ONE PROTON, TWO PROTON, AND ALPHA EMISSION FROM $^{14}\mathrm{O} + \alpha$ RESONANCE INTERACTIONS

A Dissertation

by

CHANGBO FU

Submitted to the Office of Graduate Studies of
Texas A&M University
in partial fulfillment of the requirements for the degree of

DOCTOR OF PHILOSOPHY

May 2007

Major Subject: Physics

ONE PROTON, TWO PROTON, AND ALPHA EMISSION FROM $^{14}\mathrm{O} + \alpha$ RESONANCE INTERACTIONS

A Dissertation

by

CHANGBO FU

Submitted to the Office of Graduate Studies of
Texas A&M University
in partial fulfillment of the requirements for the degree of

DOCTOR OF PHILOSOPHY

Approved by:

Chair of Committee,	Robert E. Tribble
Committee Members,	Carl A. Gagliardi
	Sherry J. Yennello
	Che-Ming Ko
Head of Department,	Edward S. Fry

May 2007

Major Subject: Physics

ABSTRACT

One Proton, Two Proton, and Alpha Emission from $^{14}O + \alpha$ Resonance Interactions. (May 2007)

Changbo Fu, B. S., Lanzhou University;

M.S., China Institute of Atomic Energy

Chair of Advisory Committee: Dr. Robert E. Tribble

In this dissertation, proton, two proton, and α emission from the $^{14}O + \alpha$ interactions were studied with the modified thick target inverse kinematics approach. The radioactive beam was obtained by using resonances in the $^{14}N(p,n)^{14}O$ reaction. The ^{14}O was $> 99\%$ pure. By using a beam analysis system, the contaminant-to-beam ratio was suppressed further to the 10^{-4} level. This makes the ^{14}O beam at TAMU one of the best available.

For the $^{14}O(\alpha, 2p)$ interaction, it was found that the resonance excited states in ^{18}Ne are populated, and most of them decay sequentially to the ground state of ^{16}O, i.e. $^{18}Ne^* \rightarrow {}^{17}F^* + p \rightarrow {}^{16}O + p + p$. Two proton events corresponding to the excited state of $^{18}Ne^*(8.45\,\mathrm{MeV})$, were found to have strong $2p$ correlation, which is the fingerprint of ^{2}He-decay. Several models were used to explain this decay process, and evidence suggests that this state decays by ^{2}He-emission.

By measuring the Time-Of-Flight for protons through the thick target, the location of $^{14}O(\alpha, p)$ reactions occurring at different places in the helium gas target were identified. With this information, we were able to measure a spectrum of protons corresponding to the population of ^{17}F particle stable states in the $^{14}O(\alpha, p)^{17}F$ reaction. This method provides a new way to measure astrophysically important reactions which involve radioactive nuclei and α particles.

By analyzing elastic scattering of ^{14}O and ^{14}C on ^{4}He, α-cluster states in $^{18}Ne^*$

and $^{18}O^*$ were found. Some α-cluster states in $^{18}Ne^*$ were found for the first time.

To **my wife, my mother, and the memory of my father**

ACKNOWLEDGMENTS

First and foremost, I would like to express my sincere thanks to Dr. Robert Tribble and Dr. Vladilen Goldberg. In the past years, I have learned a lot from their deep understanding of nuclear physics. Without their invaluable guidance, support and encouragement, this dissertation would not have been possible.

I want to express my gratitude to Dr. Sherry Yennello. Many detectors and much electronic equipment used in this project were borrowed from Dr.Yennello. Her backing is highly appreciated.

I owe thanks to my graduate committee, Dr. Gagliardi, Dr. Ko, Dr. Yennello, and Dr. Tribble for their generous advice and suggestions. Dr. Gagliardi's questions and suggestions are always to the point. I want to thank Dr. Ko for his invaluable suggestions and encouragement.

It is very lucky for me to work with my collaborators: Akram Mukhamedzhanov, Grigor Chubarian, Grigory Rogachev, Livius Trache, Yongjun Zhai, Gabriel Tabacaru, Tariq Al-Abdullah, Matthew McCleskey, Adriana Banu, Boris Skorodumov, Vladilen Goldberg, and Robert Tribble. Special thanks go to Dr. Akram Mukhamedzhanov for the time spent on the calculations, answering my (sometimes naive) questions, and for the nice and fruitful discussions. I would like to thank Dr. Trache for his help, especially his skillful operation of MARS, which boosted this project a lot. My thanks go to Dr. Rogachev for his contribution to this project, especially the R-matrix analysis code which was written by him.

My thanks go out to Dr. Roy Wada for his continuous help with the development of the photomultiplier system in this project.

I also want to express my gratitude to the staff members of the Cyclotron Institute, especially Dr. George Kim for providing the beam with qualities exceeding our

expectations.

There are quite a large number of individuals to whom I owe gratitude. My thanks go to, in alphabetical order: Dr. Xixiang Bai, Jie Bao, Xinfeng Chen, Yaosan Jia, Dr. Weiping Liu, Dr. Xiuqing Lu, Lijun Qing, Dr. Xiaodong Tang, Dr. Shuhua Zhou, and the names go on. Thank you all for your invaluable help and friendship.

TABLE OF CONTENTS

CHAPTER Page

LIST OF TABLES

LIST OF FIGURES

FIGURE Page

FIGURE Page

FIGURE Page

FIGURE Page

FIGURE Page

CHAPTER I

INTRODUCTION

A. Radioactive ion beams: chances and challenges

The exploration of nucleonic matter under extreme conditions is one of the major goals of modern nuclear physics. The structure of exotic nuclei is a very important ingredient in our understanding of the properties of nucleonic matter. It provides an insight into new features of nuclear interactions, and facilitates the development of modern theoretical approaches.

Until recently, the investigation of nuclei and their properties had been restricted to around 300 isotopes in the valley of β-stability, while there are about 7000 nuclides which are predicted to be particle bound. Thus the study of nuclear physics was limited by the number of available beams. Therefore, to reach exotic nuclei—the nuclei with unusual proton to to neutron ratio which are located far from the stability line—complicated multi-nucleon transfer reactions must be used if stable beams are used. There are experimental and theoretical challenges in the extraction of useful information about exotic nuclei from experiments with stable beams.

The development of radioactive ion beams (RIBs) was an important impetus to the field. Studies of the features and the interactions of exotic nuclei have become possible during the last two decades through unstable isotope beams. Indeed, with a RIB, one already has a neutron or proton deficient system in the entrance channel; hence it is possible to use simple reactions (resonance elastic/inelastic scattering, one/two neutron/proton transfer, resonance charge-exchange reactions etc.) to populate states in exotic isotopes.

The journal model is Physical Review C.

With the help of RIBs, recent studies have shown that exotic nuclei manifest properties and phenomena not observed in stable nuclei. It has been found that exotic nuclei often have unusually large radii, unusual density distributions and different magic numbers compared to nuclei at or near the valley of stability [1]. In addition to the interest in the structure of exotic nuclei, it is now recognized that the interactions of exotic nuclei are important in many astrophysical processes. Glimpses of the new exciting topics of nuclear physics, such as one and two neutron halos, Borromean structures, breakdown of the "old" magic numbers, inverse population of nuclear shells, new decay modes and new modes of excitation, show the power of studies of exotic nuclei by RIBs.

There are many obvious advantages of studying "simple" reactions with RIBs, such as high cross sections, known reaction mechanisms and well developed reaction theories (based on stable beam reaction studies). On the other hand, there are some disadvantages. In spite of the fact that access to exotic nuclei has become easier with the development of facilities to produce RIBs, the intensities of these RIBs are typically many orders of magnitude lower than the intensities of conventional stable beams. Besides low intensities, RIBs produced by in flight techniques have poor energy and angular resolution. Therefore there are on-going efforts to produce higher quality RIBs, and at the same time to develop new experimental approaches to overcome these shortcomings.

One of the new approaches is the thick target inverse kinematics method (TTIK) [2]. In this approach, a high-Z beam is used. The target is thick enough to stop the beam, while it allows low-Z products to pass through to particle detectors. The reaction normally is dominated by resonances and therefore has very large cross section which opens the possibility to obtain excitation functions of resonance scattering with intensities as low as 10^3 particles/second (pps).

The TTIK method has been successfully and widely applied to studies of resonance interactions of RIBs with proton targets (solid or gas like $(CH_2)_n$ and CH_4, for example Ref. [3]). However, there is only a little data on resonance interactions of RIBs with a ^{4}He target. The resonance interaction of RIBs with α particles is interesting from the point of view of the nuclear structure of exotic nuclei and has substantial astrophysical interest.

B. α-cluster structures in ^{18}Ne* and ^{18}O*

Cluster structure is an interesting phenomena which exists in nuclei. A nucleus, as a strongly interacting many-body system governed by the Pauli principle, exhibits a wide variety of characteristics and phenomena. Nevertheless, some states of the nucleus still behave like an assembly of clusters, i.e. structural subunits which are themselves made up of more than one nucleon. The reduced widths of some cluster states approach the single particle (or Wigner) limit, which is defined by

$$\Gamma_{sp} = \frac{3\hbar^2}{2\mu R^2}, \tag{1.1}$$

where μ is the reduced mass of the cluster and R is the radius of the confining potential. The Wigner limit is the limit for the largest width of a single particle/cluster resonance in the nuclear potential.

Alpha-clustering in nuclei is a long studied phenomenon. Historically, α-cluster models were the first attempts to describe atomic nuclei. It was assumed that two protons and two neutrons move together as an α-particle in the nucleus. For a simple description, the total wave function of α-cluster states can be represented as a product of a cluster wave function and the wave function of the core, like that in an atomic molecule.

From the point of view of nuclear physics, alpha-clusters present an extreme example of the clustering into bosons in the fermion's media. The extreme character of these clusters is evident from the reduced alpha cluster widths of many states in several N=Z light nuclei. These reduced alpha cluster widths are close to the Wigner limit (Eq. 1.1). Since the Wigner limit is the largest width of a single cluster in the nuclear potential, the alpha cluster appears at the edge of the nuclear potential neglecting the influence of the antisymmetrization, like a real alpha particle. The other manifestation of the surprising behavior of alpha particles in the nuclear potential is the bands of alpha cluster states in light nuclei, as illustrated in Fig 1 (from Ref. [4]). These bands, which are similar to rotational bands in nuclei, have an important new feature of alternating parity bands with similar properties. This feature can be also be related to the behavior of a single particle in the potential [5]. The systematics of the alpha cluster states are seen only in a few light N=Z nuclei, ^{12}C, ^{16}O, ^{20}Ne.

Many approaches have been introduced to provide a theoretical understanding of these α-cluster structure nuclei [6], such as the resonating group model, deformed shell models, self-consistent mean-field models, and molecular and coupled channel methods. For example, in the molecular approach, the structure is compared with an atomic molecule, leading to the idea of nuclear molecules. Several experimental results which provide evidence for the existence of nuclear molecules have recently become available. As for the shell model approach, there still remain difficulties to explain the features since too many shell model states are involved.

There are several experimental approaches to study α-cluster structure in nuclei, such as α-transfer reactions, breakup reactions, and elastic/inelastic scattering. The α-transfer approach works well for bound states but it is difficult to analyze the data in the continuum region. The advantage of the breakup method is that other more

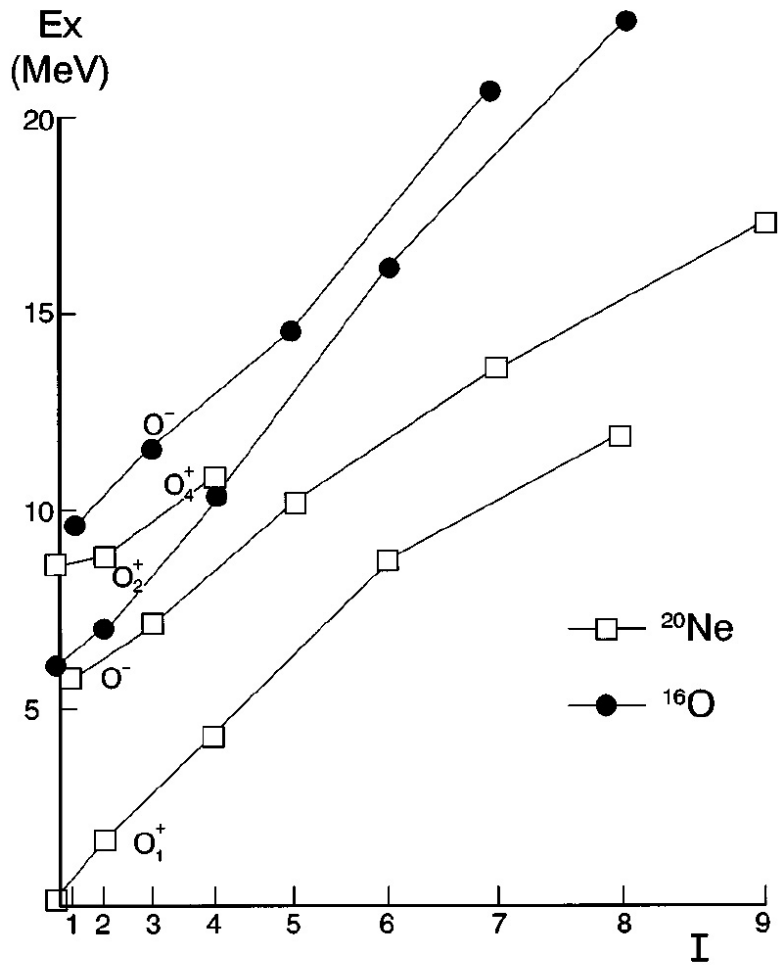

Fig. 1. The $K^\pi = 0^+$ and 0^- rotational bands in ^{16}O and ^{20}Ne. The bands shown have large α-decay widths.

exotic configurations, like ^{12}C-clusters, also can be observed. The disadvantage is that the energy resolution of this method normally is poor. In the resonance scattering approach, the energy resolution is remarkably good compared with the other two approaches. The spin-parity of states can often be assigned by R-matrix calculations. However, only states above decay threshold can be populated in this method.

Information on the specifics of alpha-cluster states in $N \neq Z$ nuclei is very scarce. In a recent publication on α cluster structure in the $^{18}\mathrm{O} + \alpha$ interaction [7], the authors found a doubling of the usual cluster structure known in $N = Z$ nuclei. Microscopic calculations [8] supported the experimental results but provide little help to understand the qualitative nature of the effect. It was claimed in several publications [7, 9, 10] that α cluster structure should be sensitive to Coulomb effects. Specifically, it was predicted in [10] that the Coulomb shift of the mirror α cluster states can shed light on the microscopic nature of these states.

The α-cluster configurations in light nuclei have significant astrophysical implications. They can be directly involved in astrophysically important reactions, increasing the probability of the capture of alpha particles, or their presence can influence the probability of reactions due to the mixture of alpha cluster structure into resonance states. α cluster structure plays a crucial role in stellar helium burning where the production of heavier elements via nuclear fusion is driven through α-cluster configurations in $T_z = 0$ and $T_z = 1$ nuclei [11]. This applies not only to stellar helium burning but also to explosive α-induced processes such as the αp-process.

The structure of the ^{18}Ne nucleus is poorly known. $\alpha + ^{14}$O resonance scattering is an appropriate way to obtain spectroscopic information on ^{18}Ne because both α and ^{14}O are spinless nucleus. In this project, ^{14}O was used to study the α-cluster structures in $^{18}\mathrm{Ne}^*$ with the resonance scattering approach.

A short review of results on the $^{14}\mathrm{C} + \alpha$ resonance interaction will be also given.

The $^{14}C+\alpha$ experiment was carried out using the tandem at Florida State University (FSU) together with a local group there. The comparison of alpha cluster structure in mirror nuclei (^{18}Ne and ^{18}O) is interesting itself. Even through ^{18}Ne and ^{18}O are mirror nuclei, one is close to the proton drip line and the other is located in the valley of β-stability. The mirror reactions, $^{14}O(\alpha,\alpha)$ and $^{14}C(\alpha,\alpha)$, provide a good way to check nuclear theories on cluster structures. In particular, the Coulomb effects which might change the mirror structure can be investigated. Furthermore, the ^{14}C beam at FSU is an intense tandem beam, while ^{14}O was available only as a secondary radioactive beam. Therefore it was possible to obtain good counting statistics in the $^{14}C+\alpha$ experiment, which are needed for reliable spin-parity assignments. Consequently, the supplemental data from the $^{14}C+\alpha$ experiment could be very useful.

C. Two proton emission from $^{18}Ne^{*}$

In 1960, V. Goldansky predicted two-proton ($2p$) radioactivity as a potential decay mode of some exotic proton rich nuclei far from the valley of β-stability[12]. He predicted a strong energy correlation between the two protons during $2p$ decay, which leads to their energies being almost equal. In Goldansky's original paper, he considered the energy which inhibits one proton decay from the ground state of a nucleus, but allows $2p$ decay to accur (Fig. 2). However, there are still other effects, such as quantum selection rules, which allow two-proton decay but block single proton decay from the ground or excited states of a nucleus. Later $2p$ decay of excited states in some proton rich nuclei was considered [13]. Two-proton emission was experimentally observed to proceed from ^{6}Be in 1977 [14].

Two-proton decay may occur through three possible mechanisms[15, 16](Fig. 3): (a) sequential (or successive) emission of protons via an intermediate state; (b) simul-

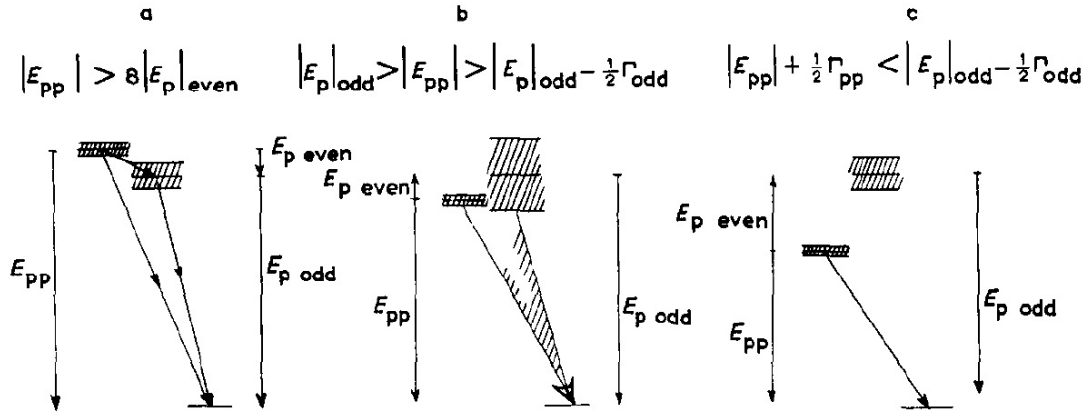

Fig. 2. Energy conditions for different modes of two proton radioactivity. (a) The decay may proceed through an intermediate state, but E_{pp} is large so the penetrability for the one proton decay through the intermediate state is small. (b) The decay may proceed through the tail of an intermediate state. (c) "Pure" two proton radioactivity as it is called in ref [12].

taneous emission of protons where there is no correlation between the two protons (or called democratic decay in some references); (c) correlated two proton emission. There is a special case (c'), where the two correlated protons come out of the nucleus as a cluster, and then separate due to the Coulomb interaction. In other words, the "correlation" here means that the two protons are "together". This special correlated decay is called ^{2}He-decay. The democratic decay was found in some nuclei, for example ^{12}O [17]. The correlated $2p$ decay, but not ^{2}He-decay, was recently found in ^{94}Ag(21^+) [18]. There are $2p$ emission cases found in ^{6}Be [14], β-decay of ^{22}Al and ^{26}P [19, 20], ^{45}Fe [21], ^{54}Zn [22], etc., without the decay mechanisms specified experimentally. However, up to the present time the pure ^{2}He decay has not been confirmed.

The ^{18}Ne nucleus, with its two proton decay threshold lying below the α particle decay threshold, appears to be a good candidate for observing $2p$ decay from its excited states. There was a recent attempt to observe a correlated $2p$ decay from

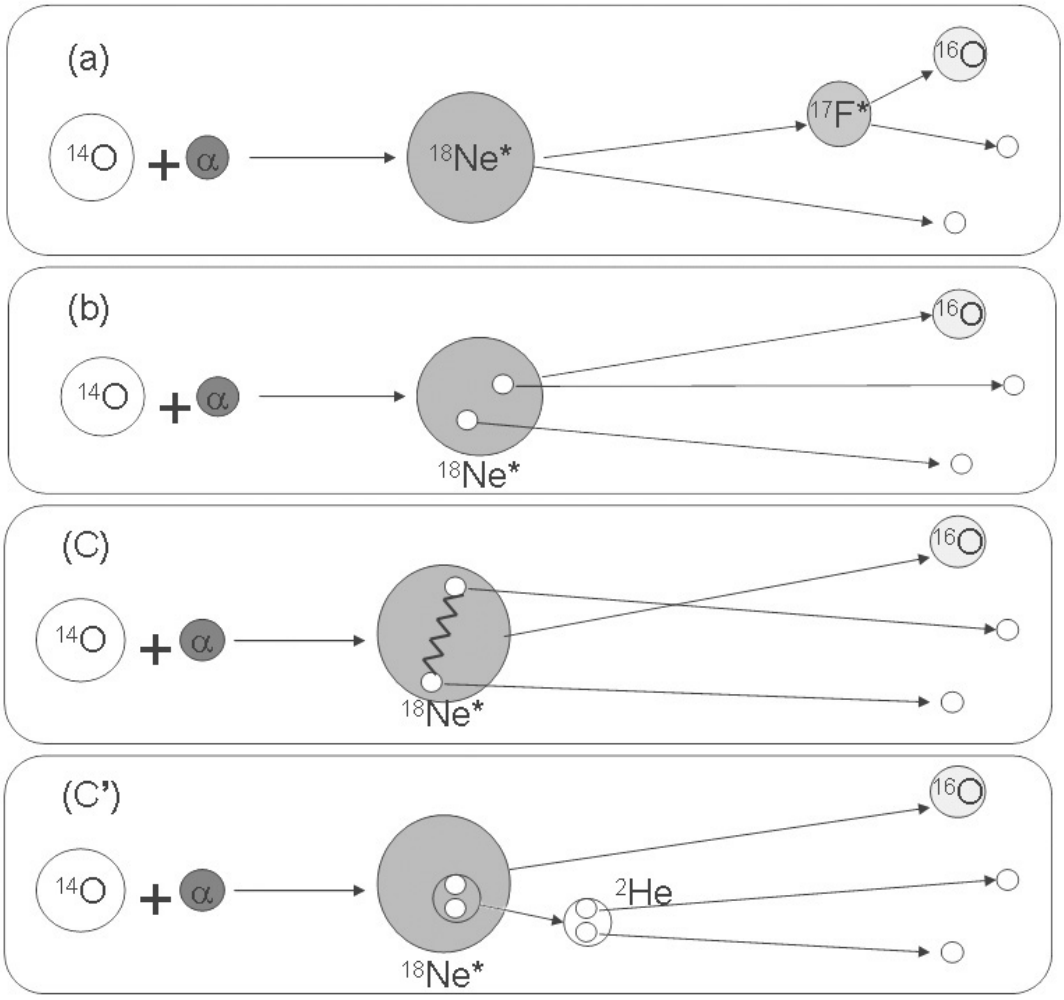

Fig. 3. Three possible mechanisms of two-proton emission: (a) sequential decay (or successive decay); (b) simultaneous decay (or democratic decay), where there is no correlation between two protons; and (c) correlated $2p$ decay, where the two protons have correlation between each other. There is a special case of the mechanism (c), the two protons exist in the nucleus as a cluster, diproton or ^{2}He, and are emitted as a cluster. This mechanism is shown in (c').

excited states in ^{18}Ne using a resonance in the $^{17}\mathrm{F} + p$ reaction [23]. However, the interpretation of the results has been criticized [24]. In Ref. [23], it is very difficult to disentangle the three-body decay of $^{18}\mathrm{Ne}^*$ states from the breakup of ^{17}F on a proton target, since both cases provide 2 protons in the final states. With a helium target, cleaner experimental results can be obtained by the $^{14}\mathrm{O} + \alpha$ resonance reaction.

Reviews of this topic can be found in Ref. [16, 25].

D. The (α, p) reaction and its astrophysical impact

Understanding the nucleosynthesis processes that take place in the cosmos is one of the primary goals in nuclear astrophysics. Simulations are used to study those stellar dynamic processes, from the time scale of milli-seconds in explosive burning scenarios to giga-years of stellar evolution. These simulations are strongly dependent on the input parameters from nuclear physics.

The astrophysical importance of nuclear reactions induced by α-particles is evident due to the helium abundance in the Universe; about 25% of the visible mass of our Universe is helium. One of these interactions is $^{14}\mathrm{O} + \alpha$. This reaction may be important during the ignition phase of x-ray bursts. In stellar explosions such as novae and x-ray bursts, ^{14}O is produced by successive proton captures on ^{12}C and ^{13}N (Fig. 4). At relatively high stellar temperatures, the reaction chain $^{14}\mathrm{O}(\alpha, p)^{17}\mathrm{F}(p, \gamma)^{18}\mathrm{Ne}(\alpha, p)^{21}\mathrm{Na}$ could provide a path to the rapid proton capture (rp) process which can lead to the build-up of iron group elements by successive proton captures. Because ^{15}F is unbound, hydrogen burning by the $^{14}\mathrm{O}(p, \gamma)^{15}\mathrm{F}$ reaction does not occur. Therefore, a significant amount of ^{14}O may be accumulated due to its relatively long β-decay life time ($t_{1/2} = 71\,s$). The rate of the $^{14}\mathrm{O}(\alpha, p)^{17}\mathrm{F}$ reaction is essential for understanding this process since it determines the conditions under

which ^{14}O beta decay is bypassed.

The rate of $^{14}\mathrm{O}(\alpha, p)^{17}\mathrm{F}$ has been studied by different indirect methods, such as by the time reversed reaction $^{17}\mathrm{F}(p, \alpha)^{14}\mathrm{O}$ [26, 27, 28], and estimating widths and spin assignments from the mirror nucleus ^{18}O [29, 30]. However, direct measurements are still important, at least to estimate the population of the first excited (particle stable) state in ^{17}F at 0.5 MeV. In a pioneering work [31], the authors claimed a "Direct measurement of the astrophysical reaction $^{14}\mathrm{O}(\alpha, p)^{17}\mathrm{F}$". In Ref. [31], the reaction was studied with the thick target inverse kinematic method (TTIK) [2]. Due to the TTIK method used, the authors had a large low energy proton background in their measurement which obscures the interpretation. This point will be discussed in detail later.

The remaining chapters of this dissertation are as follows. Chapter II and Chapter III present experimental techniques and data analysis methods which were used in the studies of all the reactions. I will focus on the difficulties which are induced by the radioactive ion beam and the thick target method used in the experiment. Following them, Chapter IV, V, and VI will discuss details of the data analysis which are more specific for each reaction (α, α), $(\alpha, 2p)$, and (α, p) separately. The results obtained will also be given in each corresponding chapter. A summary is given in the last chapter, Chapter VII.

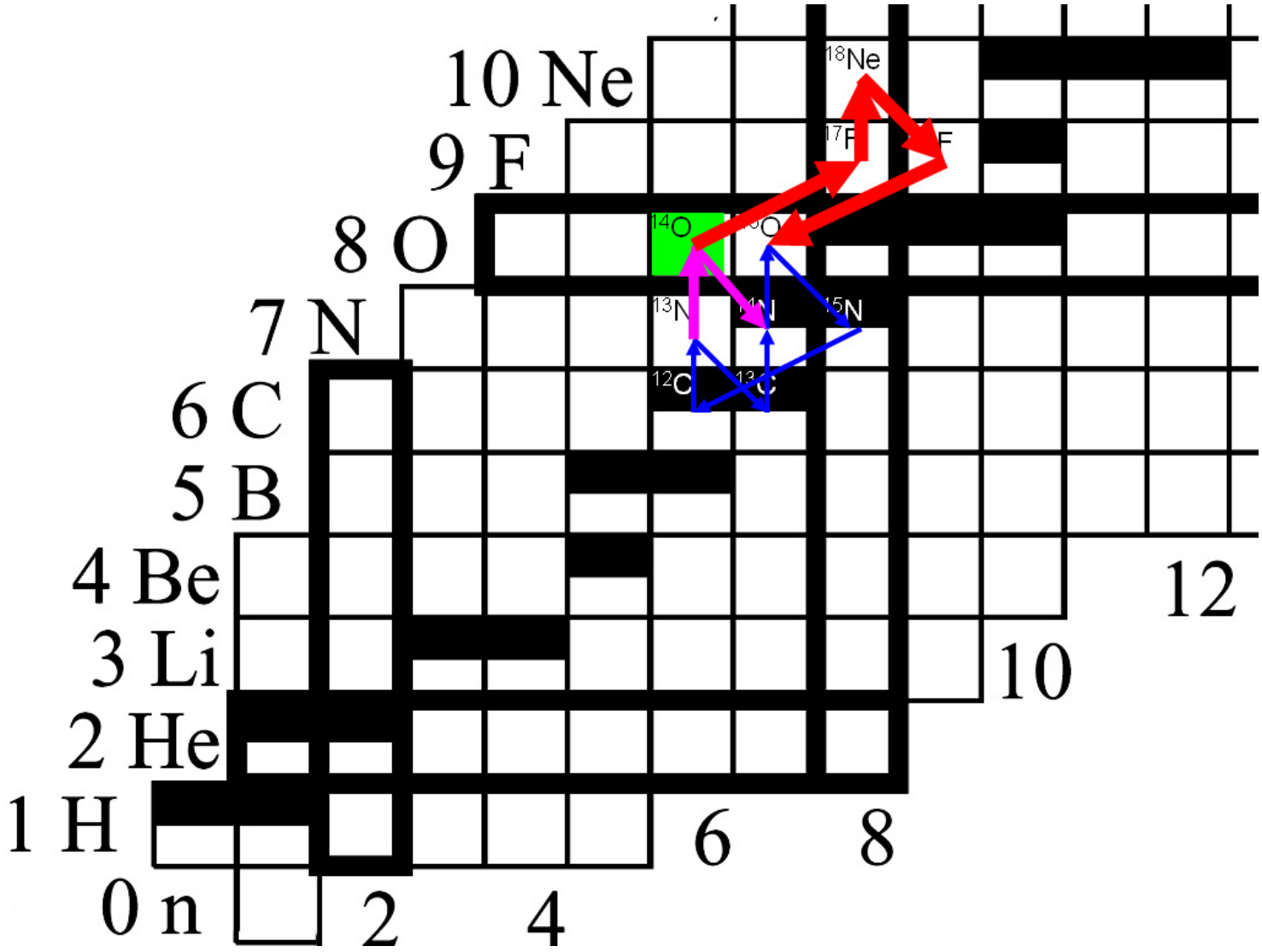

Fig. 4. The CNO and the hot CNO cycles. When the temperature is low ($T_9 \approx 0.1$), the hydrogen burning process in a star like our sun is dominated by the CNO cycle (blue lines); if $T_9 \approx 0.2$, $^{13}\mathrm{N}(p,\gamma)$ can bypass $^{13}\mathrm{N}$ β^+ decay (pink lines); if $T_9 \approx 0.4$, $^{14}\mathrm{O}(\alpha,p)$ can bypass $^{14}\mathrm{O}$ β^+ decay (red lines).

CHAPTER II

EXPERIMENTAL PROCEDURE

The experimental setup used to measure $^{14}O+\alpha$ is shown in Fig. 5. A ^{14}N beam from the TAMU K500 superconducting cyclotron was used to bombard a liquid-nitrogen-cooled hydrogen gas target to produce the ^{14}O RIB. The ^{14}O products from the H(^{14}N,$^{14}O)n$ reaction were purified by the Momentum Achromat Recoil Spectrometer (MARS) [32]. Behind MARS, the ^{14}O particles underwent reactions with helium in a gas chamber. The rate of ^{14}O incident on the helium gas was monitored by a scintillator detector before the gas chamber. The products from the $^{14}O+\alpha$ reaction were measured by a silicon detector array.

Typically, when one carries out experiments involving RIBs, the beam intensity is the bottleneck. Normally, the intensity of the RIB is several orders of magnitude weaker than stable beams. Furthermore, beam purities, energy spreads and angular spreads are much poorer than those for stable beams.

To improve the qualities of the ^{14}O RIB which is used in the experiment reported here, some special apparatus and techniques were used. The equipment included the Momentum Achromat Recoil Spectrometer (MARS) (II.A), a liquid-nitrogen-cooled first gas target (II.B), a secondary gas target(II.D), and the particle detectors, which included a silicon detector array (II.E), a thin foil detector system (II.F), and the Data Acquisition System (II.G). The specific reaction which was used to produce ^{14}O will be described in (II.C).

A. The Momentum Achromat Recoil Spectrometer (MARS)

The Momentum Achromat Recoil Spectrometer (MARS) [32]has been used for a wide variety of nuclear reaction studies utilizing inverse kinematics. MARS is able to

operate over a broad energy range with good mass resolution and high efficiency. It is also able to operate at large scattering angles. Therefore one can obtain products from fusion, fragmentation and deep inelastic scattering with the same device. MARS also has been proved to be effective for producing a wide variety of secondary radioactive beams for nuclear physics studies.

A schematic layout of MARS is shown in Fig 5. A primary beam from the K500 superconducting cyclotron passes through a beam swinger system which allows for adjusting the scattering angle. The dipole magnet SW1 bends the beam into the second magnet SW2 which is located just in front of the target chamber. Combining the two magnets, we can adjust the scattering angle from 0° to 30°.

MARS has two dispersing planes. The first dispersion is provided by the dipole magnet D1 in the horizontal direction with a maximum momentum dispersion at the entrance to the quadrupole magnet Q3. The combination of Q1, Q2, Q3, D1 and D2 provides for an achromatic beam with nearly parallel transport into the velocity filter which provides the second dispersion vertically. The beam is bent up by the dipole D3 and is focused by the final two quadrupoles, Q4 and Q5 in both the vertical and horizontal planes. This provides the M/q mass focus.

When MARS operates close to 0°, the primary beam passes through the dipole D1 and into the coffin where the original dispersion plane is located. Due to D1, the primary beam is usually separated from the secondary beam. A Faraday cup located there is used to integrate the primary beam, which can provide a method for measuring the absolute cross section of a reaction.

There are several slits along the beam line. They are used to limit the angular spread and momentum spread of the reaction products at the final focal plane, and at the same time to get rid of the contaminants which are not wanted, specifically, the contaminants which have a different M/q value from what is required. Slit-1,

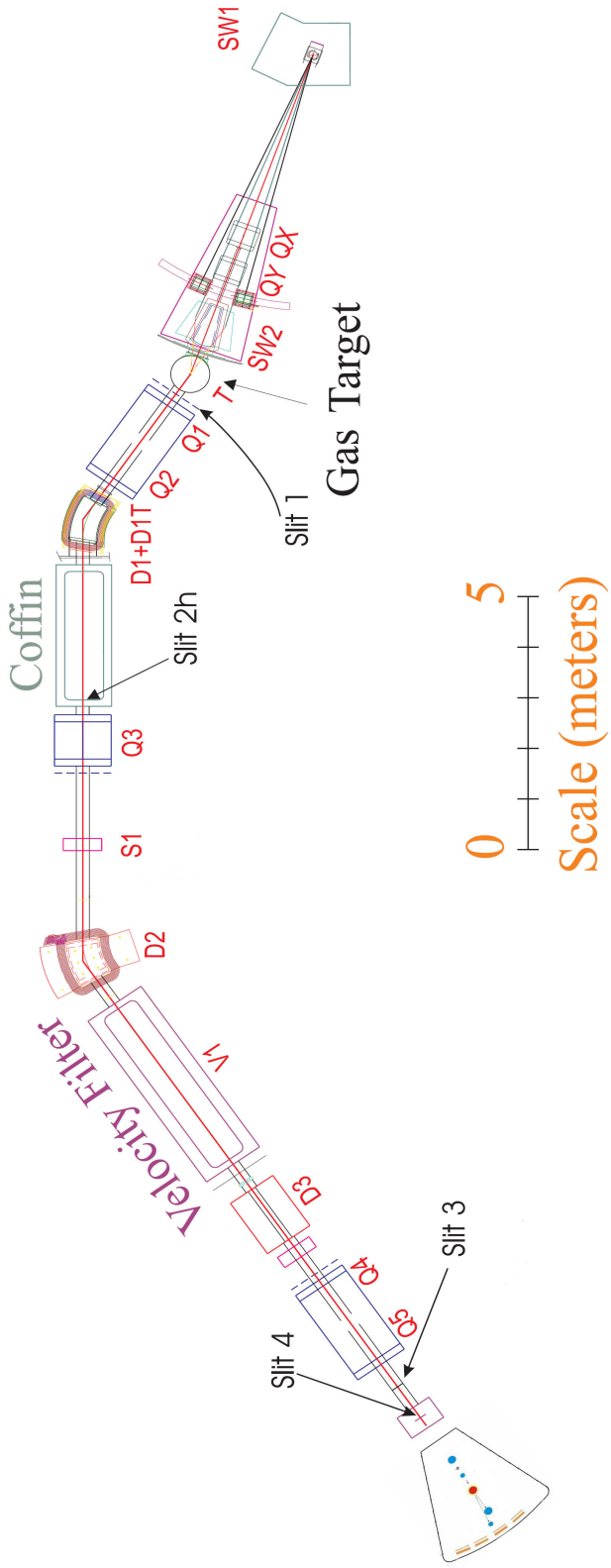

Fig. 5. Sketch of the Momentum Achromat Recoil Spectrometer (MARS) at Texas A&M University.

located just after the primary target chamber, determines the initial phase space of the particles. Between D1 and D2, at the dispersion plane of D1, there is a horizontal slit set, Slit-2h. The momentum spread is defined by its width. After Q4 and Q5, there are two slit sets, Slit-3 and Slit-4. The main function of Slit-3 is to define the angular spread of the secondary beam, and Slit-4 is used to get rid of the contaminants which have very close M/q values to the secondary beam.

MARS has a mass resolution of $\delta M/M = 1/300$, with an energy acceptance of $\Delta E/E \approx \pm 9\%$ and a geometric solid angle of up to 9 msr. The maximium $B\rho$ is about $18\, m \cdot kG$. The specifications of the system are given in Table I, and more details of the system can be found in Ref. [32].

B. The MARS gas target

To increase the effective target thickness and then the production of the RIB while keeping relatively low gas pressure, the gas target may be cooled to liquid nitrogen or even liquid helium temperature. A schematic drawing of the liquid-nitrogen-cooled gas target unit used for the work here is shown in Fig. 6.

The gas target unit has two main parts, a dewar and a gas cell. The dewar has a volume of about $2.8\, l$ for liquid-nitrogen (LN_2). The length of the gas cell, which was made of stainless steel, is about $9.0\, cm$. The gas cell intersects with the dewar and is surrounded by LN_2 which cools it down to a temperature of approximately $77\, K$. The gas cell is separated from the high vacuum of the beam line by Havar windows. The pressure of the target gas in the cell is monitored remotely in order to check for leaks in the windows that can develop during irradiation.

By cooling the gas cell, the gas density, and hence the yield of the reaction

Table I. Specifications for MARS

Overall length	19 m
Max. scattering angle[1]	30°
Max. solid angle	9 msr
Max. $B\rho$ of D1	$17.865\,m \cdot kG$
Max. $B\rho$ of D2	$17.865\,m \cdot kG$
Max. field of D3	6 kG
Max. bend angle of D3	25°
Max. electric field of the velocity filter	50 kV/cm
Max. magnetic field of the velocity filter	1 kG
Energy range with $2.0\,cm/\%$ for $\delta M/M$	$\pm 9\%$
Mass resolution [2]	1/300 (FWHM)
Path length dispersion	2 cm

[1]The angle between the axis of the primary beam and the reaction products.

[2]When $\Delta E = \pm 9\%, \Omega = 2\,msr$.

products could be increased significantly[1] by keeping the same pressure. For the experiment reported here, two Havar foil windows with thickness 12.5 μm were used. The gas target unit worked well under pressures up to 3.3 atm.

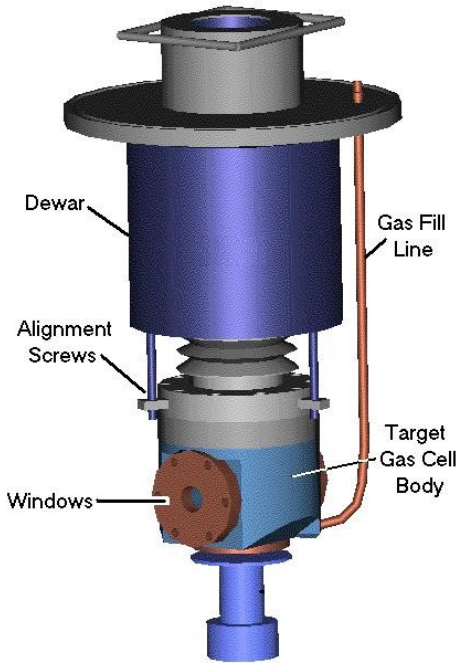

Fig. 6. The liquid-nitrogen-cooled gas target unit.

C. Production of ^{14}O from the ^{1}H(^{14}N,^{14}O) reaction

The ^{14}O beam was produced via the ^{1}H(^{14}N,^{14}O)n reaction. There are two resonance peaks in the energy range from 6 MeV to 11 MeV [33] as shown in Fig. 7. One is at 7.95 MeV/A (with $FWHM \approx 175\,\mathrm{keV}/A$), and the other is at 9.85 MeV/A (with $FWHM \approx 600\,\mathrm{keV}/A$). Both resonances were used to produce the ^{14}O RIB. To achieve this, a beam energy of ^{14}N at 12.7 MeV/A was chosen. At this energy,

[1]For a narrow resonance reaction, this may not true. The narrow resonance reaction will be discussed below.

the K500 cyclotron at TAMU could provide a high primary ^{14}N beam intensity. As is shown in Fig. 8, the beam passes through a Be degrader to reduce its energy at the entrance window of the gas target. After passing through the gas cell window, the beam energy decreases to the point ($\approx$ 11 MeV) where the resonance reactions will take place. The energy degrader of Be was chosen to minimize multiple scattering since this material has low Z.

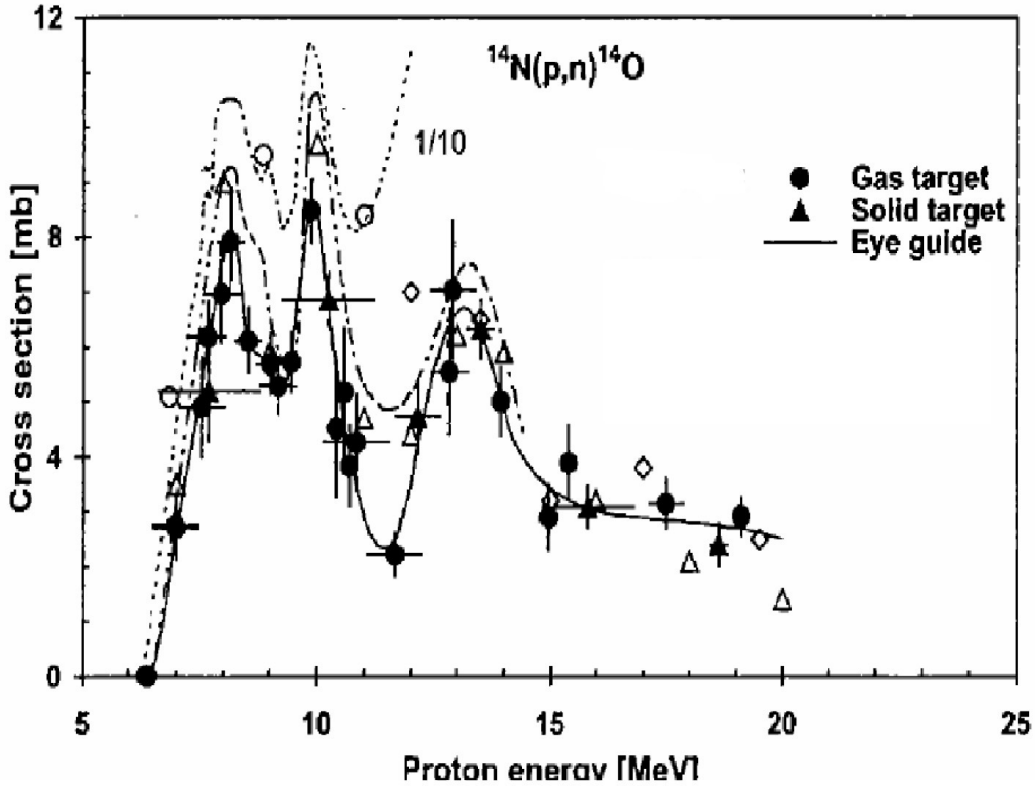

Fig. 7. The excitation function of the $H(^{14}\mathrm{N},^{14}\mathrm{O})$ reaction.

For a narrow resonance reaction, only some part of the target has a significant contribution to the yield if the energy loss of the beam in the target is larger than the width of the narrow resonances in question. The resonance yield of the reaction

^{1}H(^{14}N,^{14} O) can be estimated with the formula

$$\Delta N \simeq I\bar{\sigma}\,\Delta\Omega\Delta N_t,$$

where I is the intensity of the ^{14}N beam and $\bar{\sigma}$ is the average cross section at the resonance peak. ΔN_t is the number of target nuclei involved in the process.

Due to the lack of experimental data about the differential cross section in this energy range and the unknown spins of the resonances, we can not simulate the energy spectrum of ^{14}O without additional assumptions. With the assumption that the angular distribution is isotropic in the center of mass system, the energy spectrum of ^{14}O from a Monte Carlo simulation is shown in Fig. 9.

For a single resonance peak, the effective target thickness is

$$\Delta x \approx \frac{\Gamma}{\mathrm{d}E/\mathrm{d}x}, \tag{2.1}$$

where $\mathrm{d}E/\mathrm{d}x$ is specific energy loss of the beam particle, and Γ is the FHWM of the resonance. While the primary ^{14}N beam is slowing down in the gas cell, it passes through the resonance at 9.85 MeV/A. For this resonance, about $9.2 \times 10^{20}/cm^2$ hydrogen atoms are involved in the reaction. The energy spectrum of outgoing ^{14}O particles is shown in (A). The energy range is $100 - 130$ MeV. Similar calculations were made for the resonance peak at 7.95 MeV/A. The spectrum is shown in (B), and the energy range is 90—105 MeV. The ^{14}O products deposit part of their energy in the gas and the window of the gas cell as they exit. At the exit window, the ^{14}O spectrum is shown in (C). The two peaks, corresponding to $9.85\,\mathrm{MeV}/A$ and 7.95 MeV/A resonance peaks, overlap since the ^{14}O specific energy loss is greater than ^{14}N. Then the ^{14}O nuclei are separated from the primary beam by MARS. In practice, one can tune MARS, scanning the energy range between 60—90 MeV to get the maximum rate of ^{14}O.

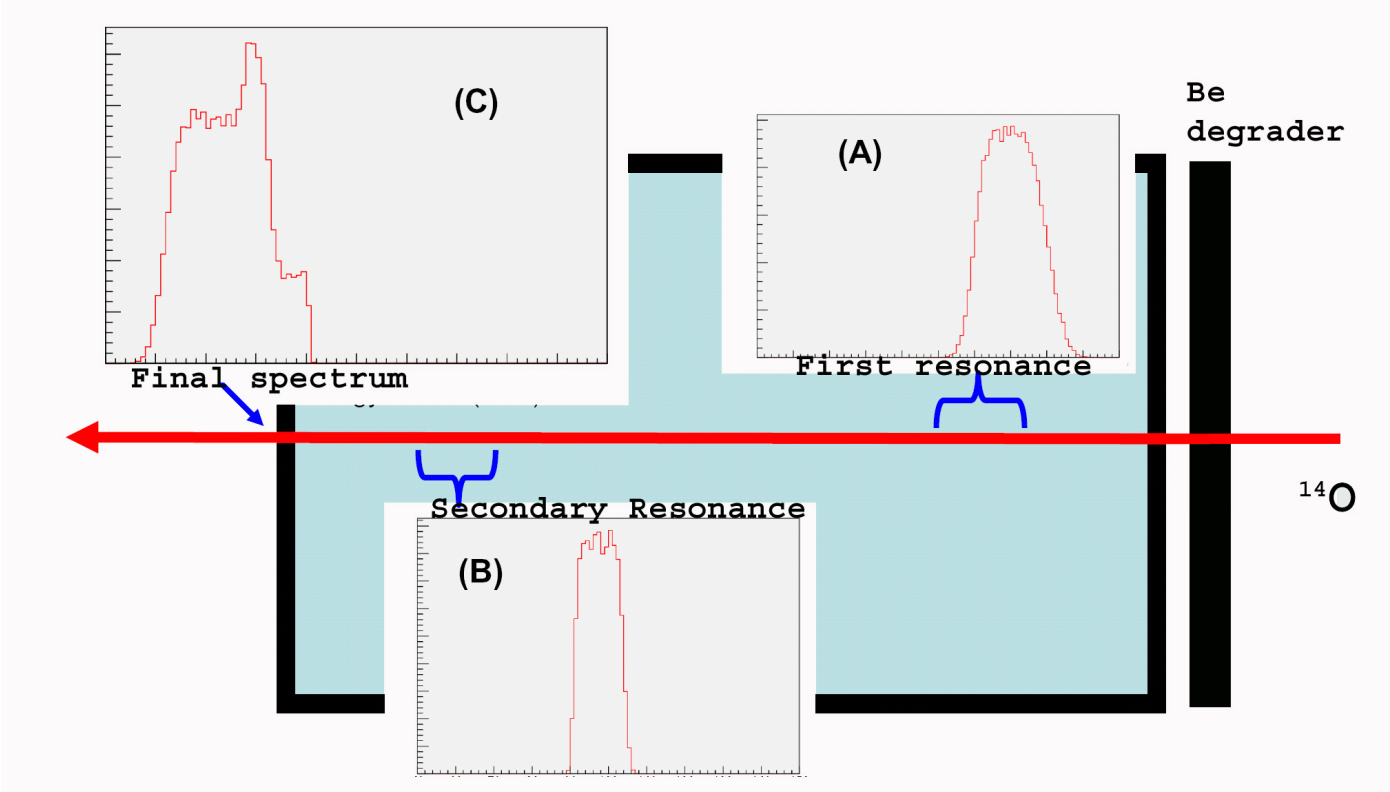

Fig. 8. To improve the yield of the ^{14}O, two resonance peaks in the excitation function of ^{14}N(p,^{14}O)n were used. The picture here shows the ^{14}O energy spectra at different positions in the gas cell.

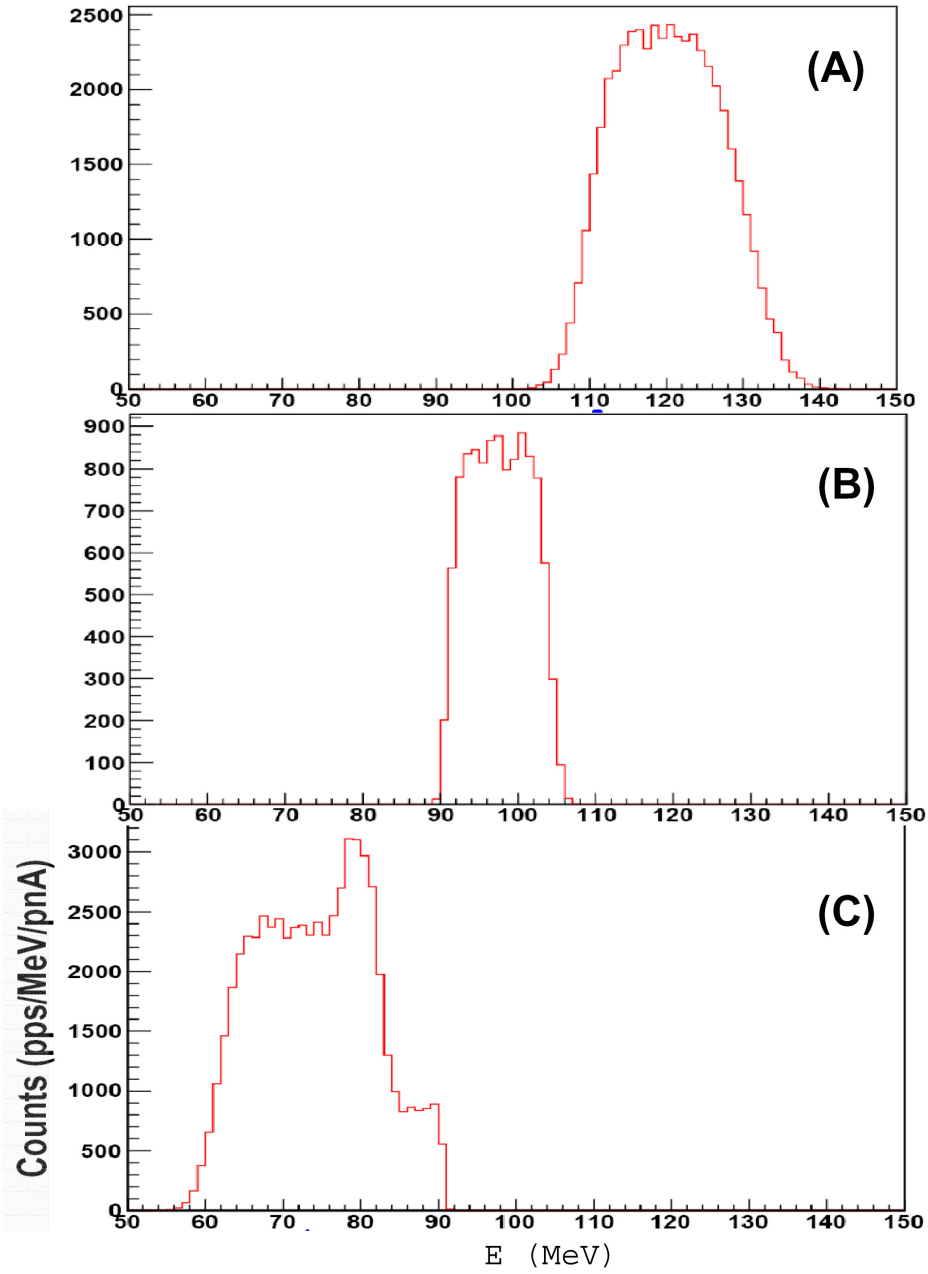

Fig. 9. The ^{14}O yield from the different parts of the primary target. (A) is the energy spectrum of ^{14}O from the resonance at 9.85 MeV; (B) is energy spectrum of ^{14}O from the resonance at 7.95 MeV; (C) is energy spectrum of ^{14}O after the target.

Only those parts of the primary target, where the beam energies are in the resonance peaks, contribute significantly to the total reaction productions. In other words, some parts of the gas target give a small contribution to the total ^{14}O yield, or they serve as a degrader. In this sense, these parts of the target can be replaced with other degraders without decreasing the ^{14}O yield much. Taking into account that the volume of the gas cell is limited and high pressure could induce some problems like gas leakage, a $3\,\mu m$ Al degrader was placed in the middle of gas cell (Fig. 10), and a hydrogen gas pressure around $2.5\,atm$ was chosen.

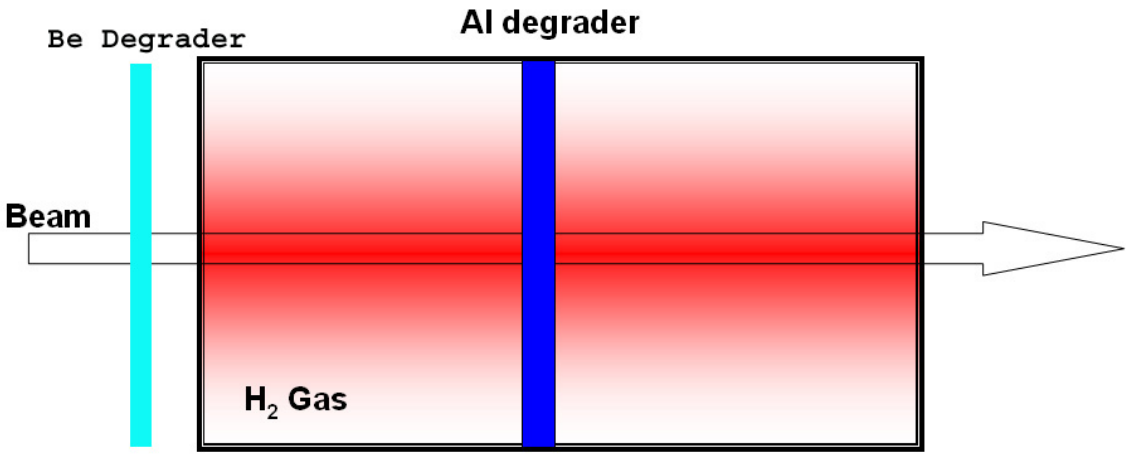

Fig. 10. A $3\,\mu m$ Al degrader was put in the middle of gas cell to decrease the working pressure without losing ^{14}O production rate. Due to beam heating, the temperature as well as the gas density in the gas cell may not be homogeneous. The temperature (density) along the beam path may be higher (lower) than in other parts. A Be degrader combined with the Havar window of the gas cell reduces the energy of the primary beam to the resonance range.

For the RIB beam study, a 5×5 cm, 300-μm-thick, position sensitive silicon strip detector (PSSSD) was mounted on the focal plane of MARS. The PSSSD consisted of 16 3-mm-wide resistive strips. The position resolution was 3 mm in the horizontal

direction and better than 1 mm in vertical direction. The back plane of this detector provided a signal corresponding to the total energy loss of the particles. The beam spot dimensions were measured to be about 5 mm horizontal by 5 mm vertical, both full-width at half maximum (FWHM).

Figure 11 shows the ^{14}O spectrum measured by the PSSSD. The dark spot at the position $(Y, Energy) = (0, 1220)$ is ^{14}O. The main contaminants were ^{7}Be (around channel 600) which has the same q/m as that of ^{14}O. One can also see some protons around channel 100. The tail of ^{14}O (around channel 1210, see also Fig. 12) was due to incomplete charge collection when particles hit the gap between two strips of the PSSSD.

The energy acceptance of MARS was set to $\approx 2\%$, i.e., about 1.5 MeV. A secondary beam intersity of 2.5×10^5/s was achieved. The purity of the ^{14}O beam was better than 99%.

It is worth pointing out that beam heating in the gas cell is especially important for resonance reactions. When the beam passes through the gas target, the temperature along the beam path may increase significantly due to the energy deposited by the beam (Fig. 10). Therefore this part of the gas expands, and then the beam deposits less energy (due to fewer atoms), until a balance is established. Due to this effect, at high beam intensity, the energy loss pattern along the beam path may very different from that with a low beam intensity. In the beam study stage, a low beam intensity is used, while a high beam intensity is used in the real measurement. Therefore the resonance reaction condition may not be satisfied after the beam study. Due to resonance properties of the reaction here, the effect is much larger than those with the direct reactions or broad resonance reactions. We observed a significant decrease ($> 30\%$) of the yield ratio of ^{14}O/^{14}N between low and high ^{14}N intensities.

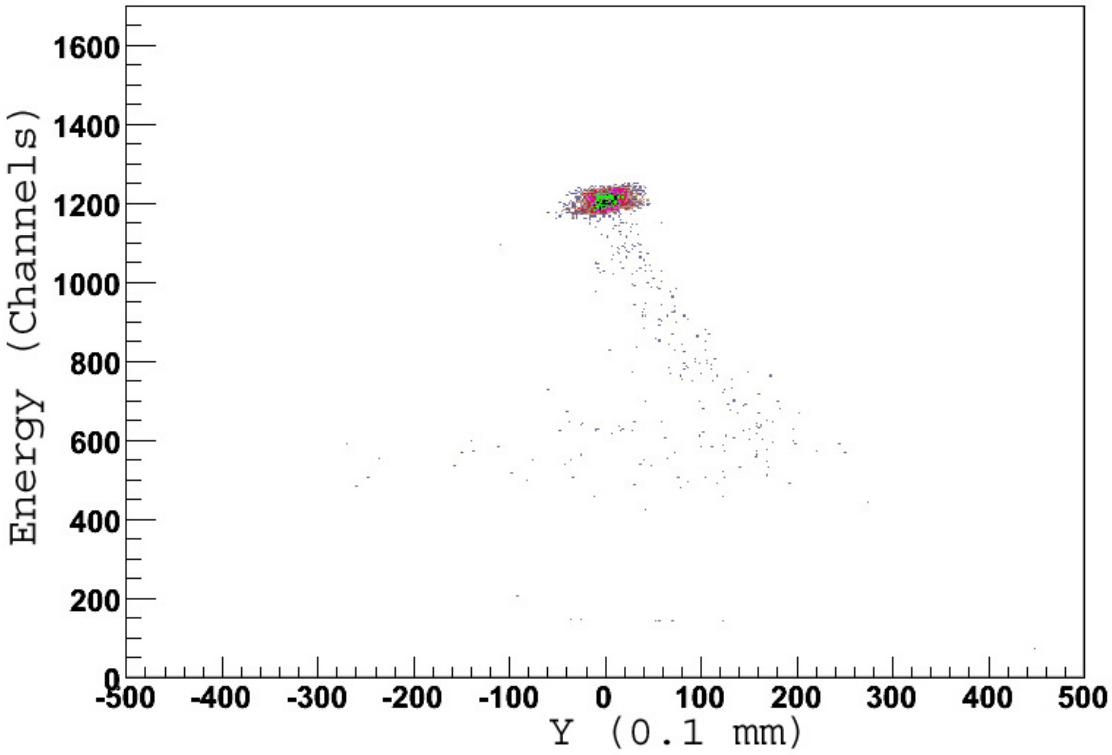

Fig. 11. The energy vs. vertical position (Y) spectrum of ^{14}O measured by the PSSSD.

D. The secondary target

For an experiment with interactions between α particles and radioactive particles, a helium gas target is almost the only choice. Even through the analysis of gas target data is more difficult than these data obtained with solid targets, gas target measurements still have advantages. Compared with a solid target, the thickness of a gas target can be changed continuously and easily by adjusting the gas pressure. The thickness of the target is also very homogeneous. These qualities were utilized in the secondary target chamber, which is shown in Fig. 13. The chamber was filled with the ultra-pure ^{4}He gas (99.99%), which was used as the target. The chamber was pumped out to high vacuum before filling with the helium gas. This prevented

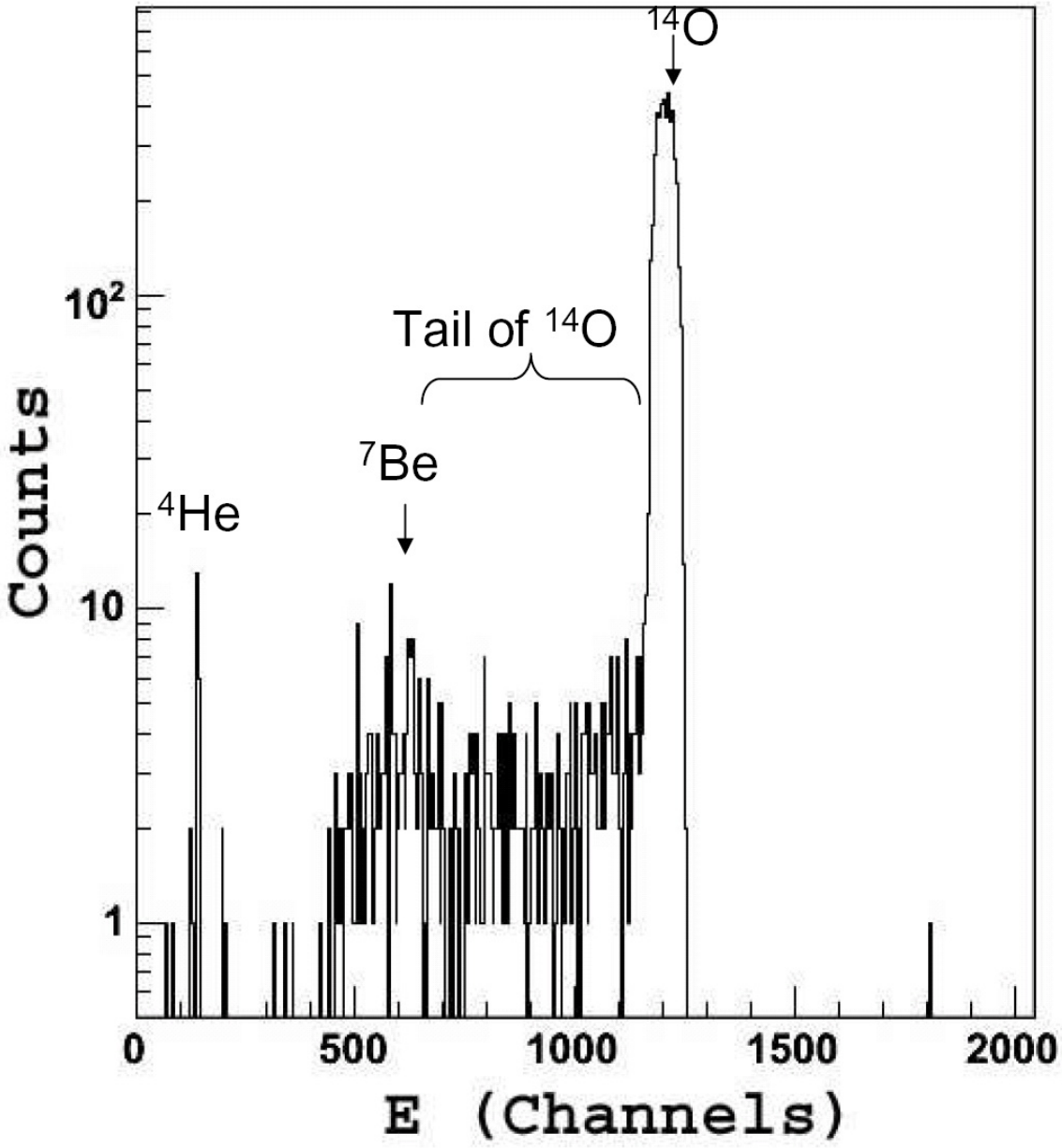

Fig. 12. The energy spectrum of ^{14}O measured by the PSSSD.

the possibility of target contamination by air. During the experiment, different gas pressures were used. The pressure of the target was sufficient to stop the secondary ^{14}O RIB, but most of the light products from reactions could still pass through the gas and were detected by the detectors placed in the gas.

E. The silicon detector array

Due to different properties of the reactions, the detection system as optimized in separate setups for detecting different products, including p, $2p$, and α.

1. The $^{14}\mathrm{O}(\alpha,\alpha)$ reaction

For the $\alpha(^{14}\mathrm{O},\alpha)$ reaction, the main issues were the statistics and the energy/angular resolution of the α spectra which would be used for the R-matrix analysis later. The setup of the detection system was complicated by the contradicting requirements. The optimized setup was shown in Fig. 13. Four quadrant silicon detectors (QSD) were mounted 47 cm away from the entrance window of the scattering chamber. Each QSD was composed of 4 silicon pads with dimensions of $2.5\,cm \times 2.5\,cm \times 0.1\,cm$. The gaps between pads were under 0.3 mm. Each pad was separated electronically from the others and could provide an independent energy signal. No cross-talk was found between pads when tested with an α-source and with the beam during the experiment.

2. The (α,p) and $(\alpha,2p)$ reactions

In addition to elastic scattering, we measured both one- and two-proton events from the $^{14}\mathrm{O}+\alpha$ interactions. For $2p$ events, the yield of a coincidence measurement is proportional to the product of two solid angles and hence it is very low. Therefore the

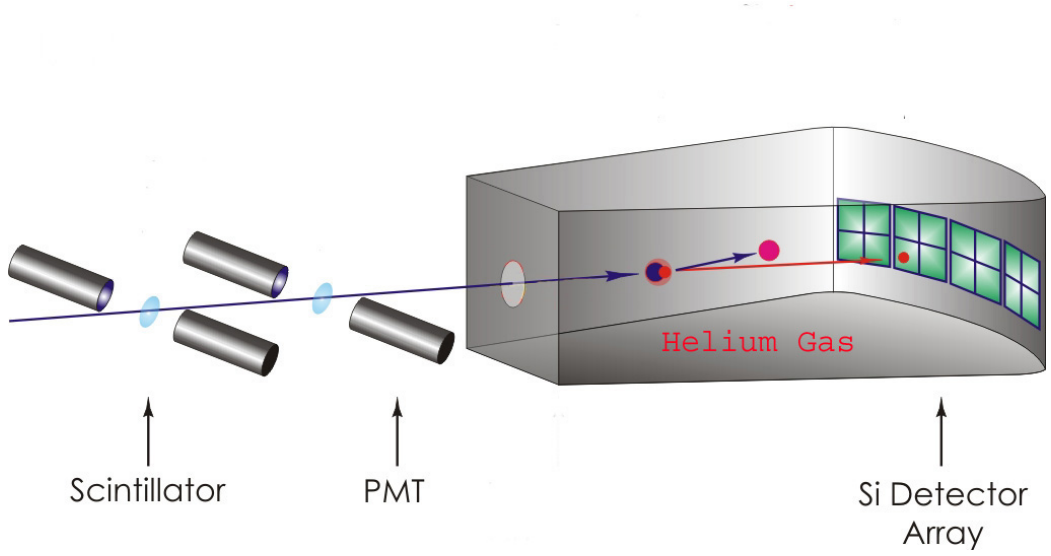

Fig. 13. Experimental setup optimized for elastic resonance reaction $^{14}\mathrm{O}(\alpha,\alpha)$.

main difficulty for $2p$ emission was to obtain enough events for analysis. Naturally, an increase in solid angle helps. The solid angle can be increased by moving the detectors closer to the reaction location, resulting in a higher gas pressure in the chamber to stop the beam. On the other hand, the energy resolution becomes worse when the distance between the event and the detectors decreases. Suppose a detector has constant position resolution of $1\,mm \times 1\,cm$. When it is moved closer, say from 100 mm to 50 mm, the angular resolution decreases from 1/100 to 1/50. Different angles mean different energies. Therefore, with the angular resolution decreasing, the energy resolution decreases.

To find an acceptable setup for the experiment, a simulation was carried out in which only kinematics was considered. The resulting setup for detecting coincident $2p$ events is shown in Fig. 14. The same QSDs were used, but they were moved close to the entrance window to provide the larger detection solid angle. Using results from the simulation, a distance of $19\,cm$ was chosen to mount the detector array. The coordinates of the detectors were $(x, y, z) = (\pm 42.5, \pm 37.5, 190)\,mm$. Since the

high energy protons could punch through $1\,mm$ of silicon, two silicon detectors were mounted behind the QSDs. The last detector severed as a veto for those events where the particles passed through the front detectors.

To provide better time resolution signals, which is important for the (α, p) measurement (the reason for doing this will be explained in detail below), two telescopes with small detectors were mounted $40\,cm$ away from the entrance window. The telescope was composed of ΔE and E_r silicon detectors which had a diameter of $1.2\,cm$, and thickness of $1\,mm$.

By choosing the proper pressure for the helium gas, the ^{14}O particles were stopped before the silicon detectors. Fast signals from silicon detectors were used as the stop signals for the TOF. The particle's energy signal combined with its TOF provided particle identification. A time resolution of $1.2\,ns$ was achieved with $2.5\,cm \times 2.5\,cm \times 1\,mm$ quadrant silicon detectors in an offline test measurement.

F. The thin film detectors

The thin film detectors (TFDs) composed of BC-400 scintillator foils and photomultiplier tubes (PMTs) were used in the experiment. TFD has many advantages, such as fast time response, small energy loss of transmitted particles, little sensitivity to radiation damage, high efficiency, flexible size, and low cost. With plastic scintillator foils, it is easy to make a detector which is thin enough even for weakly penetrating particles like heavy ions. Normally, the thin film scintillator detectors serve as transmission detectors which respond to the fraction of energy lost by the particles as they pass through the detectors. Because organic scintillators have a scintillation decay time of only a few nano-seconds, they have proved to be very useful in fast timing measurements. A typical plastic scintillator shows little decrease in light output with

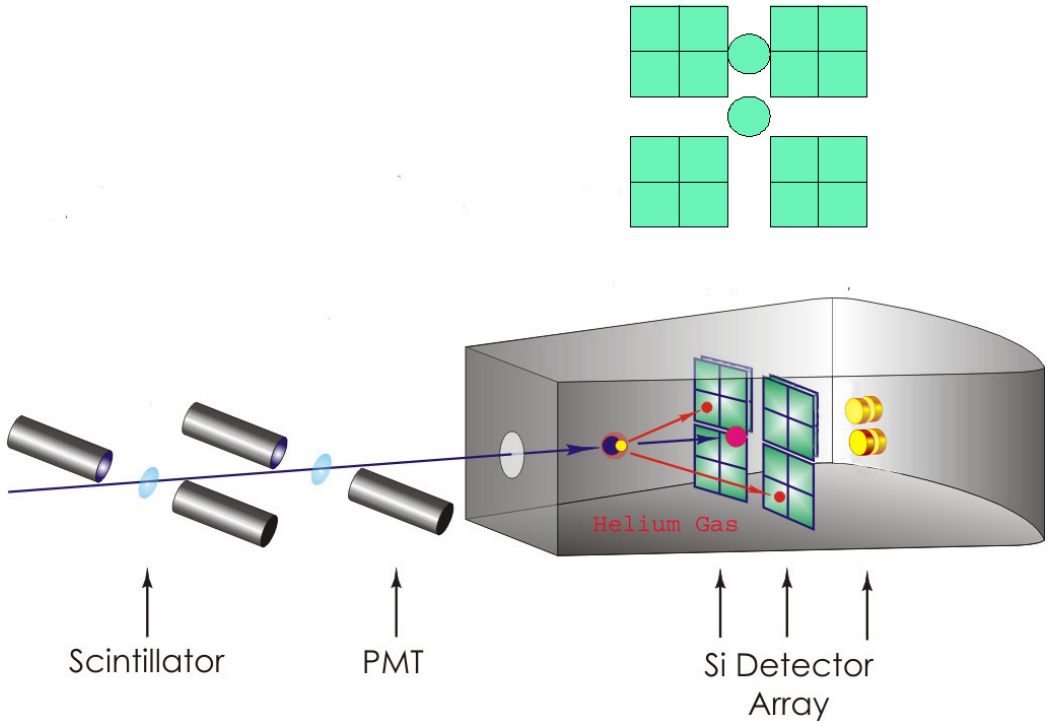

Fig. 14. Experimental setup optimized for the $^{14}\mathrm{O}(\alpha, p)$, and $^{14}\mathrm{O}(\alpha, 2p)$ reactions.

dose as high as $10^5\,Gy$ ($1\,Gy = 1\,J/kg$). A foil with a thickness as low as $10\,\mu\,m$ is available commercially. Various groups have found that the TFD is very useful for registering the transition of heavy charged particles, identification of particles, and time-of-flight experiments [34, 35, 36, 37].

Figure 15 shows the drawing of the TFD used in this experiment. A thin BC-400 scintillator foil was mounted at an angle of 45° along the beam. The light induced by particles passing through the foil was detected by a pair of photomultiplier tubes (PMTs). The internal surface of the cube which housed the PMTs was painted white to increase the light collecting efficiency. The position of the PMTs relative to the scintillator foil was optimized for light collection efficiency and energy resolution of the TFD system. An energy resolution of about 27% (Fig. 16) and time resolution of about $1.0\,ns$ was achieved using an $^{228}\mathrm{Th}\,\alpha$-source with a counting rate as high as

$10^6\ pps$.

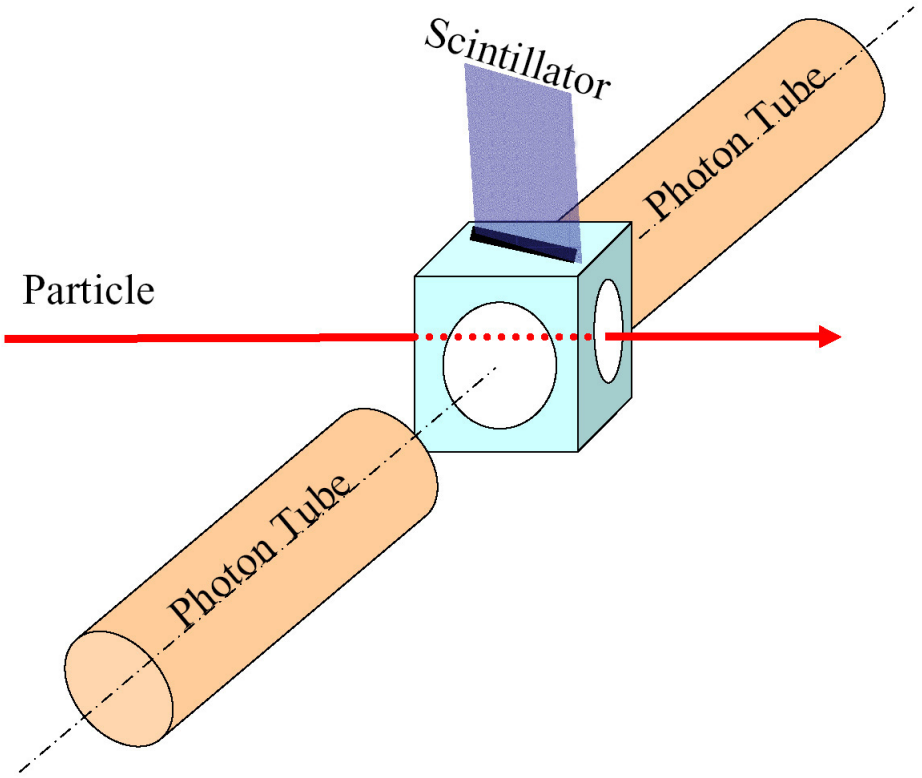

Fig. 15. Setup of the Thin Foil Detector (TFD). The BC-400 scintillator is inserted into the cube 45° along the beam. Two PMTs, which are perpendicular to the beam and 45° to the foil, are used to collect light induced by the passing particles.

The BC-400 scintillator light yield increases with the energy deposited in the foil, and it also depends on the atomic number of the ion [36] (Fig. 17). Therefore the signals from the PMTs were integrated to give an output proportional to the light yield, and then was used for particle identification. In this experiment, $^{7}Be^{4+}$ particles, which had the same q/m as $^{14}O^{8+}$, could not be removed by MARS. Other contaminants might be the result of the multiple scattering of prolific particles like protons, and α's. The TFD helped to remove these contaminants from the data.

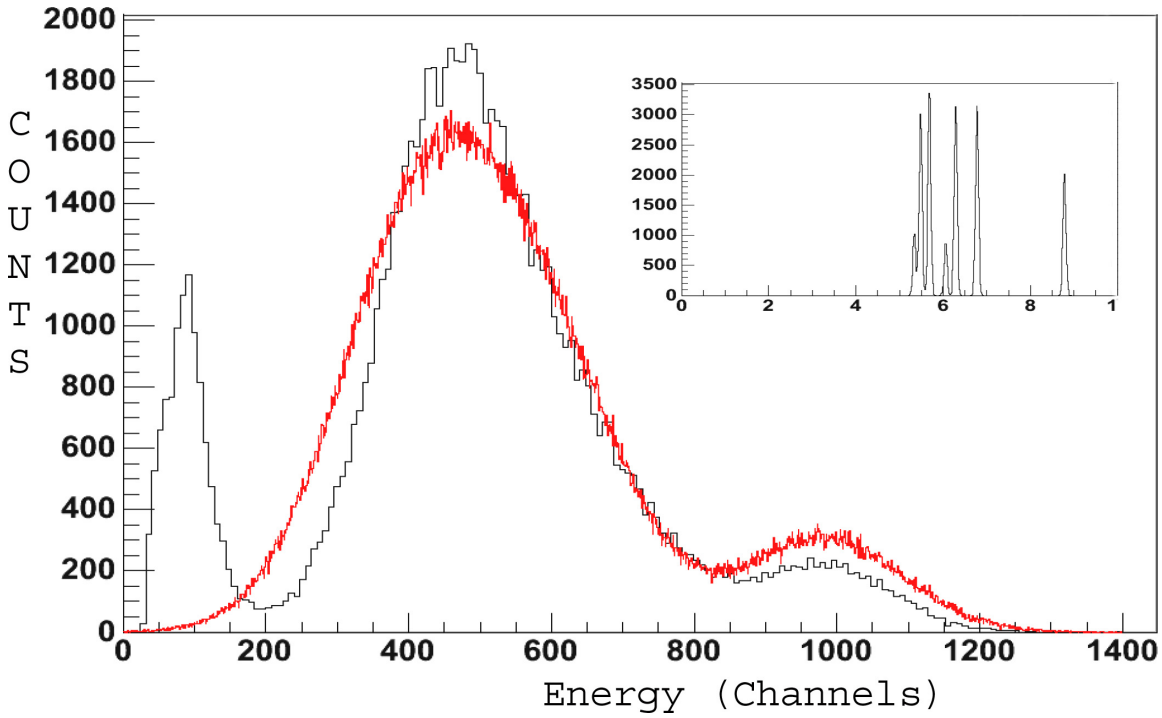

Fig. 16. The energy spectrum of a ^{228}Th α-emitting source measured by the TFD. The BC-400 scintillator is thick enough to stop 8.8 MeV alpha particles. The insert shows the spectrum measured by a silicon detector. The red line is a Monte Carlo simulation with an assumption that the energy resolution of the TFD is 1.5 MeV (FWHM).

Two TFDs, each composed of a 15 μm BC-400 foil with a 15 mm diameter collimator and a pair of PMTs, were used in the experiment as shown in Fig. 13. The counting rate between the two TFDs enabled us to monitor the particle transfer efficiency, which averaged about 95% during most of the experiment.

The signal from the PMTs was split into three channels to produce one analog and two logic signals. The logic signals were used to measure the beam intensity and, after gated by signals from silicon detectors, to provide the "start" for the time of flight (TOF). The analog signal was integrated by a charge-to-digital converter (QDC).

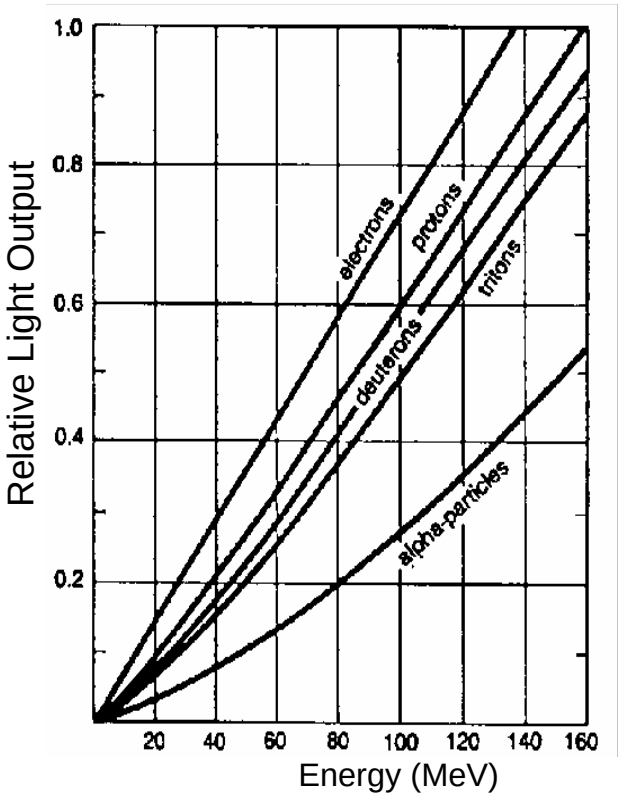

Fig. 17. The response of BC-400 scintillator to Atomic Particles. (From the product brochure of BC-400 scintillator)

G. Signal processing and data acquisition system

The signal processing circuits are illustrated in Fig. 18. The energy signals from the silicon detectors were sent to pre-amplifiers and then to CAEN Multichannel Amplifiers. The outputs from the amplifiers were passed to Analog-to-Digital Converters (ADCs). The CAEN Amplifier has an internal Timing Filter Amplifier. The fast signal from the CAEN amplifier was sent to a Constant Fraction Discriminators (CFD). The output of CFD was used for: (i) counting the events with scalers; (ii) triggering

the Data Acquisition System (DAQ); (iii) stopping the Time-to-Digital Converters (TDCs).

Signals from the PMTs were routed to fast amplifiers. The outputs of the amplifiers had a typical width of 20 ns (FWHM). The signal was split into two parts with one signal being sent to a Charge-to-Digital Converter (QDC) and another part being passed to CFDs if not vetoed by silicon detectors. The outputs from the CFDs were used as start signals of TDCs. In this way, the DAQ did not record every particle which passed through the scintillator. The secondary beam had a counting rate of about $2 \times 10^5\, Hz$ on the foil. The rate was too high for the DAQ to record. After gating by signals from the silicon detectors, the rate was about $3 \times 10^2\, Hz$ which was acceptable for the DAQ system.

The data acquisition system included a CAMAC crate, a VME frontend, and a backend host computer as shown in Fig. 19. The computer talked with the CAMAC crate via the VME frontend and got event data from it. The data was saved to disk for offline analysis.

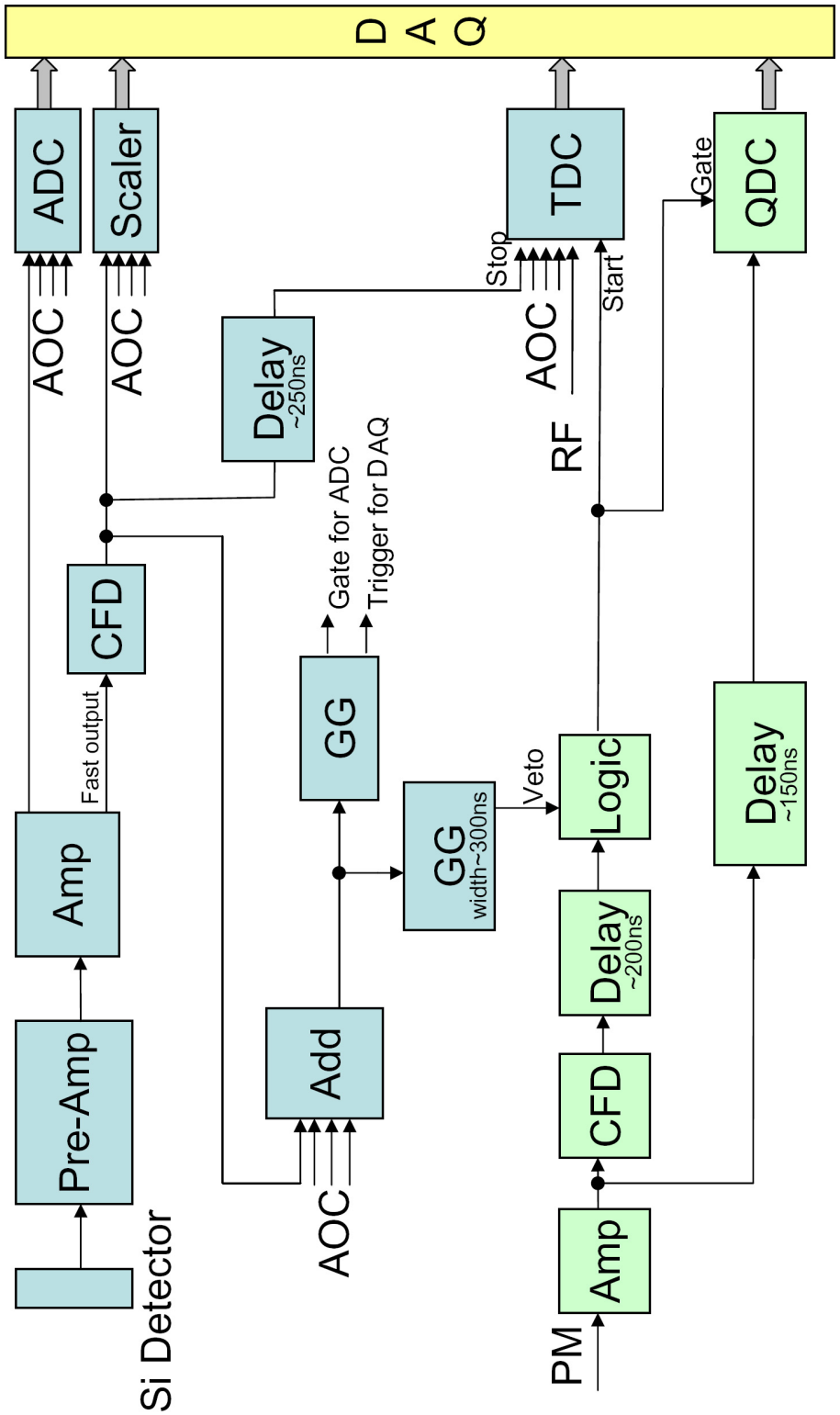

AOC: All Other Channels, i.e. the signals that are the same but from different detectors.
RF: Radio frequency signals from cyclotron
GG: Gate Generator
CFD: Constant Fraction Discriminator
DAQ: Data acquisition system

Fig. 18. Sketch of the signal processing.

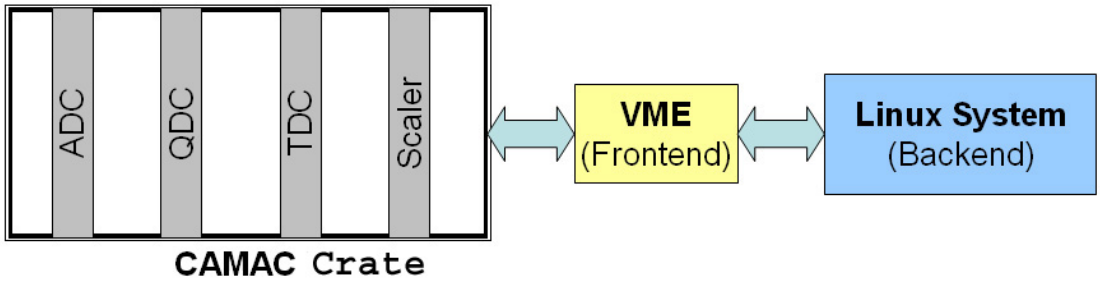

Fig. 19. Sketch of the data acquisition system used in the experiment at TAMU.

CHAPTER III

DATA ANALYSIS

The online data collected by the acquisition system was saved to disk in an event-by-event format for offline analysis. After a careful calibration of the energy signals from the detectors (III.A), the particles were identified by several different methods, including ΔE,E, and TOF(III.B).

The data were analyzed mainly by using the program ROOT [38]. ROOT is a $C++$ object oriented data analysis framework for scientific programming. It has been becoming more and more popular in all major high energy and nuclear physics laboratories around the world since its first public release in 1995. ROOT can monitor, store, and analyze large amounts of data in a highly efficient way. There were other software programs, including the Physics Analysis Workstation (PAW) [39], the SRIM [40], the R-matrix analysis program (written by Dr. G. Rogachev), and some codes written by myself which were used in the work reported here.

A. Energy calibration

All silicon detectors were calibrated using an α-emitting ^{228}Th source. Since the energy of the ^{228}Th peaks are well known, the energy scales of detectors were calibrated using six peaks from the ^{228}Th source. All silicon detectors had an energy resolution better than 80 keV.

The initial energy of the ^{14}O RIB could be estimated using the calibration of MARS and taking into account the ^{14}O RIB energy loss in the scintillator foils and the Havar window before it entered the helium target. Due to the thick foils (scintillators and the entrance Havar window), the energy spread of the ^{14}O beam was larger than the momentum acceptance of MARS. The initial energy of ^{14}O incident on the helium

gas was measured more precisely by the calibrated silicon detectors by pumping out the scattering chamber to high vacuum. The energy of the ^{14}O beam was measured by detectors close to 0°. A typical energy spectrum of the detectors is shown in Fig. 20. Since the ^{228}Th α-source was in the scattering chamber, the peaks from the source were measured at the same time. The energy of the ^{14}O secondary beam was found to be 32.7 MeV with a FWHM of 1.7 MeV (Fig. 20).

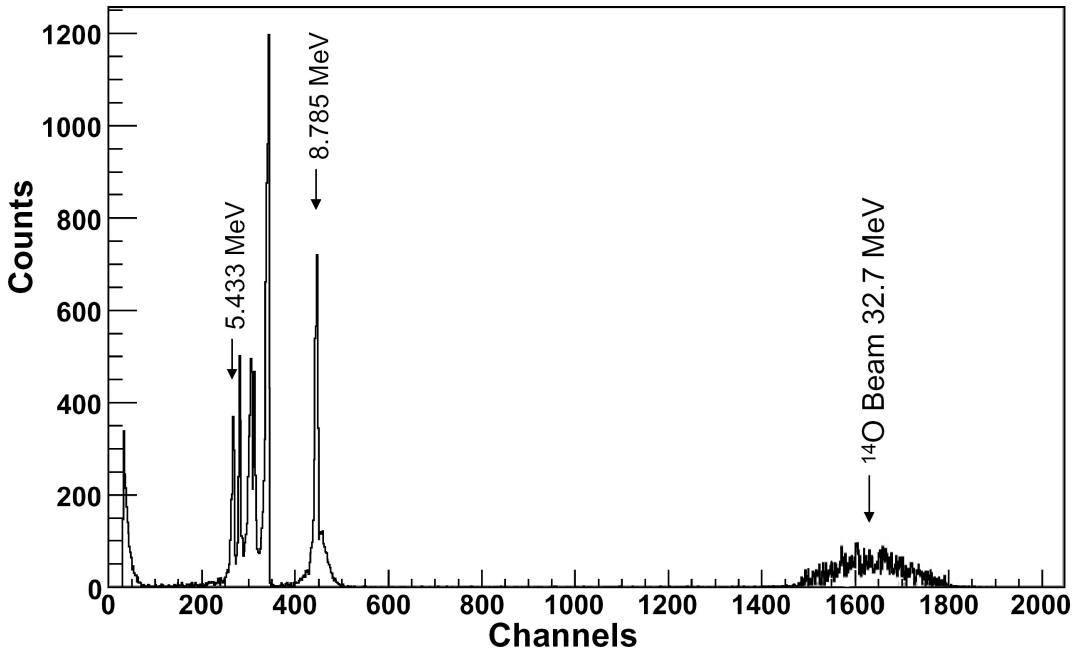

Fig. 20. An energy spectrum of the ^{228}Th α-source and the ^{14}O beam. The ^{14}O beam and ^{228}Th α-source were measured at the same time without helium-4 gas in the scattering chamber.

B. Particle identification

In the approach used in this experiment, zero degrees is important since the Coulomb scattering at zero degrees in laboratory system (corresponding to 180° in c.m. system) is a minimum while the resonance product yields are maximum. In the c.m. system,

the Rutherford scattering is

$$\frac{\mathrm{d}\sigma}{\mathrm{d}\Omega} \propto \frac{1}{\sin^4 \frac{\theta_{cm}}{2}}, \tag{3.1}$$

and the cross section has its minimum at $\theta_{cm} = 180°$. While for spin-less particles, the resonance cross section is given by

$$\frac{\mathrm{d}\sigma}{\mathrm{d}\Omega} \propto \left|P_l(\cos\theta_{cm})\right|^2, \tag{3.2}$$

where $P_l(x)$ are Legendre polynomials which have a maximum at $x = 1$, i.e. $P_l(1) = 1$.

In spite of the fact that the beam was totally stopped by the target and the beam purity was very high ($\approx 99\%$), some light particles could still pass through the target and hit the detectors. In Table II, the magnitudes of counting rates for different particles are listed. From the table, we see that the rate due to contaminants was huge in comparson with the rate from reaction products. Therefore, it was very important to identify these particles and to purify the spectra from background, especially for the detectors close to zero degrees. Several particle identification methods were used, such as ΔE-E, TOF, and TOF-E.

1. Particle identification by the TFD

During data acquisition, the computer system was triggered by signals from the silicon detectors, as illustrated in Fig. 21 as well as in Fig. 18. Only reaction products from $^{14}\mathrm{O} + \alpha$ and the low Z contaminants were recorded by silicon detectors. These events then triggered the data acquisition system to record the signals including those from the TFDs.

The response of the TFD is determined mainly by the energy and the atomic number Z of the particle [34, 35, 36, 37]. This allows the TFD signals to be used for particle identification. The signal amplitudes from the PMTs in the experiment are

Table II. Magnitudes of counting rates of the particles in the experiments

Beam	
First beam counting rate	$10^{12}/s$
Second beam ^{14}O counting rate	$10^{5}/s$
Contamination	
Proton counting rate	$10/s$
α counting rate	$10/s$
^{7}Be counting rate	$10^{2}/s$
Reaction Products	
Proton from reactions counting rate	$< 1/s$
α from reactions counting rate	$< 1/s$

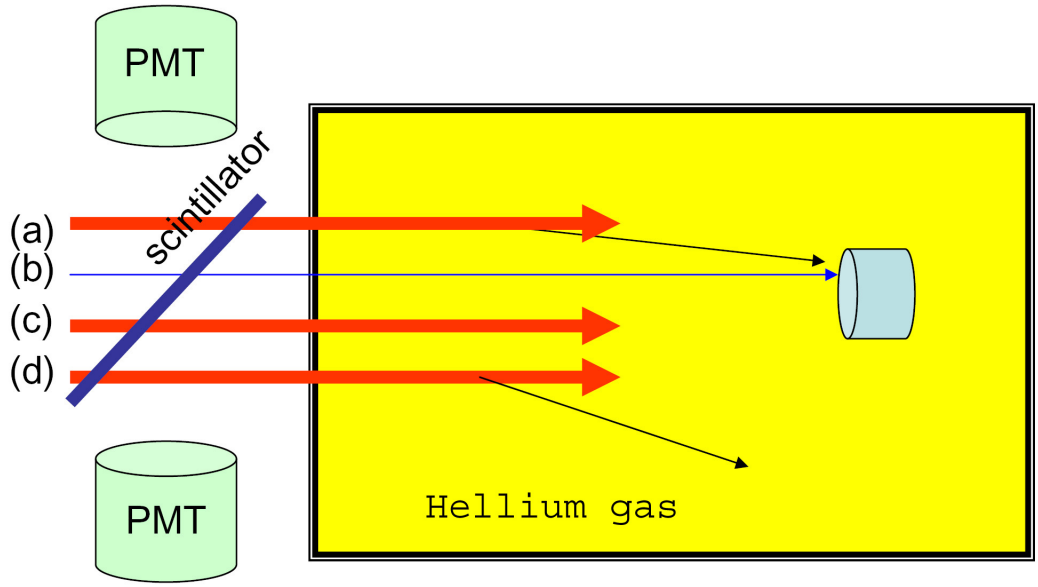

Fig. 21. Signals from silicon detectors are used to trigger the DAQ system. In two cases the PMT signals were recorded by the ACQ when (a) a product from the $^{14}\mathrm{O} + \alpha$ interaction hits a detector, or (b) a low Z contamination particle hits a detector. PMT signals were not recorded by the ACQ when (c) $^{14}\mathrm{O}$ is stopped by the target, and (d) a particle is created from a reaction but does not hit a detector.

shown in Fig. 22. The amplitude induced by ^{14}O (Fig. 22 (b)) could be distinguished from that produced by ^{7}Be (Fig. 22 (a)). Other contaminants like α's and protons, which have lower Z, had low amplitudes (below channel 200), and their counting rates were also much lower. Therefore they do not show up clearly in the TFD spectra.

Due to the time structure of the beam from the cyclotron, a special effect arises. The primary ^{14}N beam from the accelerator is not continuous but it has a periodic structure with typical beam burst duration of less than $2\,ns$ and a period of about $80\,ns$. Therefore reaction products come in bursts also and the width of the burst was measured to be about 5 ns due to the energy spread in the primary target and the time-of-flight dispersion through MARS. Therefore the reaction products from $^{14}\mathrm{N} + \mathrm{H}$ were also created with this period burst pattern. The products ^{14}O and ^{7}Be might come together in the same burst. The detector system could not distinguish events in this small time interval, and then the signals overlapped with each other. The amplitude (V) and width (σ) of two-particle events have the following relationships:

$$V_{^{14}\mathrm{O}^{7}\mathrm{Be}} = V_{^{14}\mathrm{O}} + V_{^{7}\mathrm{Be}}, \tag{3.3}$$

$$\sigma_{^{14}\mathrm{O}\,^{7}\mathrm{Be}} = \sqrt{\sigma^2_{^{14}\mathrm{O}} + \sigma^2_{^{7}\mathrm{Be}}}, \tag{3.4}$$

where $V_{^{14}\mathrm{O}^{7}\mathrm{Be}}/V_{^{14}\mathrm{O}}/V_{^{7}\mathrm{Be}}$ is peak value of the di-particle/^{14}O/^{7}Be, and $\sigma_{^{14}\mathrm{O}^{7}\mathrm{Be}}/\sigma_{^{14}\mathrm{O}}/\sigma_{^{7}\mathrm{Be}}$ is the width of the di-particle/^{14}O/^{7}Be. The experimental results corresponding to these events are shown in Fig. 22(C).

As is shown in Table III, the "small "contamination in the RIB produced a significant counting rate compared to the rate of nuclear reaction products. The overlapping PMT signal induced by an ^{14}O and contaminant particles, especially ^{7}Be, was quite important. The probability of obtaining an ^{14}O and ^{7}Be particle in a

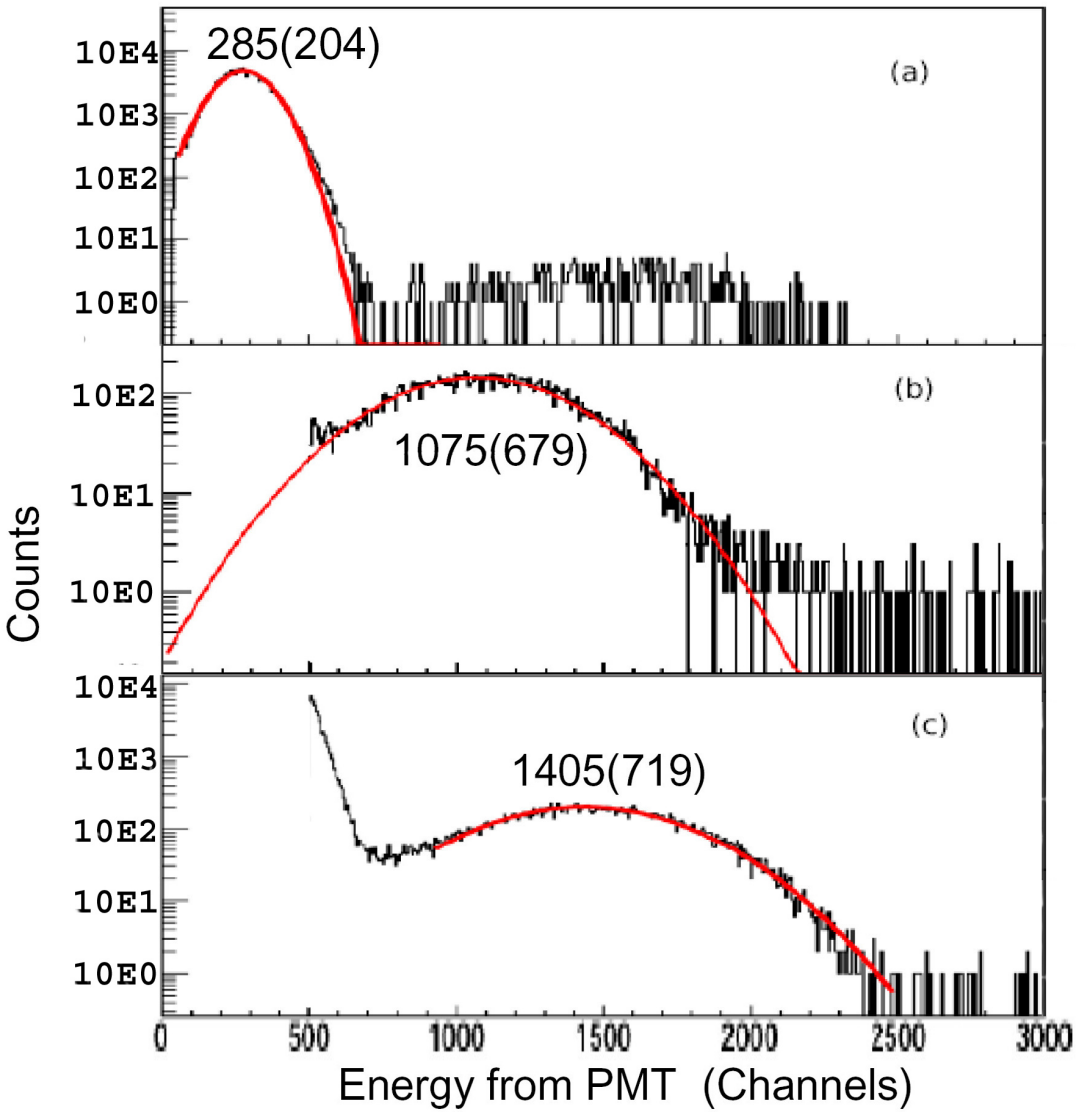

Fig. 22. The PMTs response to the ^{14}O beam and the contaminants: (a) the contribution is mainly from ^{7}Be, (b) the contribution is mainly from ^{14}O, and (c) the summed signals of ^{14}O and ^{7}Be coming from the same cyclotron burst. The number in parenthesis is the FWHM of the corresponding peak.

single burst is:

$$P_{^{14}\mathrm{O}^{7}\mathrm{Be}} = P_{^{14}\mathrm{O}} \times P_{^{7}\mathrm{Be}},$$

where $P_{^{14}\mathrm{O}}/P_{^{7}\mathrm{Be}}$is probability of obtaining a ^{14}O/^{7}Be particle in one burst of the cyclotron.

With the TFDs, we identified the ^{14}O, ^{7}Be, α, and proton events which came from MARS. However, due to the limited energy resolution, we could not separate ^{14}O from two-particle events like ^{14}O +^{7} Be, ^{14}O + α, ^{14}O + p, etc. These events required additional particle identification as will be discussed below. Table III lists some typical magnitudes of the parameters in this experiments.

A typical rise and decay time of the pulser from the TFD system was about 20 ns. The fast signal processing electronics used in this experiment were faster than 20 ns. These allowed the TFD system to count at about 2×10^7 Hz which was much larger than the beam intensity ($< 3 \times 10^5$ Hz) used.

2. TOF-E

With the start signals from the PMTs gated by the silicon detectors and the stop signal from the silicon detectors, typical TOF vs. Energy (measured by the silicon detector) spectra are given in Fig. 23. Panel (A) is a spectrum measured by the PMTs and a silicon detector at zero degrees. There is a strong peak at channel 830 which is due to ^{7}Be contamination. The continuous strip, extending from channel 100 to 1600, and overlapping with the ^{7}Be peak is due to α's from the ^{14}O+α interaction. The zone below this is due to the protons from the ^{14}O+α interaction. Another peak at $(E, TOF) = (400, 700)$ which overlaps with α strip, is due to the contamination from α particles in the RIB.

Table III. Random coincident events

Beam	
Period of the K500 Cyclotron	$\approx 80\,ns$
Width of the cyclotron burst	$< 2\,ns$
Width of the reaction products due to the cyclotron burst	$\approx 5\,ns$
Magnitude of accumulation of ^{14}O	$\approx 2 \times 10^{10}\,ion$
Random coincidence of ^{7}Be and ^{14}O	
Probability of presence of a ^{14}O in a single burst	8×10^{-3}
Probability of presence of a ^{7}Be in a single burst	8×10^{-5}
Probability of presence of a ^{7}Be and a ^{14}O in a single burst	6.4×10^{-7}
Rate of presence of a ^{7}Be and a ^{14}O together	$8\,events/s$
Random coincidence of two protons	
Probability of presence	
of a proton from MARS in a single burst	$< 10^{-6}$
Probability of presence	
of a proton from $^{14}\mathrm{O} + \alpha$ reaction in a single burst	$< 10^{-7}$
Possibility of random coincidence	
of two protons	$< 10^{-12}$
Random coincidence of two protons	
when accumulation of ^{14}O is 10^{10}	$< 10^{-12}$

Panel (B) is a typical spectrum for detectors away from zero degrees. The ^{7}Be peak, at a position $(E, TOF) = (750, 900)$, is much weaker than at zero degrees. The proton and α peaks appear at the same places as in panel (A). The proton strip bends at about channel 400 due to the protons passing through the 1 mm silicon detector.

With TOF-E spectrum, one could also determine the reaction Q-value. This will be described below.

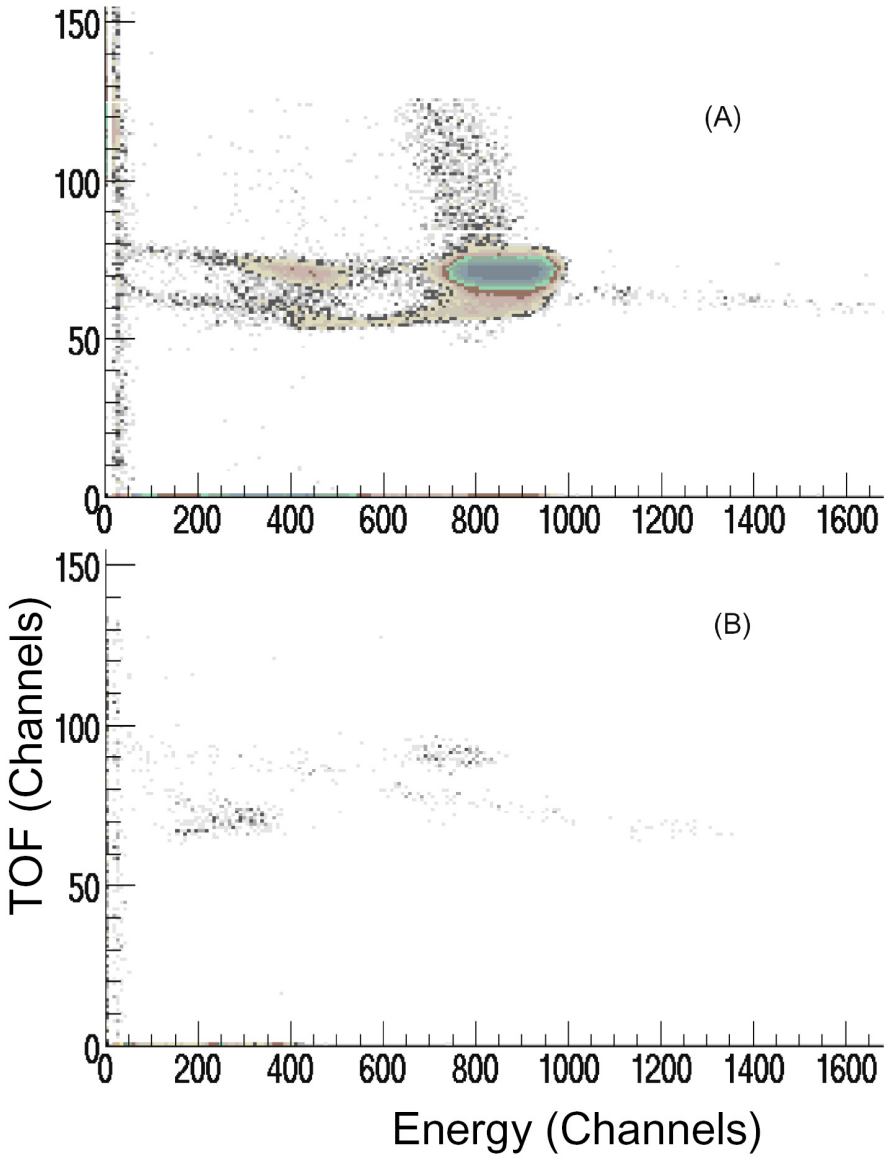

Fig. 23. Typical *TOF vs. E* spectra of the reaction products: (A) a spectrum from the detector at zero degrees; (B) a typical spectrum from a detector at 15°.

CHAPTER IV

ELASTIC SCATTERING OF ^{14}O AND ^{14}C ON ^{4}HE

A. Two body reaction kinematics for (α, α) and (α, p)

Traditionally, elastic scattering experiments have been performed by bombarding a thin target with a beam of very small energy spread. To obtain an excitation function, the beam energy is changed in small steps. It is very difficult, if it is not impossible, to use this method in a radioactive beam measurement. Normally, the intensity of a radioactive beam is many orders of magnitude lower than a stable beam. Therefore, a very long time is needed to obtain an excitation function.

The thick target inverse kinematics (TTIK) method originally was proposed to study resonance interactions of heavy ions with α particles [2]. In the TTIK, a very thick target is used to stop the incident beam which loses energy continuously due to ionization. Usually, the thickness of the target is adjusted to stop the beam completely. Due to the large difference in energy loss, a light recoil ion created in the reaction can easily penetrate through the target. These recoil ions are detected by an array of detectors which are placed in the forward hemisphere, including zero degrees. In this way the complete excitation function for different processes, such as elastic scattering, single, and di-proton emission, are measured at them same time.

Unlike the traditional thin target method, the energy of the beam is not constant in the Thick Target Inverse Kinematic (TTIK) approach. Originally [2] the TTIK method was used to study elastic resonance scattering (ERS) with the idea that the ERS dominates over all possible reactions. Since then many experiments were carried out by this method while less probable processes, like inelastic resonance scattering, were sometimes taken into account [see, for example [41]]. There were

other applications of TTIK for different nuclear reactions with outgoing particles (including proton [42], neutron [43], and γ [44]), but always with the assumption that the dominant process to be investigated was present. This might not be true in the case described in ref. [31] where the $^{14}\mathrm{O}(\alpha, p)^{17}\mathrm{F}$ reaction does not prevail over other reactions. However, with some assumptions which are discussed below, one can reconstruct the reaction kinematics. In fact, if the position of the reaction in the target can be determined, it is easy to see that a thick target is more or less like overlapping many thin targets. The kinematics of the reaction can be reconstructed, just as is done with a thin target, and the excitation function of different processes, like elastic, and inelastic scattering, can be measured simultaneously without confusion. Since the key point of this method is to find the position of a reaction by measuring the TOF of a particle, we would like to name this method "Searching for the Position Of a Reaction in a Thick Target with Inverse Kinematics" (SPORTTIK) method, or "Thick Target Inverse Kinematics with Time-Of-Flight" (TTIK-TOF) method.

1. The position in SPORTTIK

Consider a reaction $a + A \rightarrow b + B$ as it illustrated in Fig. 24. Without losing generality and making the discussion simple, a detector is put to "touch" the surface of the target as is shown in the figure. Suppose two recoil particles have the same energy when they are detected, but one comes from position x, where the energy of the beam is higher, and the other is from position x''', where the energy of the beam is lower. The two particles may have the same energy since the Q-value of the two processes may be different. Let us introduce a new parameter, the total time-of-flight ($TOF^{(t)}$), whose first part is the TOF of the beam particle, and the second part is

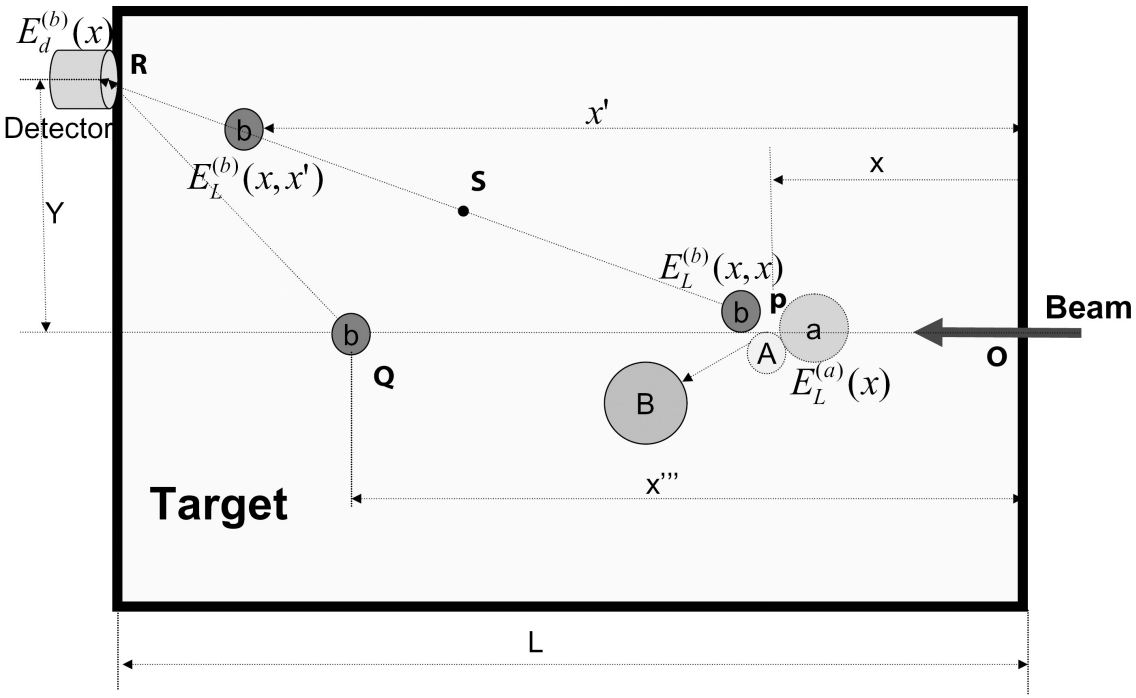

Fig. 24. An illustration of setup which was used to detect products from a two-body reaction $a + A \rightarrow b + B$ with SPORTTIK approach.

the TOF of the recoil particle. For the first particle, the $TOF^{(t)}(1)$ is

$$TOF^{(t)}(1) = TOF^{(a)}(L_{OP}) + TOF^{(b)}(L_{PR}), \tag{4.1}$$

where $TOF^{(a)}(L_{OP})$ is the beam particle flight time from point O to point P as shown in Fig. 24, and the same for $TOF^{(b)}(L_{PR})$. For the second particle, the $TOF^{(t)}(2)$ is

$$TOF^{(t)}(2) = TOF^{(a)}(L_{OQ}) + TOF^{(b)}(L_{RQ}). \tag{4.2}$$

If $L_{RQ} = L_{RS}$ for the two particles with the same detected energy, we have

$$TOF^{(t)}(2) - TOF^{(t)}(1) = TOF^{(a)}(L_{PQ}) - TOF^{(b)}(L_{PS}). \tag{4.3}$$

From this equation, we find that the speed difference of particle a and particle b opens the possibility to distinguish the recoil particles which have the same energy but come from different positions in the thick target. The Q-value of the reaction can be determined by combining the E and $TOF^{(t)}$, i.e., the kinematics of the reaction could be reconstructed. The energy of the detected particles is,

$$E^{(a)}_{Lab}(x) = E^{(a)}_{Lab}(0) - \int_0^L \frac{\mathrm{d}E^{(a)}_{Lab}(x)}{\mathrm{d}x}\mathrm{d}x, \tag{4.4}$$

$$E^{(a)}_{cm}(x) = \frac{m_A}{m_a + m_A} E^{(a)}_{Lab}(x). \tag{4.5}$$

The energy of the detected particles and the TOF^t, as a function of x and Q-value, are

$$\begin{aligned} E^{(b)}_d(x,Q) &\equiv E^{(b)}_{Lab}(L,x,Q) \\ &= E^{(b)}_{Lab}(x,x,Q) \\ &\quad - \int_0^{\sqrt{(L-x)^2+Y^2}} \frac{\mathrm{d}E^{(b)}_{Lab}(x,x',Q)}{\mathrm{d}x'}\mathrm{d}x', \end{aligned} \tag{4.6}$$

and

$$\begin{aligned} TOF^{(t)}(x,Q) &= \int_0^x \frac{\mathrm{d}x'}{\sqrt{2m_a E^{(a)}_{Lab}(x')}} \\ &\quad + \int_0^{\sqrt{(L-x)^2+Y^2}} \frac{\mathrm{d}x'}{\sqrt{2m_b E^{(b)}_{Lab}(x,x',Q)}}, \end{aligned} \tag{4.7}$$

where $E^{(b)}_{Lab}(x,x,Q)$ can be obtained by solving the kinematic equations for the reaction $a + A \rightarrow b + B$.

From equations (4.6), and (4.7), we see that the energy and TOF are functions of the distance x and Q. Since $E^{(b)}_d$ and $TOF^{(t)}$ can be measured experimentally, x, and Q then may be obtained, at least in principle, by solving the equation set (4.6) and (4.7) if the mapping $(E^{(b)}_d, TOF^{(t)}) \rightarrow (x,Q)$ is one-to-one.

The curves in Fig. (25) are calculated $TOF^{(t)}$ vs. E for the $\alpha(^{14}\mathrm{O}, p)^{17}\mathrm{F}^{*}$ reaction. The lines representing the different Q-values of the reaction separate from each other. The mapping is almost one-to-one everywhere, which means that it is possible to reconstruct the reaction kinematics by measuring the TOF-E spectrum.

2. The reaction cross section with the SPORTTIK approach

To get an excitation function for a reaction using the SPORTTIK technique requires careful consideration. In the lab system, the number of reaction products with energy in the range $(E_L, E_L + dE_L)$ going into the solid angle $d\Omega$ can be written as

$$\mathrm{d}N_L = IN_t\,\sigma_L\,\mathrm{d}\Omega_L\,\mathrm{d}E_L, \tag{4.8}$$

where I is the number of projectile particles, N_t is the number of target nuclei, and σ_L is the double differential cross section. Similarly, in the center of mass system,

$$\mathrm{d}N_C = IN_t\,\sigma_C\,\mathrm{d}\Omega_C\,\mathrm{d}E_C. \tag{4.9}$$

Since $\mathrm{d}N_C = \mathrm{d}N_L$,

$$\sigma_L \mathrm{d}\Omega_L \mathrm{d}E_L = \sigma_C \mathrm{d}\Omega_C \mathrm{d}E_C. \tag{4.10}$$

Including angular effects and using Eq. (4.8) gives

$$\sigma_C = \frac{\sqrt{1-\gamma^2\sin^2\theta_L}}{\left(\gamma\cos\theta_L + \sqrt{1-\gamma^2\sin^2\theta_L}\right)^2}\frac{\mathrm{d}E_L}{\mathrm{d}E_C}\,\frac{\mathrm{d}N}{IN_t\mathrm{d}\Omega_L\mathrm{d}E_L}, \tag{4.11}$$

where $\gamma = v_c/v_b^{'}$, v_c is the speed of center of mass, and $v_b^{'}$ the speed of the outgoing particle in the c.m. system. If the target is thin, one can get the experimental cross section in the c.m. system from this equation. For a thick target, the number of target nuclei, N_t, equates to

$$N_t = \rho \mathrm{d}x, \tag{4.12}$$

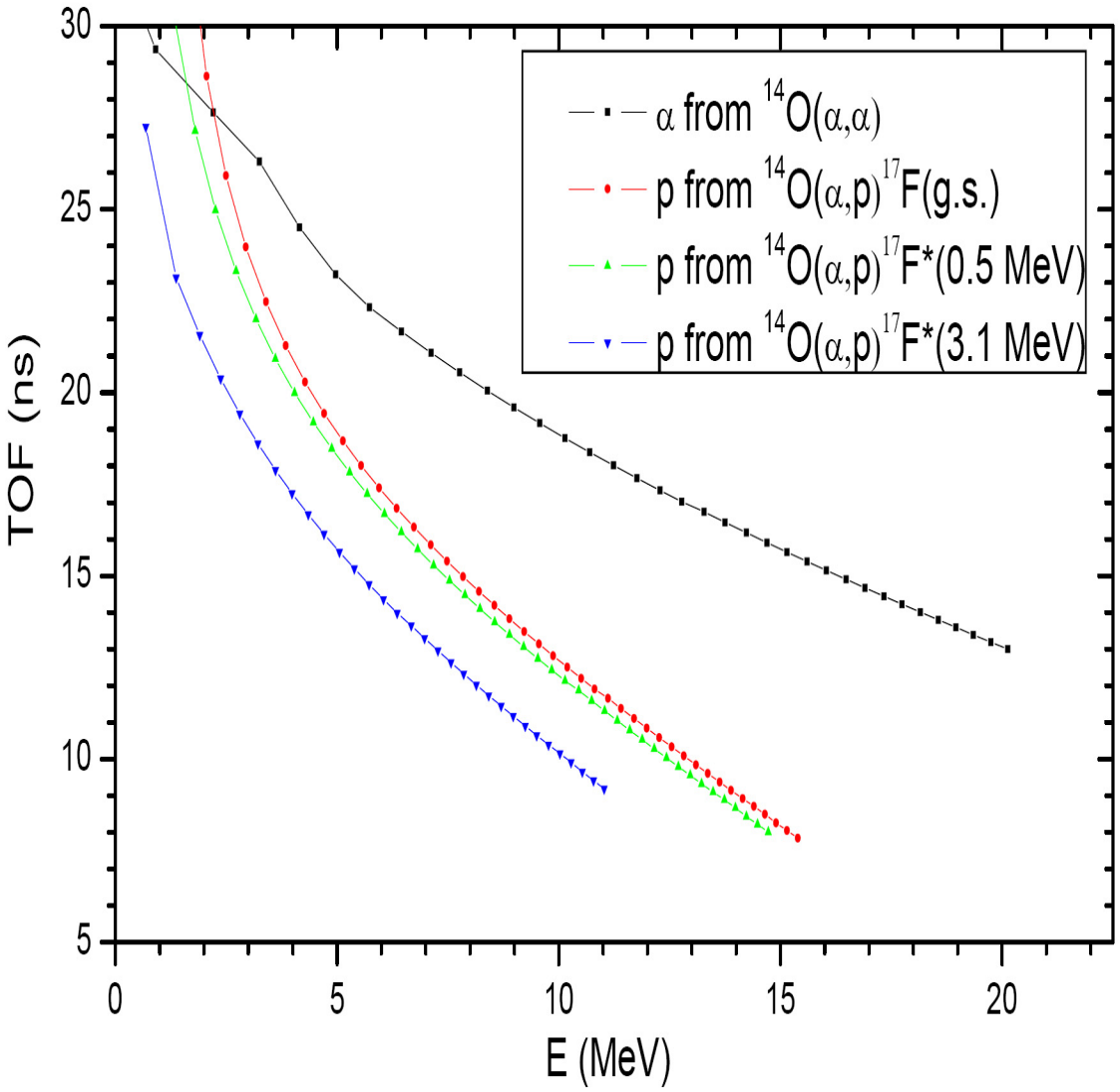

Fig. 25. A simulation for the TOF-E spectrum in the $\alpha+{}^{14}$O interaction. The mapping is one-to-one almost everywhere. The crossing of the lines corresponding to α particles and protons is due to larger energy loss of α particles in the gas. Protons from ${}^{17}\mathrm{F}^{*} \rightarrow p+{}^{16}$O were not considered here but they do not affect the conclusion.

where ρ is the density of the target, $\mathrm{d}x$ is the thickness of the target and the energy of projectile is in the range $(E_L, E_L + \mathrm{d}E_L)$. Then

$$\begin{aligned}
\sigma_C &= \frac{\sqrt{1-\gamma^2\sin^2\theta_L}}{\left(\gamma\cos\theta_L+\sqrt{1-\gamma^2\sin^2\theta_L}\right)^2}\,\frac{\mathrm{d}N}{I\rho\,\mathrm{d}\Omega_L\,\mathrm{d}x\,\mathrm{d}E_C} \\
&\simeq \frac{\sqrt{1-\gamma^2\sin^2\theta_L}}{\left(\gamma\cos\theta_L+\sqrt{1-\gamma^2\sin^2\theta_L}\right)^2}\,\frac{\Delta N}{I\rho\,\Delta\Omega_L}\frac{1}{\mathrm{d}x\mathrm{d}E_C} \\
&\simeq \frac{\sqrt{1-\gamma^2\sin^2\theta_L}}{\left(\gamma\cos\theta_L+\sqrt{1-\gamma^2\sin^2\theta_L}\right)^2}\,\frac{\Delta N}{I\rho\,\Delta\Omega_L\,\Delta E_d^2} \\
&\quad\times\frac{\mathrm{d}E_d}{\mathrm{d}x}\frac{\mathrm{d}E_d}{\mathrm{d}E_C},
\end{aligned} \tag{4.13}$$

where ΔE_d is the energy step of the detecting system. The $\Delta\Omega$, $\mathrm{d}E_d/\mathrm{d}x$, and $\mathrm{d}E_d/\mathrm{d}E_C$ are functions of projectile energy, density of the target, and the mass and charge of the projectile particles and target. They can be obtained by calculating the energy loss behavior of the projectile and recoil particles in the target. In many references, the cross section was given by integrating over the $\Delta E_C = \frac{\mathrm{d}E_C}{\mathrm{d}E_d}\Delta E_d$ energy interval. Then, it could be written as

$$\begin{aligned}
\bar{\sigma}_C &\equiv \sigma_C\,\Delta E_C \\
&\simeq \frac{\sqrt{1-\gamma^2\sin^2\theta_L}}{\left(\gamma\cos\theta_L+\sqrt{1-\gamma^2\sin^2\theta_L}\right)^2} \\
&\quad\times\frac{\Delta N}{I\rho\,\Delta\Omega_L\,\Delta E_d}\frac{\mathrm{d}E_d}{\mathrm{d}x}.
\end{aligned} \tag{4.14}$$

In elastic scattering, $\gamma = 1$ and the formula can be simplified to

$$\sigma_C^{(el)} \simeq \frac{1}{4}\,\frac{\Delta N}{I\rho\,\Delta\Omega_L\,\Delta E_d^2}\frac{\mathrm{d}E_d}{\mathrm{d}x}\frac{\mathrm{d}E_d}{\mathrm{d}E_C}, \tag{4.15}$$

and

$$\bar{\sigma}_C^{(el)} \simeq \frac{1}{4}\frac{\Delta N}{I\rho\,\Delta\Omega_L\,\Delta E_d}\frac{\mathrm{d}E_d}{\mathrm{d}x}. \tag{4.16}$$

3. Energy and time resolution in the SPORTTIK method

Energy and TOF resolution are the important considerations in the SPORTTIK method. Consider a reaction with a beam energy spread ΔE_a. Due to the energy spread, the resonance interaction will happen at different positions in the target. The difference in distance, $\Delta x^{(E_a)}$, is given by [45]

$$\Delta x^{(E_a)} \approx \frac{\Delta E_a}{\mathrm{d}E_a/\mathrm{d}x}, \tag{4.17}$$

where dE_a/dx is the specific energy loss of the beam nuclei in the target. The detected energy spread of the recoil particles, $\Delta E_d^{(E_a)}$, corresponding to the interval $\Delta x^{(E_a)}$ is

$$\Delta E_d^{(E_a)} \approx \Delta E_a \frac{\mathrm{d}E_b/\mathrm{d}x}{\mathrm{d}E_a/dx}, \tag{4.18}$$

where, $\mathrm{d}E_b/\mathrm{d}x$ is the specific energy loss of the recoil light nuclei in the target. Since the Q-value of the reaction is,

$$Q = (\frac{A_a}{A_B}-1)E_a + (\frac{A_b}{A_B}+1)E_b - \frac{2(A_aA_bE_aE_b)^{1/2}\cos\theta_L}{A_B}, \tag{4.19}$$

ΔQ can be written as

$$\begin{aligned}\Delta E_b &\approx \Delta Q\left[\frac{A_b}{A_B}+1-\frac{(A_aA_bE_aE_b^{-1})^{1/2}\cos\theta_L}{A_B}\right]^{-1}\\ &= 2\,\Delta Q\left[\frac{Q}{E_b}+\frac{A_b}{A_B}+1-(\frac{A_a}{A_B}-1)\frac{E_a}{E_b}\right]^{-1}\\ &\equiv \Delta E_d^{(Q)},\end{aligned} \tag{4.20}$$

where $\Delta E_d^{(Q)}$ is the detected energy difference of the recoil particles due to the Q-value difference ΔQ.

In a resonance reaction, the cross section dramatically depends on the system energy. If $\Delta E_d^{(Q)} > \Delta E_d^{(E_a)}$, two resonance peaks can be separated. Considering Eqs. (4.18) and (4.20), we have:

$$\Delta Q > \frac{\Delta E_a}{2} \frac{\mathrm{d}E_b/\mathrm{d}x}{\mathrm{d}E_a/dx} \left[\frac{Q}{E_b} + \frac{A_b}{A_B} + 1 - (\frac{A_a}{A_B} - 1) \frac{E_a}{E_b} \right]. \tag{4.21}$$

For $A_b << A_B$ and $A_a \approx A_B$, at least

$$\Delta Q > \frac{\Delta E_a}{2} \frac{\mathrm{d}E_b/\mathrm{d}x}{\mathrm{d}E_a/dx} (\frac{Q}{E_b} + 1) \tag{4.22}$$

is required to separate the peaks. Since in the SPORTTIK approach $Z_a > Z_b$ and $\mathrm{d}E/\mathrm{d}x \propto Z^2$. The beam spread is "suppressed" by the factor $\frac{\mathrm{d}E_b/\mathrm{d}x}{\mathrm{d}E_a/dx}$ which is $<< 1$ in many cases.

From equation 4.3, the ΔTOF can be rewritten as

$$\Delta TOF \approx \frac{L_{PQ}}{\bar{v}_a} - \frac{L_{PS}}{\bar{v}_b}, \tag{4.23}$$

where $\bar{v}_a/\bar{v}_b$ is the average speed of the beam/recoil particle in the corresponding intervals. Since $\bar{v}_a$ and $\bar{v}_b$ are determined by the Q-value of the reaction, Z and A of target and beam, they can not be tuned. However one can decrease the gas target density, therefore increasing the distances L, to increase ΔTOF. For example, in Fig. 25 for helium gas at 0.85 atm and 10 MeV detected proton energy, the $\Delta TOF^{(gas)}$ is about 3 ns. Suppose one compresses the helium gas one thousand times, to get a "solid" helium target. With the same condition except this "solid" target, the $\Delta TOF^{(solid)}$ is about about 3 ps, one thousand times smaller than $\Delta TOF^{(gas)}$ as Eq. 4.3 suggests. This would be too small to be measured. Therefore, for solid targets, one would have to change the experimental setup to get the SPORTTIK method to work. A possible schematic for solid target experiment with the SPORTTIK approach is shown in Fig. 26. The thin solid targets are aligned separately to increase the ΔTOF

to a measurable level.

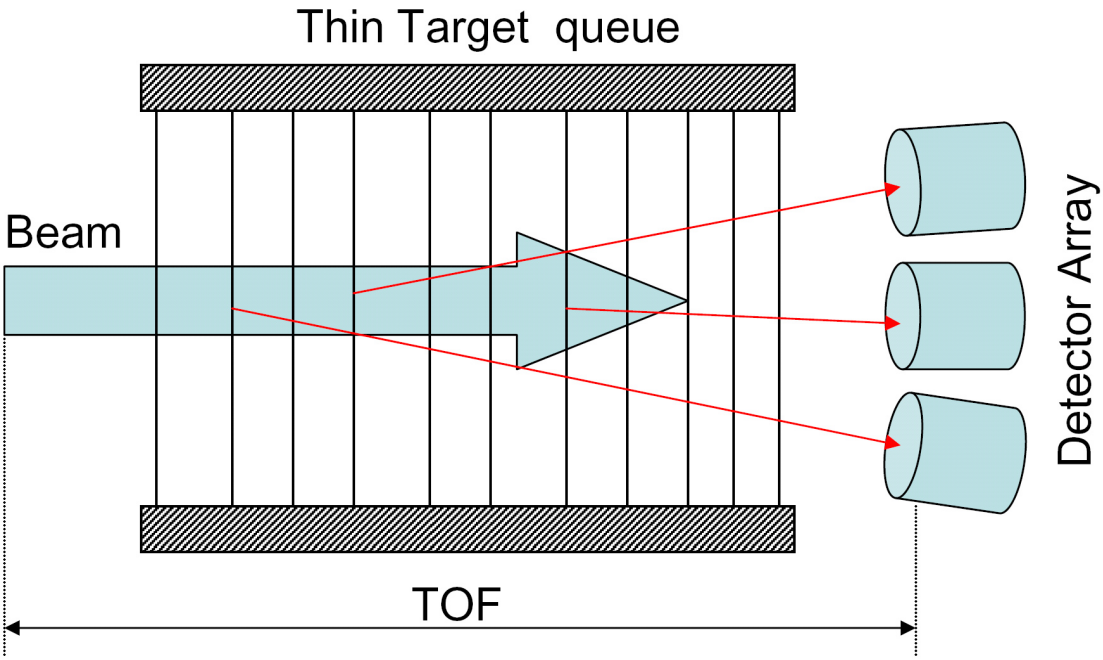

Fig. 26. A possible experimental layout for experiments with solid targets and the SPORTTICK approach.

There are some other parameters which can spoil the energy and time resolution, such as the angular spread of the beam. However, by designing the experiment carefully, the excitation functions can be measured with acceptable precision in a single run which overcomes the low beam intensity problem of a RIB.

B. The R-matrix method

To analyze low energy resonance reaction data, R-matrix theory, which was developed by Wigner [46] and his collaborators for the analysis of resonance reactions, can be used. For a history of R-matrix theory, see Ref. [47].

The main goal of the R-matrix method is to parameterize some experimentally known quantities, such as angular distributions, and cross sections, with a small set

of parameters. In R-matrix theory, the space is divided into two regions [47], the "external" region, where only the Coulomb force remains and the "internal" region, where nuclear forces dominate and the physics of the problem is derived from the properties of poles. The external region provides parameters like the collision matrix, penetration factors, etc. The internal region provides the parameters like energy levels, widths, etc. The internal and external regions connect with each other on the boundary of the compound nucleus. The two regions can be separated due to the fact that the nuclear force is short range, and the nucleus has a reasonably well defined radius.

This R-matrix method had been widely used in resonance reactions, especially for low level density resonance studies. If the level density is low, the cross section can be given in terms of parameters with the inclusion of suitable interference terms. However, when more than a few resonances are required, the number of channels involved increases rapidly, and the method can not be used efficiently.

For simplicity, consider a zero-spin single-channel system [48]. The Schrodinger equation for this is

$$\{H - E\}\psi_{lm} = 0. \tag{4.24}$$

In the region where the nuclear force dominates, we find a base set of solutions

$$\varphi^i_{lm} = \frac{u^i_l(\rho)}{\rho} Y_{lm}(\Omega_\rho), \tag{4.25}$$

which are the solutions of the equation

$$\{H - E^i_l\}\varphi^i_{lm} = 0, \tag{4.26}$$

where E^i_l are the eigenvalues. The u^i_l are orthonormal

$$\int_0^\infty u^i_l(\rho) u^j_l(\rho)\, \mathrm{d}\rho = \delta_{ij}. \tag{4.27}$$

The boundary condition of this equation is

$$\left(\frac{du_l^i(\rho)}{d\rho}\right)_{\rho=a} = 0. \tag{4.28}$$

In the external region, the general solution Φ_l may be expressed as a linear combination of the linearly independent I_l and U_l waves:

$$\Phi_l \sim I_l - U^l O_l, \tag{4.29}$$

where I_l is the incoming flux, and O_l is the unit outgoing flux. U_l is the amplitude of the outgoing flux. It is called the *collision or scattering function*. U_l may be expressed in terms of a phase shift δ_l as

$$U_l \equiv e^{2i\delta_l}, \tag{4.30}$$

where

$$\delta_l = tan^{-1}[R_l P_l / 1 - R_l S_l] - \phi_l + \omega_L. \tag{4.31}$$

For spinless particles, the differential cross section of the reaction is (Ref. [49], page 237):

$$\frac{\mathrm{d}\sigma}{\mathrm{d}\Omega} = \frac{1}{4k^2}\left|\sum_l (2l+1)(1-U_l)P_l(\cos\theta)\right|^2, \tag{4.32}$$

And the integrated cross section is

$$\sigma = \int \frac{\mathrm{d}\sigma}{\mathrm{d}\Omega}\mathrm{d}\Omega = \frac{\pi}{k^2}\sum_l (2l+1)\left|1-U_l\right|^2, \tag{4.33}$$

where P_l is the Legendre polynomial. the first several Legendre polynomials ($P_l(\cos\theta)$) are listed below:

$$P_0(x) = 1, \tag{4.34}$$

$$P_1(x) = x, \tag{4.35}$$

$$P_2(x) = \frac{1}{2}(3\,x^2 - 1), \tag{4.36}$$

$$P_3(x) = \frac{1}{2}(5\,x^3 - 3\,x), \tag{4.37}$$

$$P_4(x) = \frac{1}{8}(35\,x^4 - 30\,x^2 + 3). \tag{4.38}$$

The first several $|P_l(\cos\theta)|^2$ are shown in Fig. 27. Since the different polynomials have different angular dependences, then so do the cross sections. Therefore, studying the angular distribution of particular states helps to determine the l-value of those states. However, when the widths of two or more states are comparable to the energy separation between them, interference plays a large role. If this is the case, the angular dependence of one specific state will not only be determined by the l-value of this state, but also by the angular dependence of other nearby states.

The total wave function of Φ_{lm} is

$$\Phi_{lm} = \frac{g_l(\rho)}{\rho} Y_{lm}(\Omega_\rho), \tag{4.39}$$

where

$$g_l(\rho) = \sum_{i=1}^{N} A_i^l u_l^i(\rho) \qquad , \tag{4.40}$$

for $\rho \leq a$, and

$$g_l(\rho) = i^{l+1}(\pi(2l+1)/v)^{1/2}[I_l(k\rho) - U^l O_l(k\rho)]/k, \tag{4.41}$$

for $\rho > a$. Multiplying 4.24 by φ_{lm}^{i*}, and 4.26 by Φ_{lm}^*, and subtracting both equations gives

$$A_i^l = \frac{\hbar^2}{2\mu m_N} \frac{u_i(a) g'(a)}{E_i - E}. \tag{4.42}$$

Using the continuity of the wave function 4.40 at the boundary provides

$$g(\rho) = G(\rho, a) a g'(a), \tag{4.43}$$

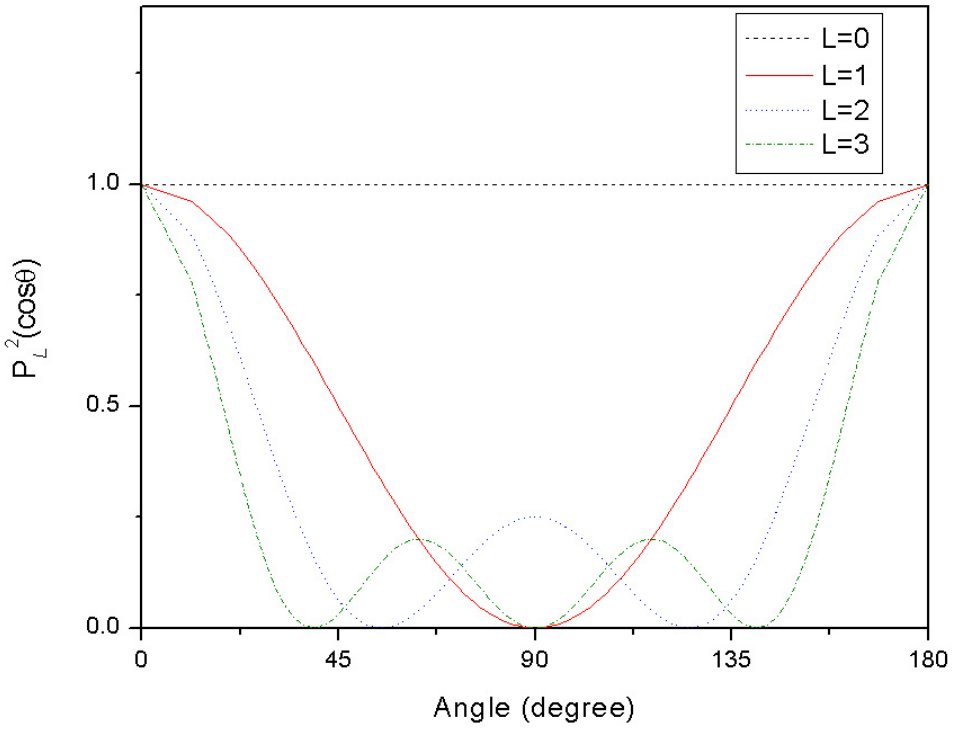

Fig. 27. Angular dependence of cross sections for isolated resonance states in the case of spinless particles, where the cross section is proportional to the square of the Legendre Polynomials. L is the order of the Legendre Polynomial.

where the $G(\rho, a)$ is Green's function which is defined as

$$G(\rho, a) \equiv \frac{\hbar^2}{2\mu m_N a} \sum_i \frac{u_i(a)u_i(\rho)}{E_i - E}. \tag{4.44}$$

Then, the R-matrix is defined as

$$R_l = \sum_i \frac{(\gamma_l^i)^2}{E_l^i - E} \equiv \sum_i R_l^i, \tag{4.45}$$

where the formal reduced width $(\gamma_l^i)^2$ is given by

$$(\gamma_l^i)^2 = \left(\frac{\hbar^2}{2\mu m_N a}\right)^{1/2} u_l^i(a). \tag{4.46}$$

The reduced widths are correlated to the partial widths

$$\Gamma_l^i = 2P_l^i \cdot (\gamma_l^i)^2, \tag{4.47}$$

where P_l^i is the penetrability factor when the particle passes through the Coulomb and orbital momentum barrier. The penetrability factor is given by the equation

$$2P_l^i = \frac{kr}{F_l^2 + G_l^2}, \tag{4.48}$$

where k is wave number, and F and G are the regular and irregular Coulomb functions respectively [47]. The asymptotic behavior at large r is

$$F_l \approx \sin[kr - \eta \log(2kr) - \frac{l\pi}{2} + \sigma_l], \tag{4.49}$$

and

$$G_l \approx \cos[kr - \eta \log(2kr) - \frac{l\pi}{2} + \sigma_l], \tag{4.50}$$

where $k = mv/\hbar$ and the Coulomb phase shift and the Coulomb parameter are given by

$$\eta = Z_1 Z_2 e^2/hv. \tag{4.51}$$

From an experiment, we can obtain a differential cross section spectrum for a reaction as a function of energy and angle. By fitting the experimental data with the R-matrix method, we obtain information about spin-parities, energies and widths of the excited states of a compound nucleus. For example, one can get the reduced width from an α resonance scattering reaction by an R-matrix fit. If the reduced width is very large, this state is considered to be an α cluster state.

C. R-matrix fit result

1. Assumptions

The following assumptions were used when the experimental data were analyzed.

a. The reaction is dominated by resonance reactions

There are two extremes to consider for the nuclear reactions, direct reactions and compound nuclear reactions [49]. A direct reaction involves a short time delay whose order of magnitude is the time that it would take a projectile and/or the emerging particle simply to traverse the nucleus. The reaction has "finger prints" like the cross section has a weak dependence on energy and the angular distribution is strongly anisotropic. A compound nuclear reaction involves a longer interaction time, the cross section changes rapidly with energy (i.e. resonance reaction), and the angular distribution in the c.m. system is symmetrical about 90°.

In this experiment, the excitation energy is small (about 11 MeV maximum in the c.m.). Therefore, to a good approximation, the resonance reaction mechanism will dominate. If the experimental data manifest strong energy dependence, we can assume a resonance character for the interaction.

b. α decay to $^{14}O^*$ is small

As shown in Fig. 28, the first excited state of $^{14}O^*$ is at 5.17 MeV. The maximum excitation energy of ^{18}Ne which could be populated with the experimental conditions at TAMU was about 12.5 MeV. The maximum Q-value of the $^{18}\mathrm{Ne} \rightarrow \alpha + ^{14}\mathrm{O}^*(5.17\,\mathrm{MeV})$ is only about 2.2 MeV while the Coulomb barrier for the decay is about 4 MeV. Considering that many reaction channels are open and the corresponding penetrabilities are large, the decay to the first excited state of ^{14}O should be small. The same is true for population of the first excited of ^{16}O at 6.049 MeV by $2p$ emission.

2. The R-matrix fit results for ^{18}O and ^{18}Ne

As was stated before, the specific aim of the study of resonance elastic scattering of ^{14}O and ^{14}C on helium was to obtain spectroscopic information on the mirror nuclei, ^{18}O and ^{18}Ne. As described in Chapter II, we used the time of flight method to separate protons and alpha particles in the $^{14}\mathrm{O} + \alpha$ experiment. In spite of the additional beam analysis (see Chapter III), the ^{7}Be contaminants still appeared at zero degrees. However at angles larger than 3° (laboratorial system), the ^{7}Be peak was much weaker, and could be separated by the TOF method. The experiment using a clean ^{14}C beam was made at Florida State University, and is discussed in Appendix B. The excitation functions of both reactions were obtained from the raw data with the method shown in the last section.

Figure 29 presents an R-matrix fit of the low energy part of the $^{14}\mathrm{O}+\alpha$ excitation function, using parameters of 1^- and 3^- resonances from the analysis of the $^{14}\mathrm{C}+\alpha$ excitation function. Some tentative parameters for the resonances are given in Table

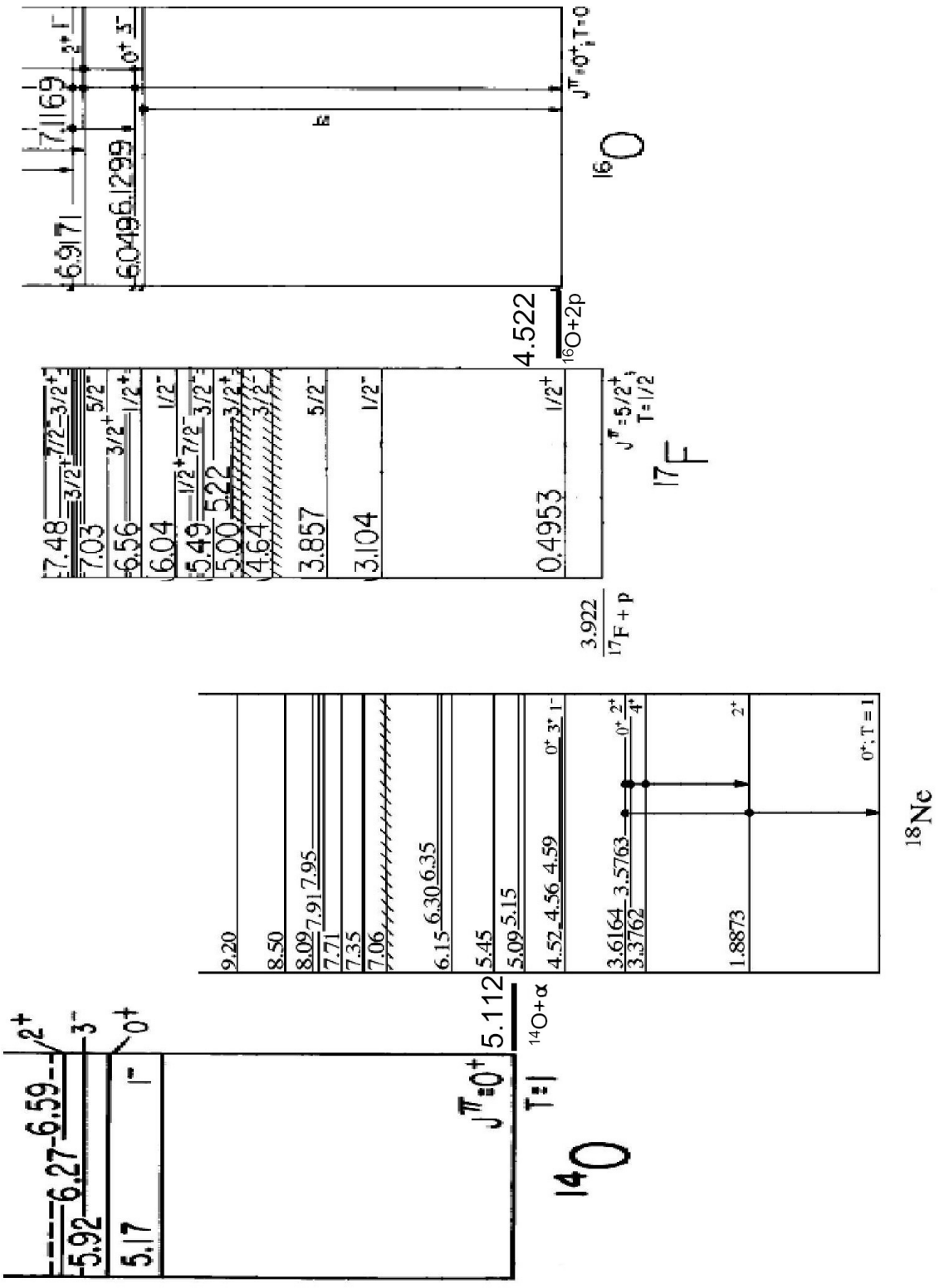

Fig. 28. Energy level of ^{18}Ne.

IV and Table V. The value θ^2 is defined as follows

$$\theta^2 = \gamma_\alpha^2/\gamma_{sp}^2, \tag{4.52}$$

where γ_α^2 is the reduced width, and γ_w^2 is the single particle limit (or Wigner limit) width (Eq. 1.1). One can see a surprising difference in their excitation functions, as shown in Fig. 30 where a comparison is given.

Table IV. A list of the tentative parameters for the α-cluster states in the ^{18}O

J^π	E_{ex} (MeV)	Γ (MeV)	γ_α (MeV)	Θ^2
1^-	9.058	0.353	0.51	0.475
3^-	9.417	0.166	0.48	0.421
3^-	9.699	0.219	0.52	0.494
1^-	9.814	0.426	0.40	0.292
5^-	11.646	0.048	0.30	0.164
6^+	11.686	0.027	0.45	0.370
5^-	12.235	0.103	0.31	0.175
6^+	12.475	0.056	0.40	0.292

It is clear that the fits for both systems are not good. Indeed the analysis of the scattering data appears to be very difficult. This difficulty was recognized by the authors of pioneering experiments [50, 51] where $\alpha + ^{14}$ C scattering was measured. For example, in Ref. [50], the authors claimed that "Phase-shift analysis of the angular distributions indicated interference from very broad levels having low spins. The existence of such a background makes a quantitative analysis *very difficult and ambiguous*." In more recent work [52], the authors tried to analyze the old data [50] and also claimed large uncertainties. Similar problem were found in a very recent experiment [53] (Jan, 2007), where R matrix analysis of the spectra from the β-α

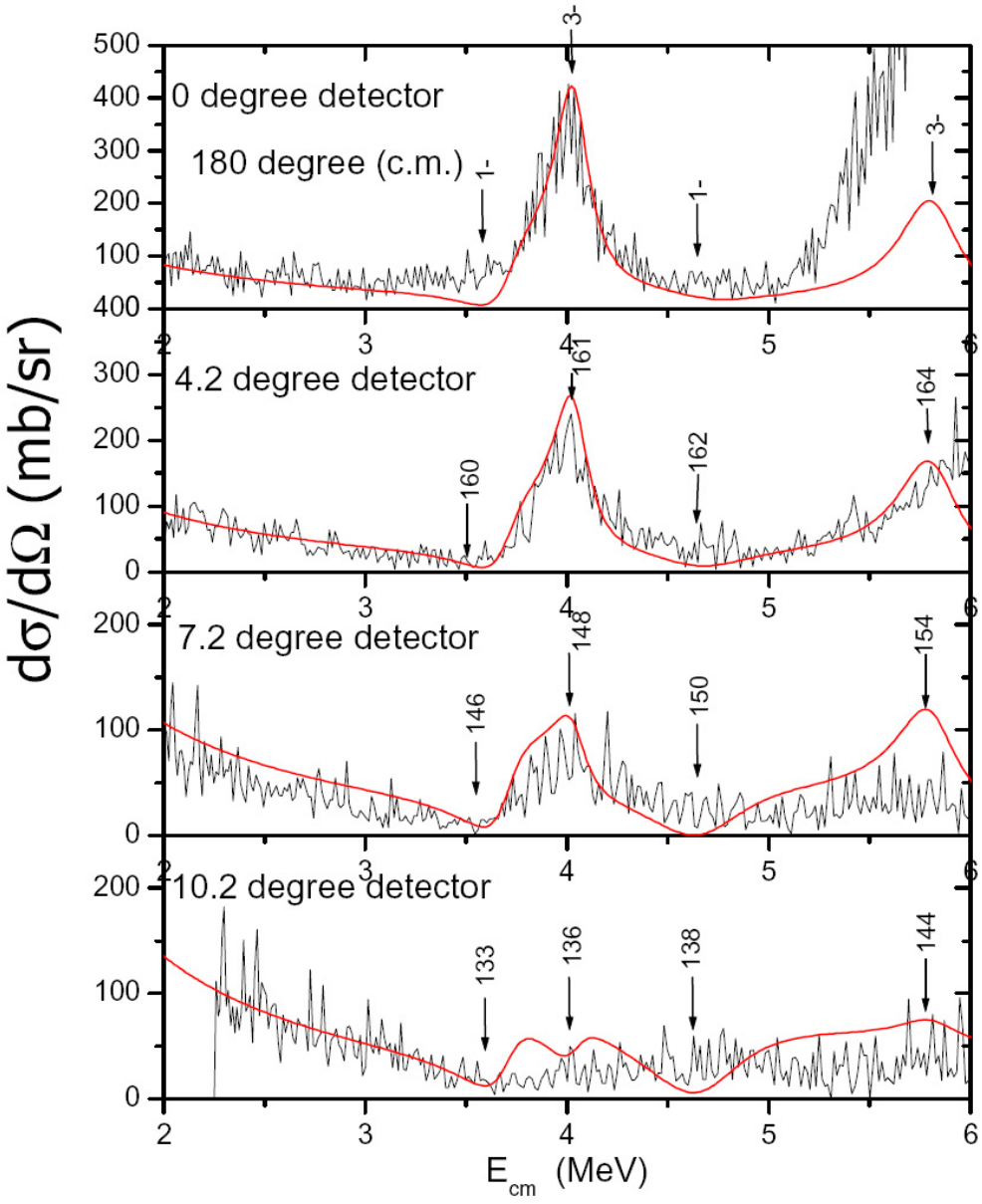

Fig. 29. R-matrix fit for the spectra of $^{14}\mathrm{O} + \alpha$ at different angles.

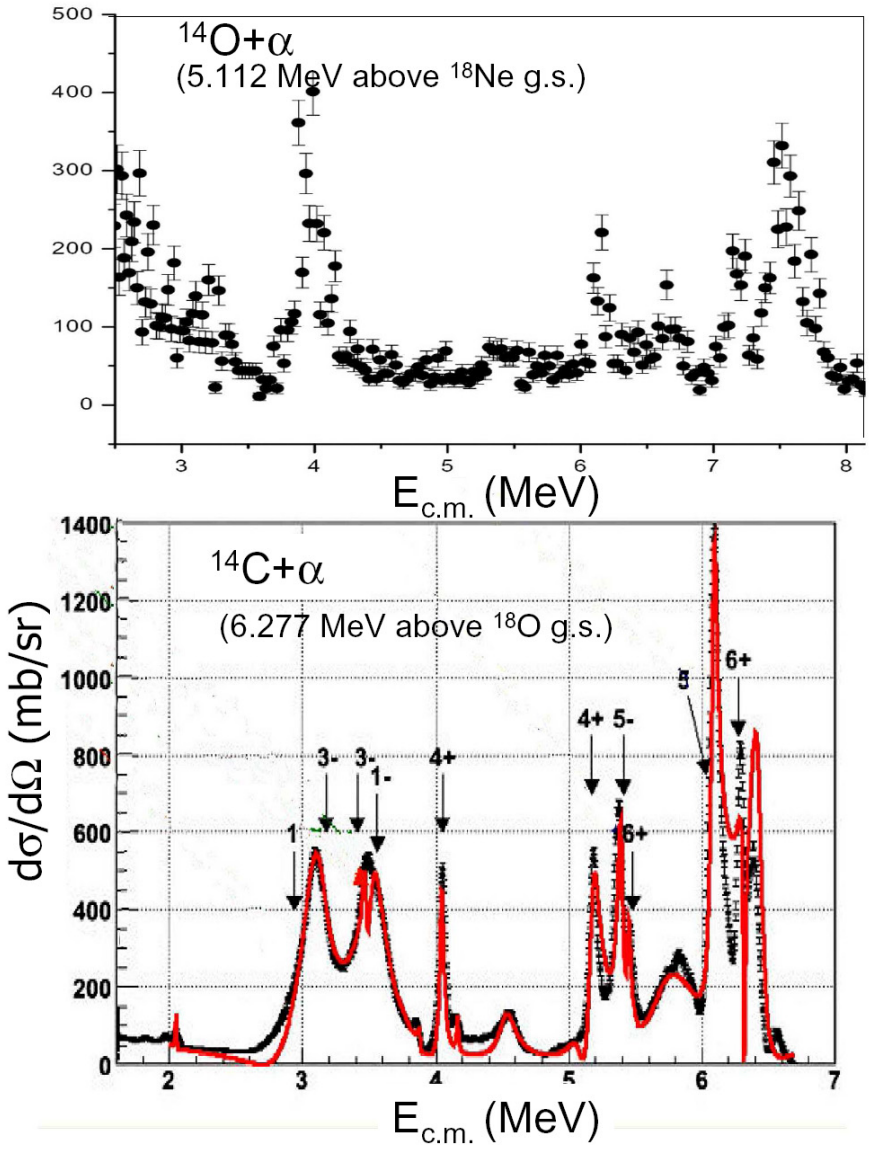

Fig. 30. A comparison of the ^{14}O(α,α) spectrum with the ^{14}C(α,α) spectrum.

coincidences of ^{18}N decay was made. Due to selection rules in the β-α coincidence, only 1^- states present, and still the fits appeared to be poor.

The conclusion from this is that many alpha cluster states in ^{18}O are broad and they are overlapping. That is why one can observe structure but not separated peaks. For instance, the second strong peak in the $^{14}\mathrm{C}+\alpha$ spectrum, which has been interpreted as a single 3^- state [52] appears to be a group of overlapping 1^-, 2^+ and 3^- (relatively weak) levels. At the present time, we can state that there are strong peaks in the ^{14}O+α and ^{14}C+α spectra, which is an evident manifestation of alpha cluster structure in the A=18 nuclei. This is especially evident in the case of the ^{14}O+α interaction. The threshold for α decay in ^{18}Ne is higher than that for p and $2p$ decay. Therefore the large cross section is clear evidence for the dominance of the partial α decay width. These results tend to contradict earlier publications which questioned the role of α-cluster structure in $A = 18$ nuclei [54].

We also found that in the first strong peak in the ^{14}C+α spectrum (Fig. 30) the main contribution comes from the presence of broad 1^- and 3^- levels. The presence of the broad 1^- level at an excitation energy about 9 MeV in the ^{18}O and ^{18}Ne spectra is important for astrophysics as well as possible experiments on parity violation in the decay of ^{18}O (see discussion in Ref. [53]).

Table V. A list of the tentative parameters for the α-cluster states in the ^{18}Ne

E_{ex} (MeV)	J^{π}	γ_{α} (MeV)
8.85	1^{-}	0.25
9.25	3^{-}	0.53
9.49	3^{-}	0.21
11.31	5^{-}	0.33
11.92	3^{-}	0.15
12.24	6^{+}	0.29
12.32	5^{-}	0.28

CHAPTER V

TWO PROTON EMISSION FROM THE $^{14}O + \alpha$ INTERACTION

With the accumulation of 2×10^{10} ^{14}O particles on the target, about 4800 two proton coincidence events were observed from the $^{14}O(\alpha, 2p)$ interaction. As is shown in Table III, less than 2 events correspond to random 2 proton coincidences.

A. Cross section for $(\alpha, 2p)$

The large area silicon detectors used here provided only a crude measurement of angular distribution. Furthermore, the spin-parities of most states were not known. To calculate the total cross section for the resonance peaks in the $^{14}O(^4He, 2p)^{16}O$ reaction, an assumption was made that the angular distribution of the resonances were isotropic. Therefore the total cross section of a resonance can be estimated as

$$\sigma_c \approx \frac{dN}{IN_t} \left(\frac{4\pi}{d\Omega_c} \right)^2, \tag{5.1}$$

where I is the beam intensity, N_t is the target intensity, and $d\Omega_c$ is the solid angle in c.m. system. The term $(4\pi/d\Omega_c)^2$ is due to the fact that two protons were emitted and the detection possibility for each one of them is $4\pi/d\Omega_c$.

The details of the calculation of the differential cross section for a 3-body reaction with the Thick Target Inverse Kinematics method are given in the Appendix A.

B. Sequential decay

Since a thick target was used, the situation for $2p$ decay is more complicated due to the involvement of many resonance states in ^{18}Ne, intermediate resonance states in ^{17}F, and poor energy and angular resolution. To find the decay mechanisms of the

3-body reactions, the Dalitz plot was used to analyze the data.

The Dalitz plot, which was introduced in 1953 [55], is a two-dimensional plot which represents the entire phase space of a three-body final state. It provides a good way to distinguish whether a three body decay proceeds as two successive two-body decays, or proceeds directly into the three decay products. By the pattern of the Dalitz plot, one can distinguish the different decay mechanisms.

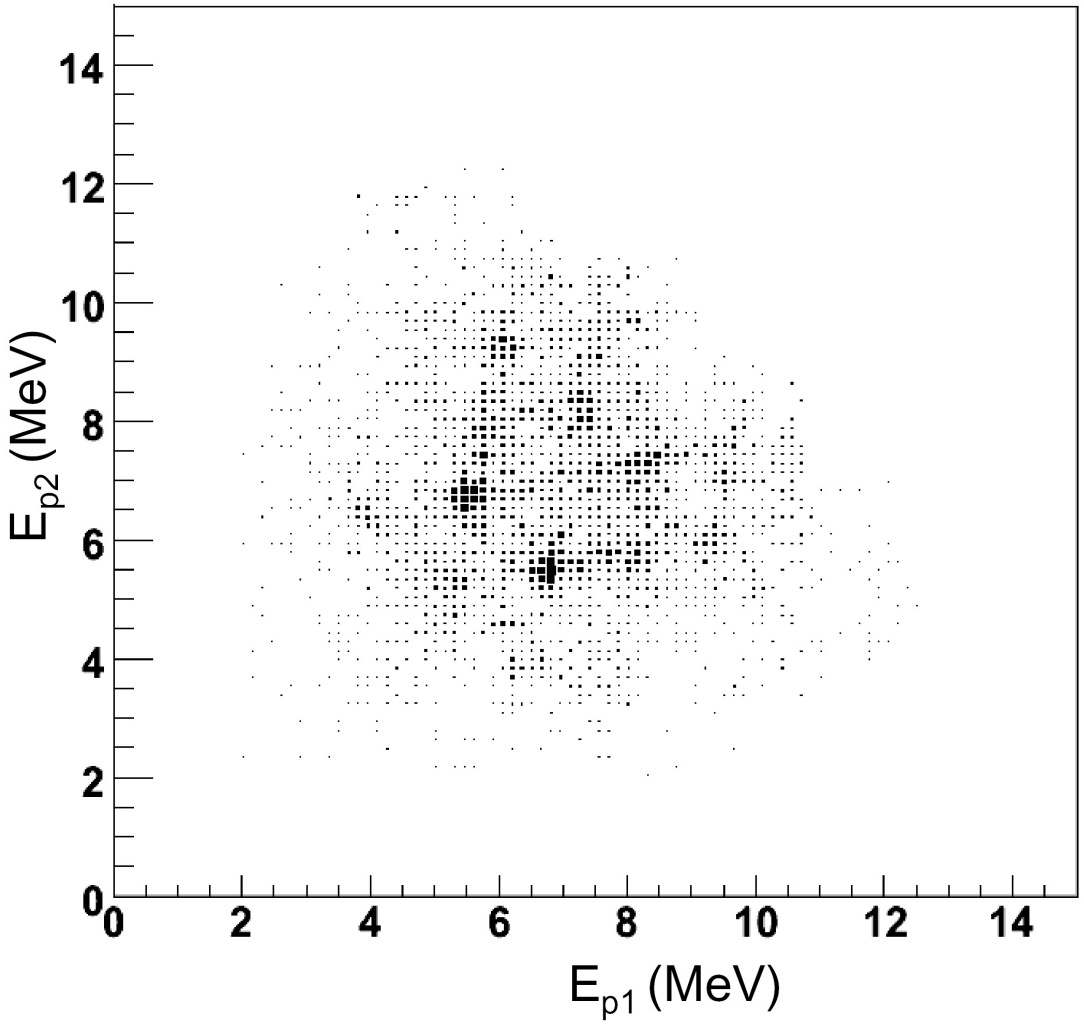

Fig. 31. the Dalitz plot for the coincident protons from the $^{14}\mathrm{O}(^{4}\mathrm{He}, 2p)^{16}\mathrm{O}$ reaction. The energy of protons are given in lab system.

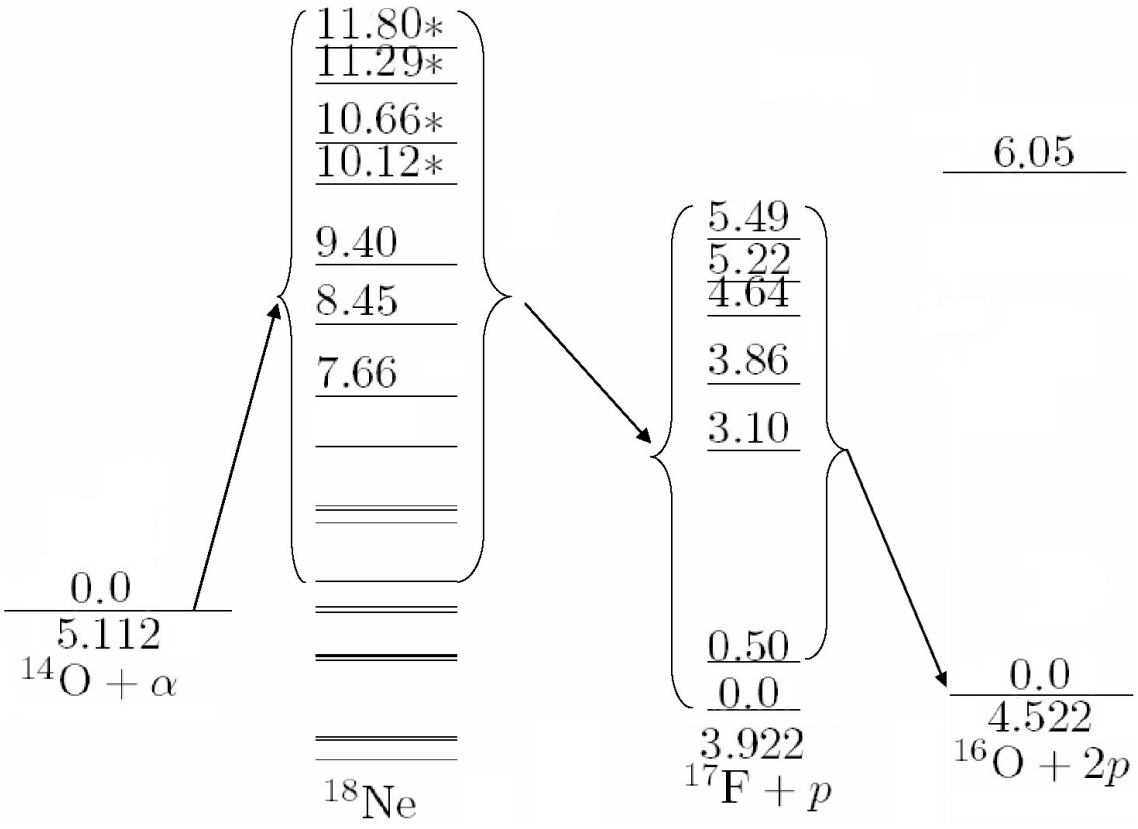

Fig. 32. Energy level scheme for proton decays. Levels marked by * have not been reported in the literature.

The Dalitz plot of the two proton events measured here is presented in Fig. 31 (i.e. proton energies as coordinates). As is shown in the figure, most of the events are concentrated in spots. This is a signature for sequential proton decay of resonance states in $^{18}Ne^*$ to excited states in $^{17}F^*$ and then to the ground state in ^{16}O (Fig. 32). As noted above, we do not expect to see decays populating the first excited state in ^{16}O due to the low energy ($E_{cm} = 12.5\,\mathrm{MeV}$) used here and no evidence was found for them in the data.

Figure 33 presents the excitation function for the $^{14}O(\alpha, 2p)^{16}O$ reaction. The cross sections are listed in table VI. It is evident from the figure that resonance population of levels in ^{18}Ne dominates. The 8.45 MeV level was observed before in

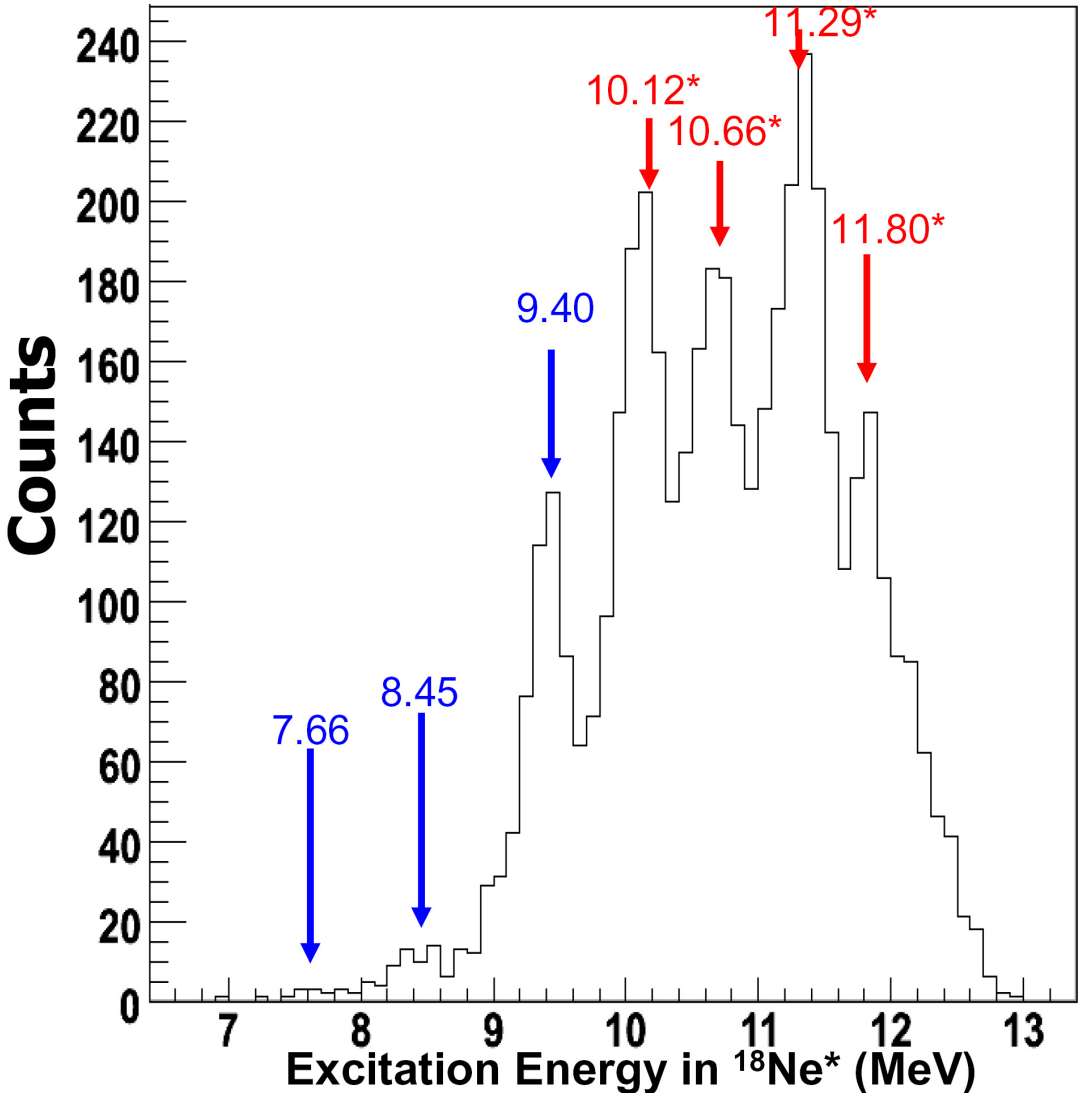

Fig. 33. Spectrum of ^{18}Ne* states which decay through 2-proton emission. The cross section of the 8.45 MeV level is about 0.73 mb, and the 11.29 MeV level is about 49.9 mb.

the ^{16}O(^{3}He, n) reaction [56], and the 9.4 MeV level is likely the 9.2 MeV which was found in the ^{20}Ne(p, t) reaction [56]. None of the other levels have been reported in the literature. No spin parity assignments are known for the levels above 8 MeV in ^{18}Ne. As was mentioned before, the dominant proton decay of these levels is to excited states in ^{17}F.

Cross sections of the resonance peaks were found using Eq. 5.1, and the results are shown in Table VI and VII.

Table VI. Energy levels in ^{18}Ne* which contribute to $2p$ emission.

Energy (MeV)	$J\pi$	Width (keV) from references	Width (MeV) this work (FWHM)	cross section (mb)[1]
7.66	$(1-, 2+)$		0.31	0.11
8.45		< 120 [3]	0.47	0.73
9.40	$3-$		0.42	9.92
10.12 [2]			0.54	29.2
10.66 [2]			0.73	25.9
11.29 [2]			0.66	49.9
11.80 [2]			0.52	42.4

[1]calculated with assumptions, see the text.

[2]This work.

[3]From Ref.[56].

Obtaining the excitation energy of the intermediate states in ^{17}F was difficult. Suppose detector a records a proton (p_a), and detector b records another proton (p_b). To fix the excitation energy in ^{17}F it is important to know which proton is from the first step, and which is from the second step in the

$$^{18}\mathrm{Ne}^* \rightarrow p_1 + {}^{17}\mathrm{F}^* \rightarrow p_1 + {}^{16}\mathrm{O} + p_2$$

Table VII. The decay parameters of $^{18}Ne^*$ levels

Energy Level of $^{18}Ne^*$	Energy Level of intermediate state $^{17}F^*$	Cross Section
MeV	MeV	mb
8.45	2.57[1]	0.73 ($2p$)
9.40	3.17	4.7
	3.90	5.4
10.12	3.18	13.0
	3.90	9.4
10.66	3.16	13.5
	3.90	4.4
11.29	3.19	7.4
	3.90	28.4
	5.19	7.9

two step process. The experimental setup could not be used to distinguish them since the time delay between the "first" and "second" proton is extremely short (about 10^{-15} second or less). Therefore, an assumption had to be made before the energy levels of ^{17}F* could be determined. To account for this ambiguity, the excitation energy of ^{17}F* was calculated twice with the roles of the protons reversed. The result is shown in Fig. 34. By projecting on the axis in the figure, we find that some groups correspond to known ^{17}F levels, and some do not. The former means that the decay is sequential, and the later means that either the wrong sequence of the protons was taken or the decay is not sequential. This is more clearly seen in Fig. 35 where a projection of the two dimensional plot of Fig. 34 onto the axis of calculated excitation energies in ^{17}F is presented. Some "ghost" peaks in the excitation energies of ^{17}F show up as a result of choosing the wrong order of the protons in the decay process. For example, in the panel for $E_{^{18}Ne^*} = 9.40\,\mathrm{MeV}$, there is a "ghost"peak at $E_{^{17}F^*} \approx 2.2\,\mathrm{MeV}$. If the sequence of the two protons is reversed, we get the excitation energy of $E_{^{17}F^*}$ at the known location of 3.86 MeV. Figure 36 is similar to Fig. 35 with an important difference—the known levels in ^{17}F have been taken into account to define the order of the protons in the sequential decay process.

As is seen in Fig. 36, most levels in ^{18}Ne undergo sequential proton decay through excited states in ^{17}F. The decay of the ^{18}Ne* level at 8.45 MeV demonstrates a different feature. This decay will be considered in the next section.

C. The $2p$ decay of ^{18}Ne*(8.45 MeV)

In the discussion above, we found that there is no evidence that ^{18}Ne*(8.45 MeV) undergoes proton decay to the known states in ^{17}F, including ^{17}F*(3.104 MeV) and ^{17}F*(3.857 MeV), even if the sequence of the two protons are changed. Therefore we

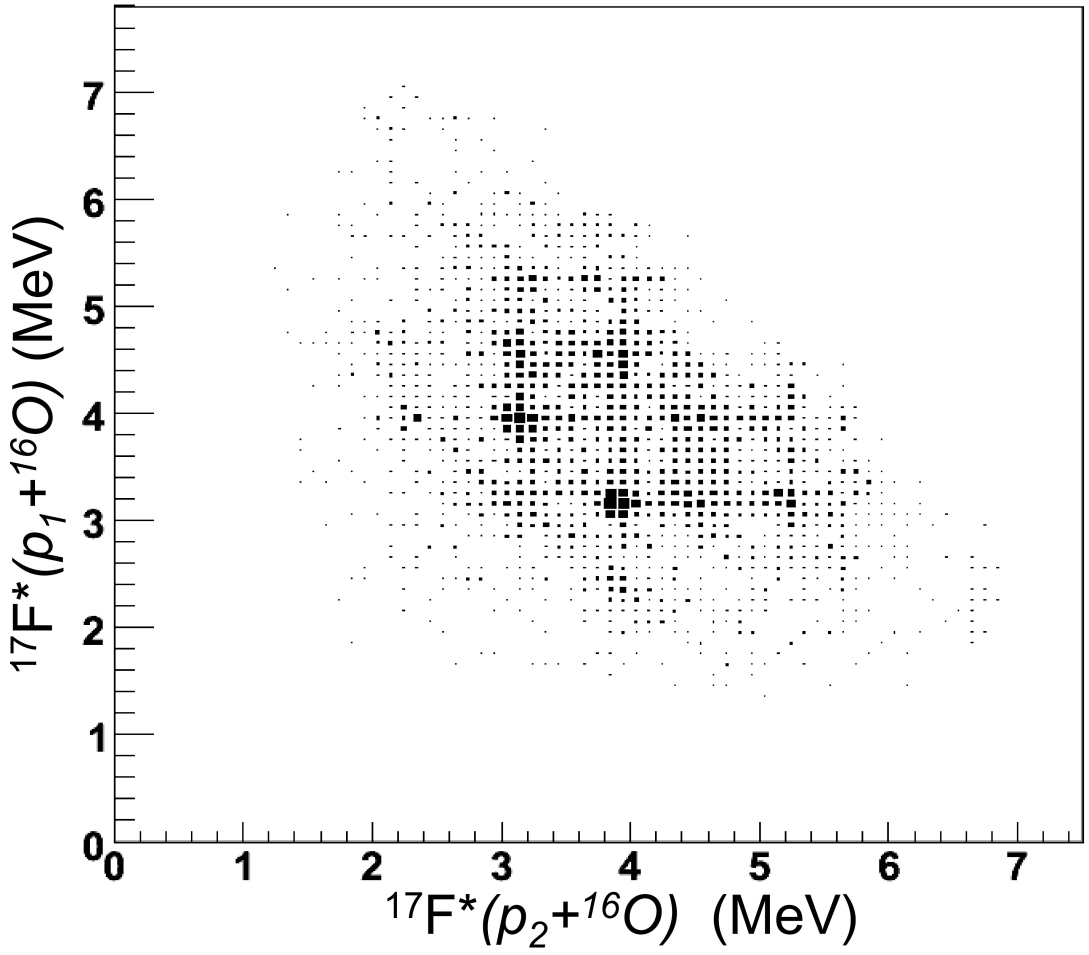

Fig. 34. Modified Dalitz plot with the coordinates shown as the excitation energies in ^{17}F with the assumption of sequential $^{18}\mathrm{Ne}^* \rightarrow p + {}^{17}\mathrm{F}^* \rightarrow p + {}^{16}\mathrm{O} + p$ decay. $E^{(1)}_{^{17}\mathrm{F}^*}$ is the excitation energy of ^{17}F based on the assumption that one proton of the coincident proton pair is from $^{18}\mathrm{Ne}^* \rightarrow p + {}^{17}\mathrm{F}^*$ and the other one is from $^{17}\mathrm{F}^* \rightarrow p + {}^{16}\mathrm{O}$. $E^{(2)}_{^{17}\mathrm{F}^*}$ is the same with the role of the protons reversed.

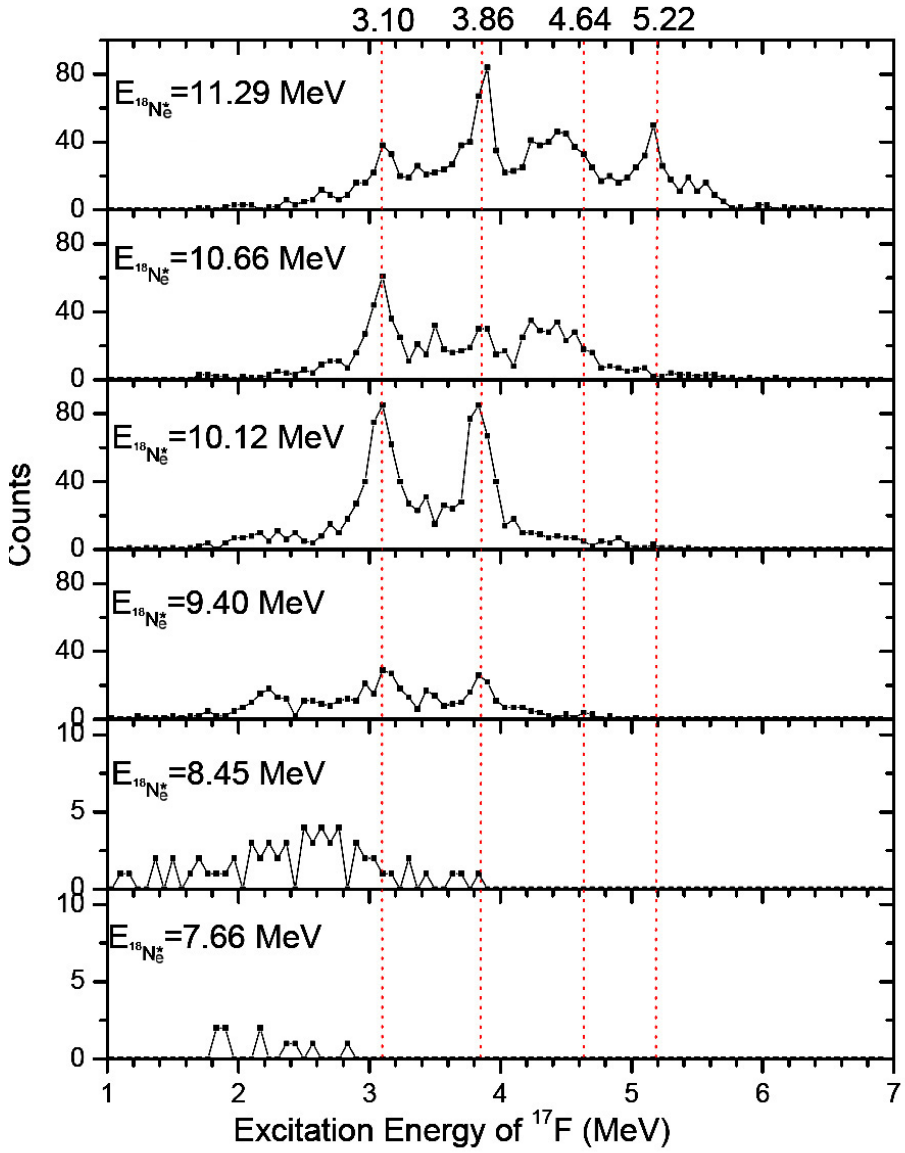

Fig. 35. The energy levels of the ^{17}F* intermediate states in the "sequential" decay process ^{17}F$^* \rightarrow p + {}^{16}$O*. Here the sequence of the two protons was not considered.

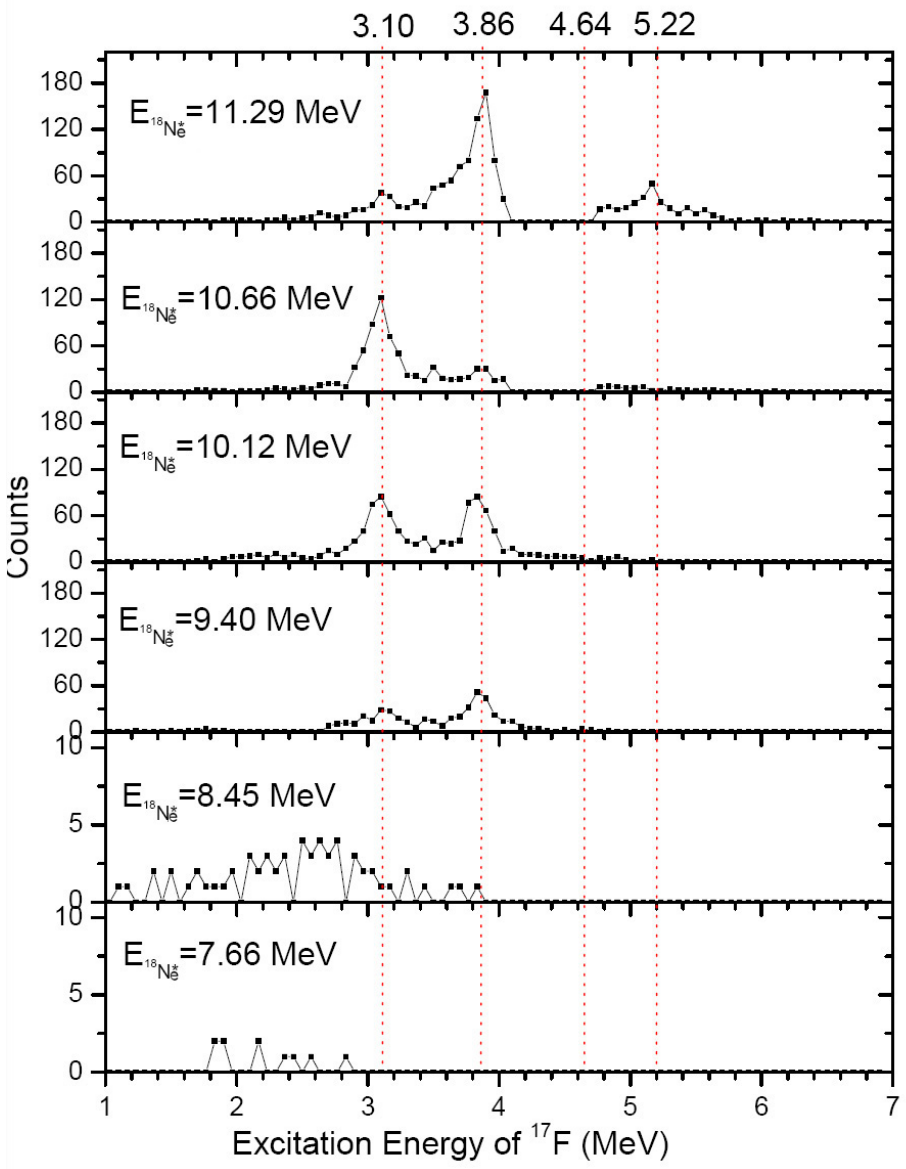

Fig. 36. The energy levels of the ^{17}F* intermediate states in the "sequential" decay process $^{17}\mathrm{F}^* \rightarrow p + {}^{16}\mathrm{O}^*$. The sequence of the two protons was considered as discussed in the text.

should discuss other possible decay models for this state.

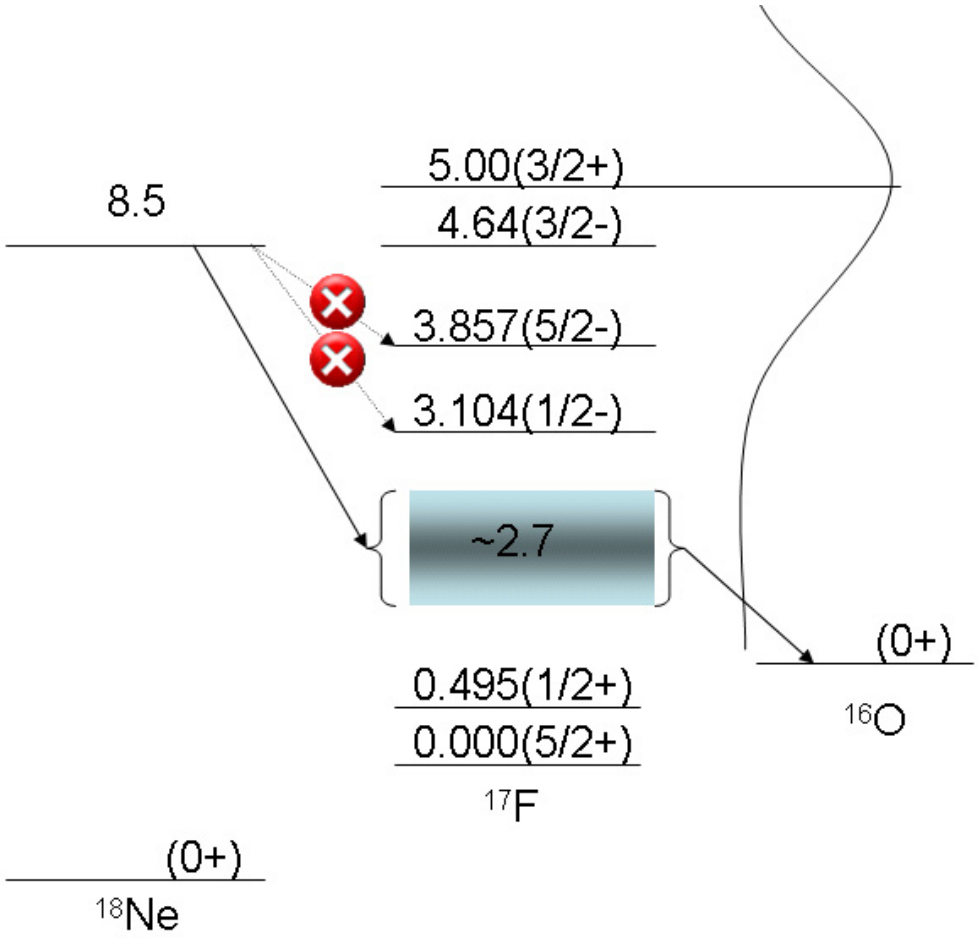

Fig. 37. A possible "decay" scheme for ^{18}Ne*(8.45 MeV). If the decay is sequential, it should have proceeded through the intermediate state of ^{17}F*(2.7 MeV) which does not exist, or this "state" is the tail of the broad resonance state ^{17}F$^{*}(5.0 \pm 0.7\,\mathrm{MeV})$. See the text for details.

1. Sequential decay

Here we consider a possible decay model which is sequential decay through the tail of a broad $d_{3/2}$ state in ^{17}F[1](Fig. 38). The excitation energy of the broad ($FWHM \approx 1.5$

[1]Thanks to Dr. Carl A. Gagliardi for this suggestion

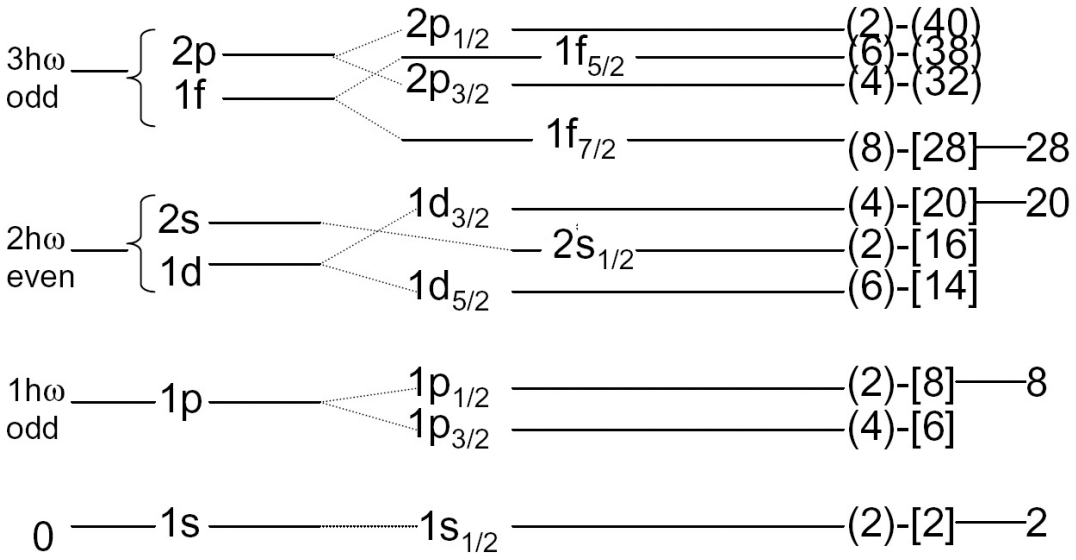

Fig. 38. Approximate level pattern for protons in the shell model.

MeV) $d_{3/2}$ state is 5.0 MeV. The "peak" value that would correspond to sequential decay was measured to be 2.7 MeV (see Fig. 37 as well as Fig. 36). Assuming a sequential mode, the first step is the decay

$$^{18}\mathrm{Ne}^{*}(8.45\,\mathrm{MeV}) \rightarrow {}^{17}\mathrm{F}^{*}_{(d_{3/2})}(E).$$

The second step is the decay

$$^{17}\mathrm{F}^{*}_{(d_{3/2}{}^{+})}(E) \rightarrow p + {}^{16}\mathrm{O}.$$

The $^{17}\mathrm{F}^{*}_{(d_{3/2})}(E)$ indicates that the intermediate state of ^{17}F has a structure $(d_{3/2})$ and has excitation energy E. The possibility of the proton being in this state is $|\psi(E)|^2$, where the ψ is the proton wave function. The possibility of the $2p$ decay through the

$^{17}\mathrm{F}^{*}_{(d_{3/2})}(E)$ state should be

$$W(E) \quad \propto \quad P^{(p)}_{^{18}\mathrm{Ne}^{*}}(E) \times |\psi(E)|^2, \tag{5.2}$$

where $P^{(p)}_{^{18}\mathrm{Ne}^{*}}(E)$ is the penetrability for the proton in the the process $^{18}\mathrm{Ne}^{*}(8.45\,\mathrm{MeV}) \rightarrow {}^{17}\mathrm{F}^{*}_{(d_{3/2})}(E) + p$.

To generate the proton wave function in Eq. 5.2, we used potential parameters from Ref. [42]. The results are given in Table VIII. The calculations with the parameters shown in Table VIII give the correct position of the resonance, but the calculated width appeared to be smaller than the experimental width. We repeated the calculation for the mirror nucleus, ^{17}O, where the parameters for the $d_{3/2}$ level are known with higher precision. For ^{17}O, we obtained a width which is 10% larger than experimentally observed. This result is expected in the extreme single particle approach. We also noticed that there is another $d_{3/2}$ level $^{17}\mathrm{O}(5.08\,\mathrm{MeV}, 3/2+)$. This level is 0.8 MeV higher in excitation energy and has a width of 6.6 keV, which is 10 times smaller than the width of the lower level. These results verified that the calculations are reasonable. The 10% difference can be considered as a conservative evaluation of the width. Using the potential approach, we obtained the contribution of the tail of $^{17}\mathrm{O}(d_{3/2}, 5.0\,\mathrm{MeV})$ to proton decay. The calculated wave function, $P^{(p)}_{^{18}\mathrm{Ne}^{*}}(E)$, and $w(E)$ for $l = 2$ are shown in Fig. 39. If the orbital momentum of the decay of the $^{18}\mathrm{Ne}^{*}(8.45\,\mathrm{MeV})$ level is equal to zero ($l = 1$), the contribution is 0.01, and for $l = 2$, it is 0.0081. The small probability for this decay mode stimulated us to consider other possible decay mechanisms.

2. ^{2}He decay

In Goldansky's original work [12] on two proton decay from a ground state of a nucleus, he speculated that "the energy correlation between the protons during the

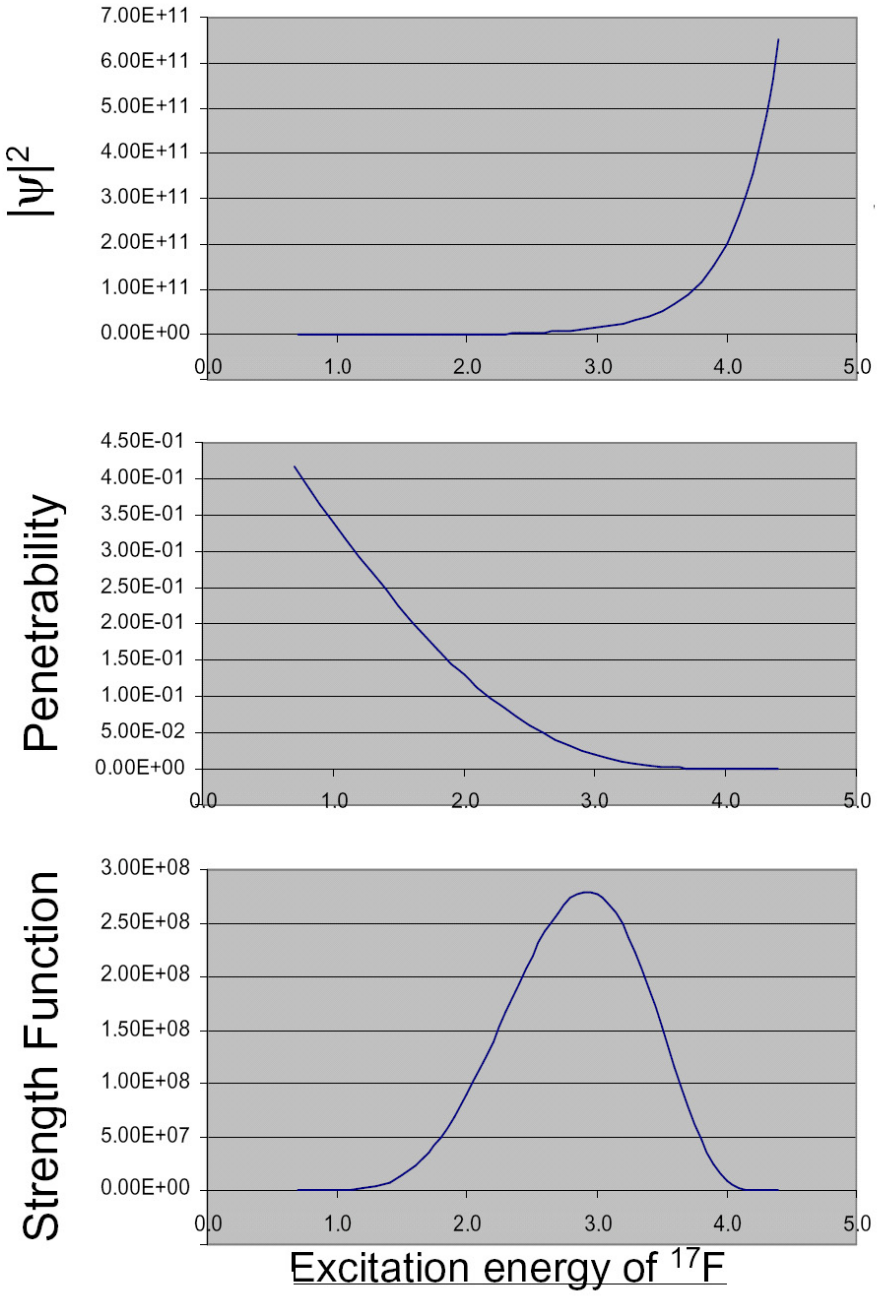

Fig. 39. The strength function of the "sequential" decay of $^{18}\mathrm{Ne}^{*}(8.45\,\mathrm{MeV}) \rightarrow {}^{16}\mathrm{O} + 2p$, where $l = 2$ for the both protons. See the text for details.

Table VIII. Parameters of the Woods-Saxon potential for ^{17}F

Parameters (Ref. [42])	V_0	r_0	a	V_{sl}	r_{sl}	a_{sl}	r_0(Coulomb)
^{17}F	-59.75	1.17	0.64	6.4	1.17	0.64	1.21
^{17}O	-60.065	1.17	0.64	6.4	1.17	0.64	1.21

The results of the calculation

Nucleus	$E_{peak}^{(cal)}$	$FWHM^{(cal)}$	$E_{peak}^{(exp)}$	$FWHM^{(exp)}$
	MeV	MeV	MeV	MeV
^{17}F	5.09	1.35	5.00	1.50
^{17}O	5.08	0.10	5.09	0.09

two-proton decay, which leads to their energies being almost equal". The energy distribution between the two protons should be the fingerprint of the correlation of the protons, independent of a decay from a ground state, or an excited state of a nucleus.

To determine the energy spectrum of two protons we need the decay amplitude of the resonant state of ^{18}Ne $\rightarrow$ ^{16}O$+p+p$. To check the idea that the decay from the 8.45 MeV state of ^{18}Ne* is a ^{2}He decay, we calculated the relative energy spectrum of the two protons. Two models were used, one is based on a single particle state cluster model, and the other one is based on three body Faddeev equations.

a. ^{2}He decay with a Single Particle State Cluster model

Consider a ^{2}He (or di-proton) as a cluster which moves around a ^{16}O core, as shown in Fig. 40. The total energy of the system is E_t, the relative energy between the two protons is E_r, and the relative energy between ^{2}He and ^{16}O is E_R.

In this model, we simplified the process to two steps. First, we consider just the

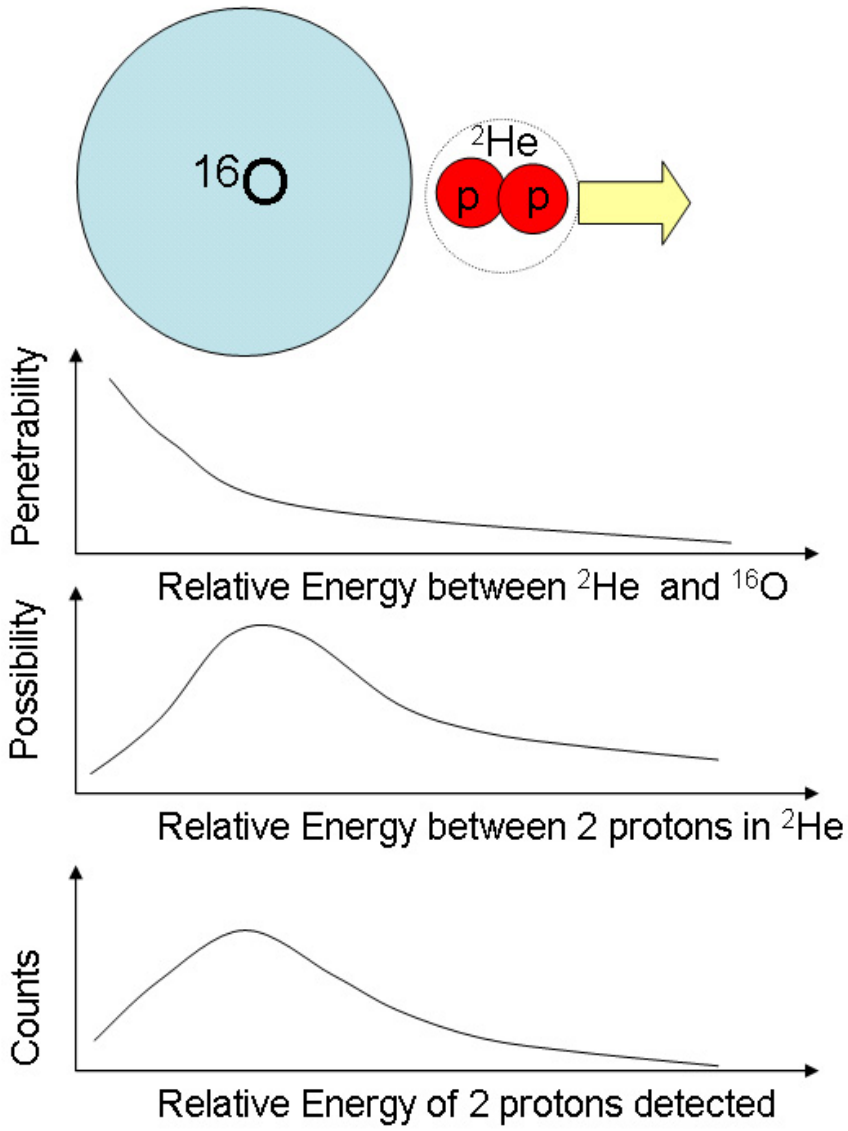

Fig. 40. An illustration of a simple ^{2}He decay model which was used to explain the $^{18}\mathrm{Ne}^*(8.45\,\mathrm{MeV}) \rightarrow 2p + {}^{16}\mathrm{O}$ decay. See the text for details.

interaction of two protons as if they are moving in free space. In the second step we consider only the penetrability of this two-proton cluster escaping from the core. The second step is straight forward. For the first step, the free space proton-proton wave function is needed. In order to make the calculation more reliable, this wave function also should explain neutron-neutron scattering.

To achieve this, we calculated the two-neutron wave function using a central Woods-Saxon potential, with the assumption that the system is slightly unbound. It is known that neutron-neutron scattering has a virtual resonance pole at about -70 keV [57]. However, for two protons, the corresponding virtual resonance pole is about 400 keV due to the Coulomb force. We can determine the wave function of the weakly bound state of two neutrons by adjusting the potential parameters. Keeping these parameters, and only turning on the Coulomb force, we can get the wave function for proton-proton scattering, or effectively the wave function for the two-proton system (di-proton or ^{2}He) in free space. The probability ($P_{p-p}^{(^2\mathrm{He})}$) of the two protons having a relative energy E_r can be obtained from the wave function of the system. In this model, an assumption is made that the wave function of this two proton system is the same as that in $^{16}\mathrm{O} + 2p$. The ^{2}He would escape from the core with energy $E_R = E_t - E_r$. If we define the penetrability of ^{2}He escaping from the core as $P_{2p-core}$, the probability ($P_{p-p}^{(Det)}$) of detecting two protons with relative energy E_r is

$$P_{p-p}^{(Det)}(E_r) = P_{p-p}^{(^2\mathrm{He})}(E_r) \times P_{2p-core}(E_R). \tag{5.3}$$

The result of the calculation with these assumptions is shown in Fig. 41. There is good agreement between the calculations and the experimental result. The Woods-Saxon parameters used here ranged for "V" between -50 and -70 MeV, "a" between 0.3 an 0.7 fm, and "r" between 0.9 and 1.5 fm. The peak in Fig. 41 is very insensitive

to the Woods-Saxon parameters. A parameter set which results in a slightly unbound two-neutron system produces almost the same curve as in Fig. 41.

With an assumption that the decay of the ^{18}Ne* state is democratic (see Chapter I.C), the energy distribution of the decay can be described by [58]

$$\frac{\mathrm{d}N}{\mathrm{d}\epsilon} \propto \sqrt{\epsilon(E_{2p}-\epsilon)}\,|M|^2, \tag{5.4}$$

where ϵ is the relative energy of the protons, E_{2p} is the energy of the resonance relative to the $2p$ threshold, which is 4.07 MeV for ^{18}Ne*(8.45 MeV), and M is an amplitude which depends only weakly on ϵ. Therefore, if the decay corresponding to ^{18}Ne*(8.45 MeV) is democratic, it should produce a broad distribution in energy with a maximum at 2.035 MeV, as shown in Fig. 41.

b. ^{2}He decay with a Faddeev approach

A more sophisticated model using a Faddeev approach was also used to predict the decay spectrum[2]. Generally the amplitude of the three-body decay $a \to 1+2+3$ can be written as the sum of the three Faddeev components:

$$R = R^{12} + R^{13} + R^{23}. \tag{5.5}$$

Here, R is the total decay amplitude, R^{ij} is the Faddeev component which contains the final state interaction between particles i and j of the three-body system $i+j+k$. In the case of ^{2}He-decay, we should observe a peak in the energy spectrum which is the result of the p-p final state interaction—an analog of the Migdal-Watson peak in the case of the neutron-neutron final state interaction. The peak in the p-p relative energy spectrum can appear only in the R^{23} component, where $2 = p$ and $3 = p$. The

[2]Thanks to Dr. Akram Mukhamedzhanov for his help with the calculation

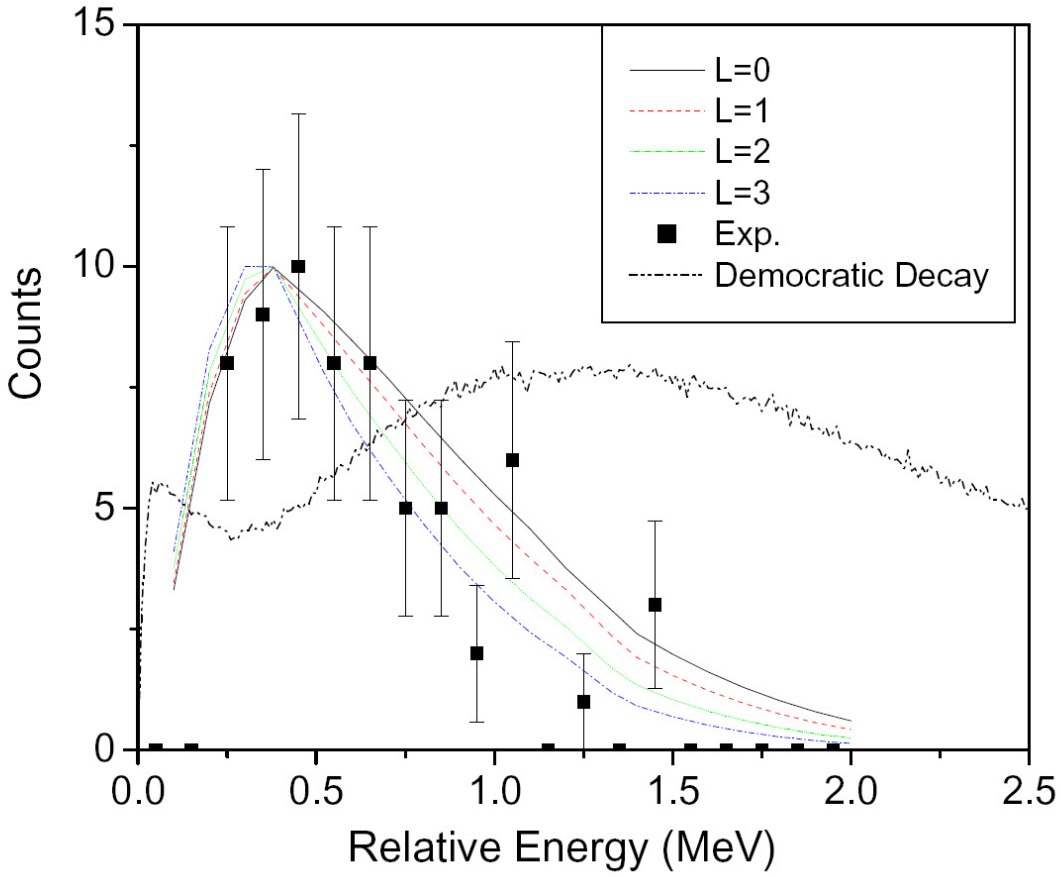

Fig. 41. Spectrum of the relative energy between two coincident protons emitted from the 8.45 MeV excited state of ^{18}Ne with different decay models. The l is the angular momentum of the ^{2}He relative to the ^{16}O core when ^{2}He-decay is assumed. Since the spin and parity of this state are unknown, different l values are calculated and compared to the experimental data.

R^{23} component can be written as

$$\begin{aligned} R^{23} &= (R^{12}+R^{13})G_{23}^{(0)}\, f_{23} \\ &= \int \frac{\mathrm{d}\mathbf{p}}{(2\,\pi)^3}\,(R^{12}+R^{13})\,\frac{1}{\frac{p^2}{2\mu_{23}}-E_{23}-i\,0}f_{23}(\mathbf{p},\mathbf{k}_{23}), \end{aligned} \tag{5.6}$$

where, $G_{23}^{(0)}$ is a free particle Green's function, $f_{23}(\mathbf{p},\mathbf{k}_{23})$ is the half-off-the-energy shell (HOES) p-p scattering amplitude, $\mathbf{p}$ is the virtual relative momentum of two protons, $\mathbf{k}_{23}$ is the on-shell relative momentum, i. e. $E_{23}=k_{23}^2/(2\,\mu_{23})$, E_{23} is the relative p-p kinetic energy, μ_{23} is the reduced mass of two protons. The integration is performed over the virtual momentum $\mathbf{p}$. The amplitude $f_{23}(\mathbf{p},\mathbf{k}_{23})$ is given by the sum of the HOES Coulomb scattering amplitude and the HOES Coulomb-modified nuclear p-p scattering amplitude. It is obtained as shown below.

The scattering matrix can be defined as

$$S_l \equiv e^{2i\delta_l}, \tag{5.7}$$

$$= e^{2i(\delta_l-\delta_l^C+\delta_l^C)}, \tag{5.8}$$

$$\equiv e^{2i(\delta_l^{CN}+\delta_l^C)}, \tag{5.9}$$

where δ_l^C is the Coulomb phase shift, and δ_l^{CN} is called the Coulomb modified nuclear phase shift. The amplitude of the scattering wave is

$$f_l = \frac{e^{2i\delta_l}-1}{2ik}, \tag{5.10}$$

$$= \frac{e^{2i\delta_l^{CN}}e^{2i\delta_l^C}-1}{2ik}, \tag{5.11}$$

$$= \frac{(e^{2i\delta_l^{CN}}-1+1)e^{2i\delta_l^C}-1}{2ik}, \tag{5.12}$$

$$= \frac{(e^{2i\delta_l^{CN}}-1)e^{2i\delta_l^C}}{2ik}+\frac{e^{2i\delta_l^C}-1}{2ik}, \tag{5.13}$$

$$\equiv f_l^{CN}e^{2i\delta_l^C}+f_l^C. \tag{5.14}$$

In momentum space, this can be written as

$$f(\vec{p'},\vec{p}) = \sum_l (2l+1)\, f_l\, P_l(\cos\theta), \tag{5.15}$$

$$= \sum_l (2l+1)\left[f_l^{CN} e^{2i\delta_l^C} + f_l^C\right] P_l(\cos\theta), \tag{5.16}$$

where P_l represent Legendre polynomials.

For low energy nucleon-nucleon scattering, the cross section is

$$\delta_l^{CN} \propto (kr)^{2l+1}. \tag{5.17}$$

For $k << 1$, only s-wave ($l = 0$) scattering makes a significant contribution. At low relative energies of two protons it is sufficient to take into account only the s-wave Coulomb modified nuclear scattering amplitude. Therefore, for low energy,

$$\begin{aligned} f(\vec{p'},\vec{p}) &\approx f_0^{CN} e^{2i\delta_0^C} + \sum_l (2l+1)\, f_l^C\, P_l(\cos\theta) \\ &= \left(f_0^{CN} e^{2i\delta_0^C} + \sum_{l=2n} (2l+1)\, f_l^C\, P_l(\cos\theta)\right) + \sum_{l=2n+1} (2l+1)\, f_l^C\, P_l(\cos\theta) \\ &\equiv f^{even} + f^{odd}. \end{aligned} \tag{5.18}$$

The Coulomb amplitude may be written as [59]

$$f^C(p,p',\frac{p^2}{2\mu}) = -2\mu\alpha e^{-\pi\eta/2}\Gamma(1+i\eta)\frac{[p'^2-(p+i\gamma)^2]^{i\eta}}{[(p-p')^2+\gamma^2]^{1+i\eta}}, \tag{5.19}$$

where $\eta = \frac{\alpha\mu}{p}$, and $\gamma \to +0$.

The theoretical description of the nonrelativistic few-body problem is considerably simplified by the use of nonlocal separable potentials in place of local potentials [59, 60]. Consider a simple separable potential

$$V(r',r) = \lambda g(r') g(r), \tag{5.20}$$

where λ is called form factor of the potential. In momentum space, the potential $V(p', p)$ is

$$V(p', p) = \lambda g(p')g(p), \tag{5.21}$$

$$g(p) \equiv \int_0^\infty \mathrm{d}r\, r^2 j_0(p, r)\, g(r). \tag{5.22}$$

For the Yamaguchi separable potential, $g(p)$ takes form

$$g(p) = \frac{1}{p^2 + \beta^2}. \tag{5.23}$$

Then $g(r)$ has the form

$$g(r) = \frac{e^{-\beta r}}{r}. \tag{5.24}$$

The function f_{23} was calculated using the separable potential shown above. The partial-wave expansion of $f_{23}(\mathbf{p}, \mathbf{k}_{23})$ is separated into even and odd partial waves. Since the wave function of two protons is antisymmetric relative to their exchange, only odd partial waves contribute for the total spin $S = 1$ of two protons, while for $S = 0$ only even partial waves contribute. The p-p energy spectrum is calculated using

$$W(E_{23}) = \frac{1}{4}\left|R^{23}_{even}(E_{23})\right|^2 + \frac{3}{4}\left|R^{23}_{odd}(E_{23})\right|^2, \tag{5.25}$$

where R^{23}_{even} is the radial amplitude for the resonance decay into the $1+2+3$ channel corresponding to $S = 0$ and is given by Eq. (5.6), where only even p-p partial wave scattering amplitudes are taken into account. Hence, the s-wave amplitude contains the Coulomb modified nuclear p-p scattering amplitude. R^{23}_{odd} corresponds to $S = 1$, and is given by the integral (5.6) where only odd partial waves of the scattering amplitude are taken into account. These partial wave scattering amplitudes are given only by the HOES Coulomb partial scattering amplitudes [59]. The factors 1/4 and 3/4 are spin weight factors. Since we don't know the explicit form of R^{12} and R^{13},

we replaced them by the Coulomb-centrifugal barrier penetration factor

$$P_l = \frac{q_1\, r_0}{F_l^2(q_1, r_0) + G_l^2(q_1, r_0)}, \tag{5.26}$$

where $F_l(q_1, r_0)$ and $G_l(q_1, r_0)$ are regular and singular Coulomb solutions, $q_1 = \sqrt{2\, M_1\, E_1}$ and E_1 is the relative momentum and relative kinetic energy of nucleus "1" and M_1 is the reduced mass of nucleus "1", and r_0 is the channel radius. The energy of the resonance which decays into the continuum $1 + 2 + 3$ is $E_R = 4$ MeV, and

$$E_1 = E_R - \frac{k_{23}^2}{2\, \mu_{23}}.$$

Since the momentum of the resonance is not known we are not able to determine the relative orbital momentum of nucleus 1 and the center of mass of the two protons. Therefore, to check the dependence of the proton-proton energy spectrum we did calculations from $l = 0$ to 3. The advantage of the separable representation for the Coulomb modified nuclear p-p amplitude is that this amplitude explicitly contains the pole in the energy plane E_{23} corresponding to the virtual p-p state (^{2}He). Hence we can compare the p-p energy spectrum calculated using Eq. (5.25) with the one obtained by taking into account only the p-p Coulomb modified scattering amplitude. The results of the calculations are compared with the experimental data and presented in Fig. 42. As can be seen, the results depend on l such that the larger l is, the stronger the suppression of the higher-energy tail. The full calculation does not differ significantly from the simplified calculations based only on the Coulomb modified p-p scattering amplitude which is dominated by the virtual p-p pole. The relative energy of the two protons with the sequential decay model is shown in Fig. 43. One can see that the calculation does not match the experimental data at large relative energy.

A detailed analysis of the correlation would benefit from data on the angular

correlation between the protons, quantum characteristics of the level, and data with better counting statistics. It is worth noting that the calculated pole is not a "fit" to the data from "this" work. All the parameters used here are from other low energy nucleon-nucleon scattering experiments.

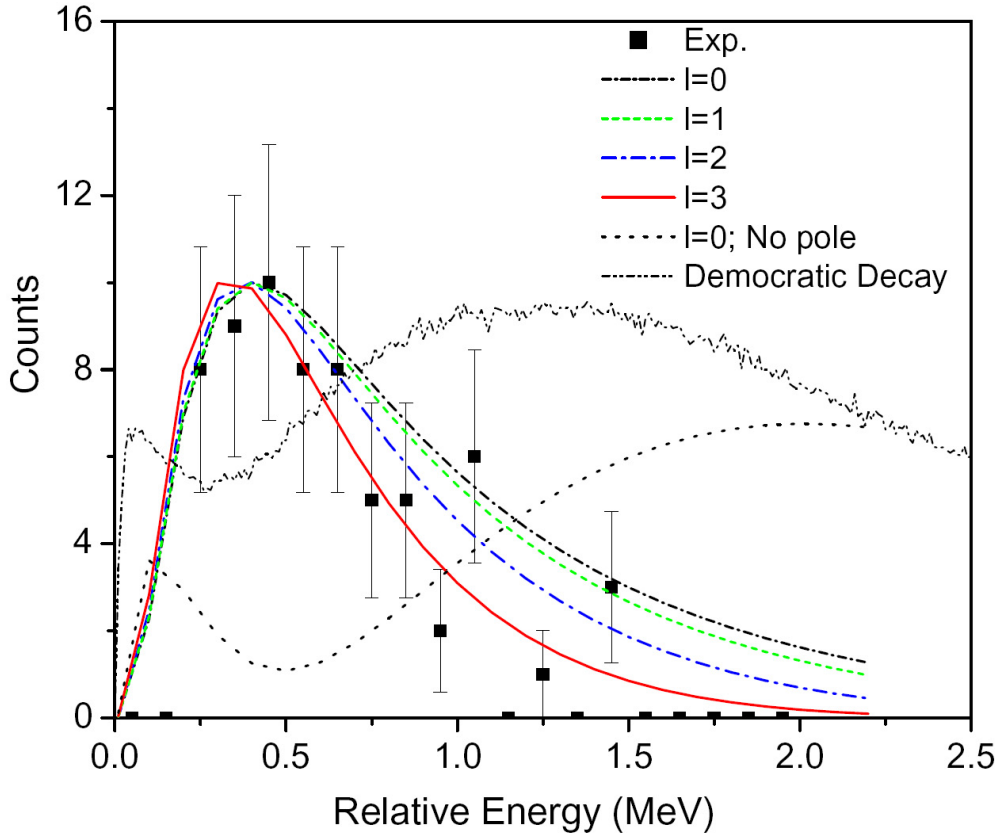

Fig. 42. The spectrum of relative energy between two coincident protons emitted from the 8.45 MeV excited state of ^{18}Ne with calculations based on the Faddeev equation. The l is the angular momentum of ^{2}He relative to the ^{16}O core. Since the spin and parity of this state are unknown, different l values were calculated to compare with the experiment. The dotted line is the calculation in which the resonance pole between the two nucleons is removed.

As a comparison, the relative energy spectra of protons from different sources are shown in Fig. 44. The spectrum of coincident protons emitted from the 8.45

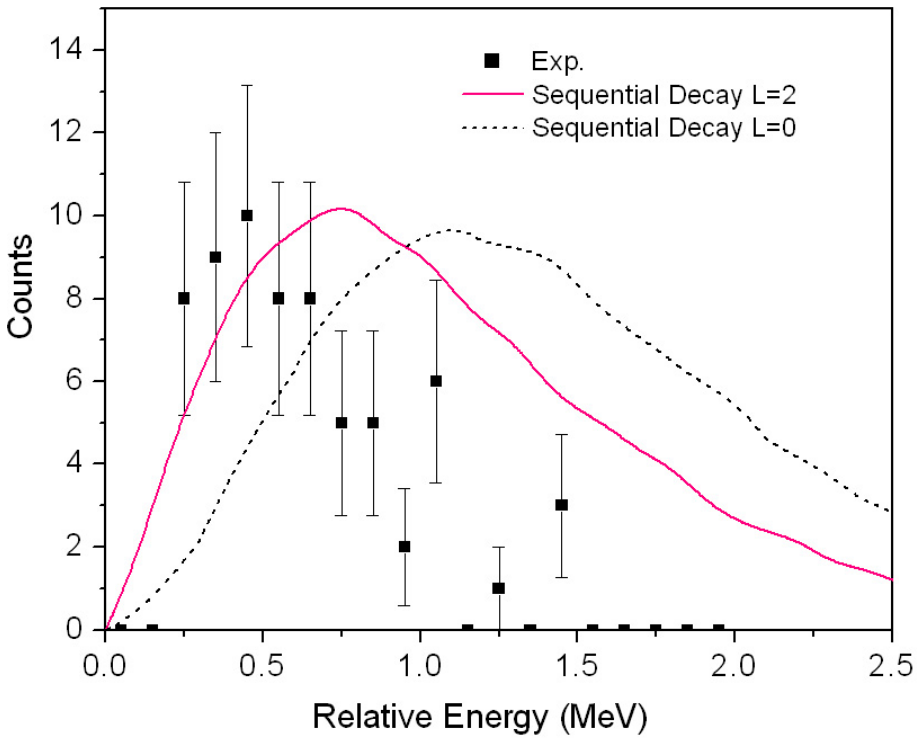

Fig. 43. The $2p$ relative energy spectrum. The curves are simulations with the assumption that the $^{18}\mathrm{Ne}^{*}(8.45\,\mathrm{MeV}) \rightarrow {}^{16}\mathrm{O} + 2p$ is a sequential decay. Since no absolute normalization exists, the calculations were normalized to experimental data.

MeV excited state of ^{18}Ne (red curve at the bottom) has a peak at 0.45 MeV. The spectrum (black curve at the top), which is the relative energy of all the coincident proton pairs measured in this experiment, has a peak at 0.65 MeV. The red curve may be due to ^{2}He decay from the 8.45 MeV state, while the black curve is mainly from sequential decays of excited states of ^{18}Ne, as was shown above.

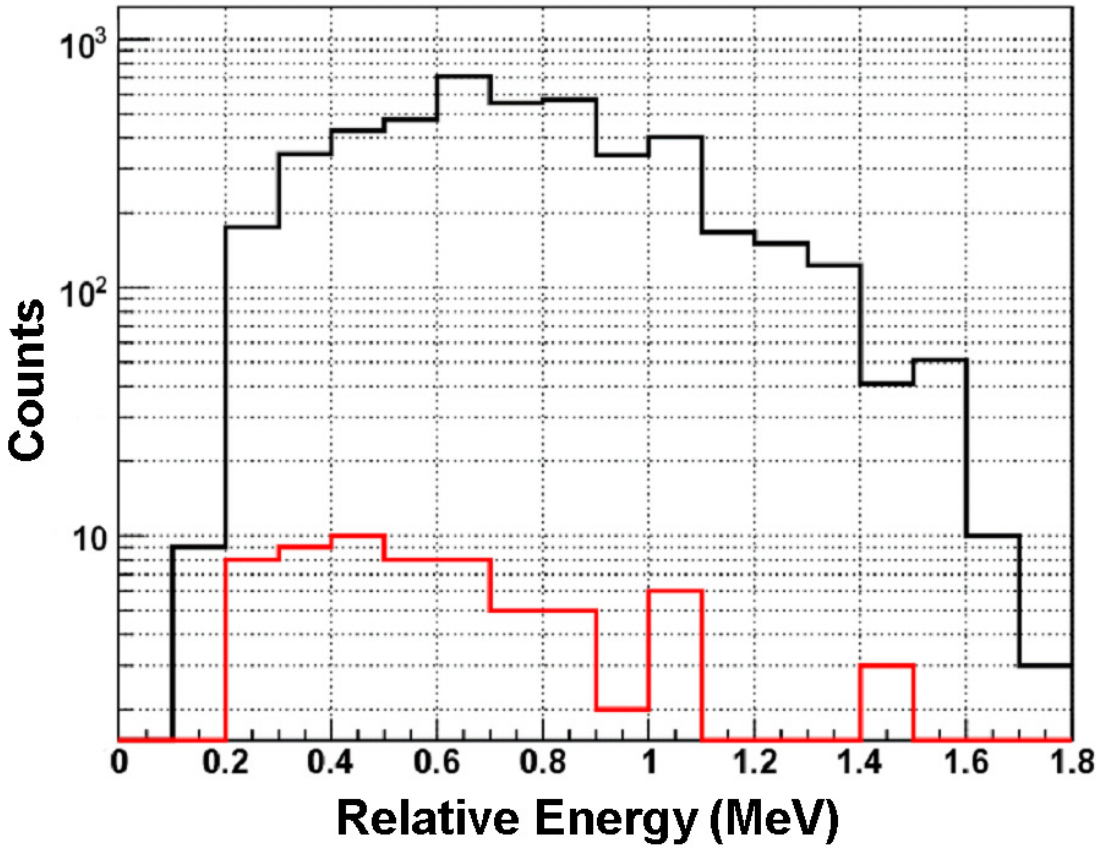

Fig. 44. The comparison of relative energies of the protons from different sources. The red curve is the spectrum of relative energy between two coincident protons emitted from the 8.45 MeV excited state of ^{18}Ne, and the black curve is the spectrum of the relative energy of all the coincident proton pairs measured in this experiment. The red curve may be due to the ^{2}He decay from the 8.45 MeV state of ^{18}Ne, while the black curve is mainly from sequential decays of excited states of ^{18}Ne.

CHAPTER VI

SINGLE PROTON EMISSION FROM THE $^{14}O + \alpha$ REACTION

A. Possible sources of low energy protons

The expected cross section of the $^{14}O(\alpha, p)^{17}F$ reaction at energies below the Coulomb barrier is so small ($\approx 1\,\mu b/sr$ at an energy of 2 MeV [27]) that careful consideration of possible backgrounds should be made.

1. Low energy protons from $^{17}F^* \rightarrow p +^{16}$ O reaction

One possible source of low energy protons could be $^{17}F^* \rightarrow p +^{16}$ O. Let us consider a hypothetical proton decay of a higher excited state in ^{18}Ne to a higher excited state in $^{17}F^*$(see Fig. 45), so that the Q value for the (α, p) reaction will be approximately the same as in the case for the decay from the 7.06 MeV level to the ^{17}F ground state (it could be, for example, the 10.2 MeV level in ^{18}Ne and 3.1 MeV level in $^{17}F^*$). Taking into account the similar kinematics, the energy of the proton will be approximately the same in both cases. However, the energy of the $\alpha +^{14}$ O system will be above the Coulomb barrier for a higher energy resonance in ^{18}Ne, and hence the ratio, Γ_α/Γ_p, could be close to 1.

Many (at present unknown) states in ^{18}Ne up to an excitation energy of 14 MeV, which corresponds to 42 MeV of ^{14}O initial energy in Ref. [31], could contribute background to the low proton energy region. The other source of backgrounds with $\Gamma_\alpha/\Gamma_p \approx 1$ could be secondary proton decay of low lying states in ^{17}F. For example, the proton decay of the 3.1 MeV level can contaminate a broad energy region of protons from zero up to 8 MeV. The energy and the shape of the spectra depend upon the energy and the direction of the primary proton (from the decay of ^{18}Ne).

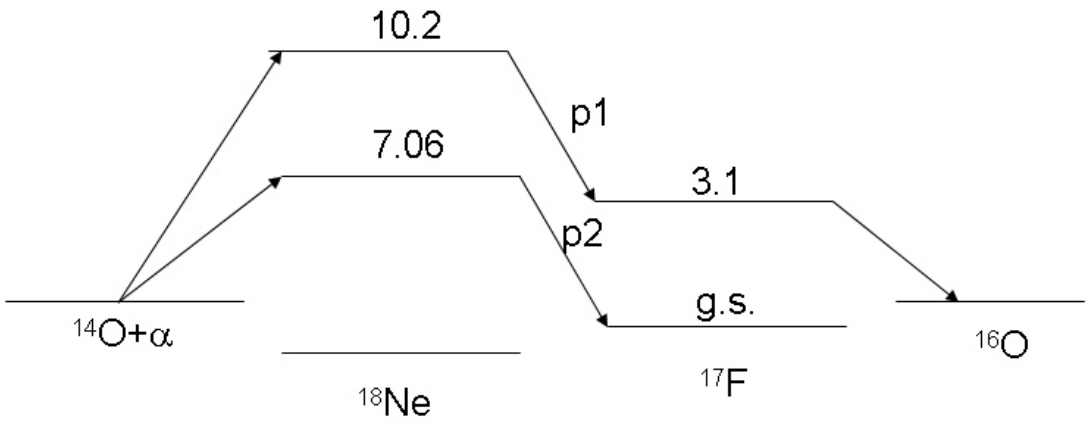

Fig. 45. Possible background in a one proton emission measurement for astrophysics. For example, the energy of a proton from $^{18}\mathrm{Ne}^{*}(10.2\,\mathrm{MeV}) \rightarrow {}^{17}\mathrm{F}(3.1\,\mathrm{MeV})$ is the same (or very close) as the energy of a proton from $^{18}\mathrm{Ne}^{*}(7.06\,\mathrm{MeV}) \rightarrow {}^{17}\mathrm{F}(g.s.)$ since they have the same(or very close) reaction Q-values; for the same reason, protons from $^{17}\mathrm{F}^{*}(3.1\,\mathrm{MeV}) \rightarrow {}^{16}\mathrm{O}(g.s.)$ could be a background.

2. Low energy protons from the $^{7}\mathrm{Be}(\alpha,p)^{10}\mathrm{B}$ reaction

Another possible source of low energy protons is $^{7}\mathrm{Be}(\alpha,p)^{10}\mathrm{B}$. High intensity ($\approx 10^{6}\,pps$) $^{14}\mathrm{O}$ beams are produced by means of the online magnetic separation with a velocity filter like MARS [32] or CRIB [61]. They provide for up to 99% purity of the $^{14}\mathrm{O}$ beam. The important contamination is $^{7}\mathrm{Be}$, which has the same Z/A ratio as $^{14}\mathrm{O}$, and therefore can not be separated by a velocity filter.

At this energy range, if the $^{14}\mathrm{O}(\alpha,p)^{17}\mathrm{F}$ reaction is below the Coulomb barrier, the cross section is small, while the $^{7}\mathrm{Be}(\alpha,p)^{10}\mathrm{B}$ reaction at the same c.m. energy is above the Coulomb barrier and the cross section is much larger.

In fact, due to the Coulomb barrier effect, the cross section of the reaction $^{7}\mathrm{Be}(\alpha,p)^{10}\mathrm{B}$ [62] at low energies is 10^{3} times larger than for the $^{14}\mathrm{O}(\alpha,p)^{17}\mathrm{F}$ reaction.

In the experiment carried out at TAMU, the ratio of ^{7}Be/^{14}O was suppressed up to 10^{-4} of the ^{14}O intensity.

3. Protons from reactions of ^{14}O on the foils

In the experiment, there were other proton emission sources including elastic scattering and inelastic scattering. There were foils in the ^{14}O beam path, including BC-400 scintillators (main component C_9H_{10}), and the Havar entrance window ($Co_{42}Cr_{20}Ni_{13}Fe_{19}W$). Protons from BC-400 foils might be elastically scattered. Also the nuclei in the foils could have proton emission reactions with the ^{14}O beam. All the protons created by ^{14}O on the BC-400 and Havar foils had shorter flight time for the same reasons as discussed above. Therefore they could be separated from the protons of interest.

B. Results and discussion of the ^{14}O(α, p) reaction

With the SPORTTIK approach (Ch. IV), the excitation function for the ^{14}O(α, p) reaction was obtained. Since the $2p$ coincident events are free from background, they were used to test the TOF and energy calibration. Figure 46 shows a plot of TOF versus particle energy for detectors at zero degrees. The black dots indicate the spectrum for single protons. The blue solid circles are all the $2p$-coincident events, and the events corresponding to intermediate states at 3.1 and 4.6 MeV in ^{17}F are shown by red and green markers. As can be seen in Fig. 46, the levels corresponding to different Q-values are not clearly separated due to the time/energy resolution of the system and the energy spread of the beam. Still the majority of the events corresponding to the 4.6 MeV level are below the ones corresponding to the 3.1 MeV level which has shorter TOF than the previous one.

These data, together with the α particle spectrum, were used to test a simulation code (the lines in Fig. 46), and to predict the loci for the $^{14}O(\alpha, p)^{17}F$ reaction populating the ground state of ^{17}F. The parameters of the simulation code were adjusted using the zero degrees coincidence data and the elastic α-particles events. As can be seen in the figure, the lines for α elastic scattering and protons corresponding to $^{17}F(g.s.)$ cross at low energy range. This is a result of the large energy loss of the α-particles in the gas.

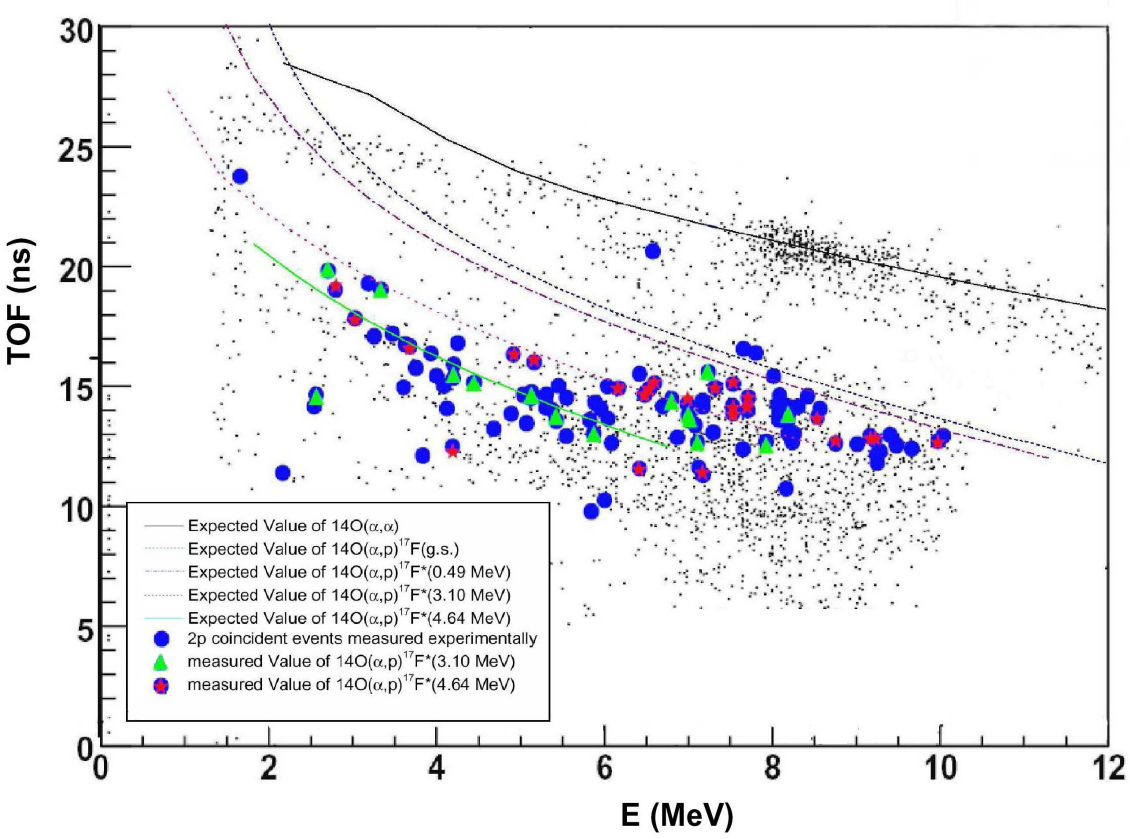

Fig. 46. the TOF-E spectrum for the ^{14}O + ^{4}He interaction. The overlap markers, which are labeled in the figure are from the two proton coincident events measured by the silicon array. The excitation energy of the intermediate states of the two proton coincident events from the sequential decay are given.

A part of the TOF-E spectrum is shown in Fig. 47. The intense group at the

top (slow moving particles) corresponds to α particles from the $^{14}\mathrm{O} + \alpha$ interaction. Below these are the proton events corresponding to the population of the different states in $^{17}\mathrm{F}$. The events corresponding to the population of the ground and the first excited state in $^{17}\mathrm{F}$ are shown by the shadow.

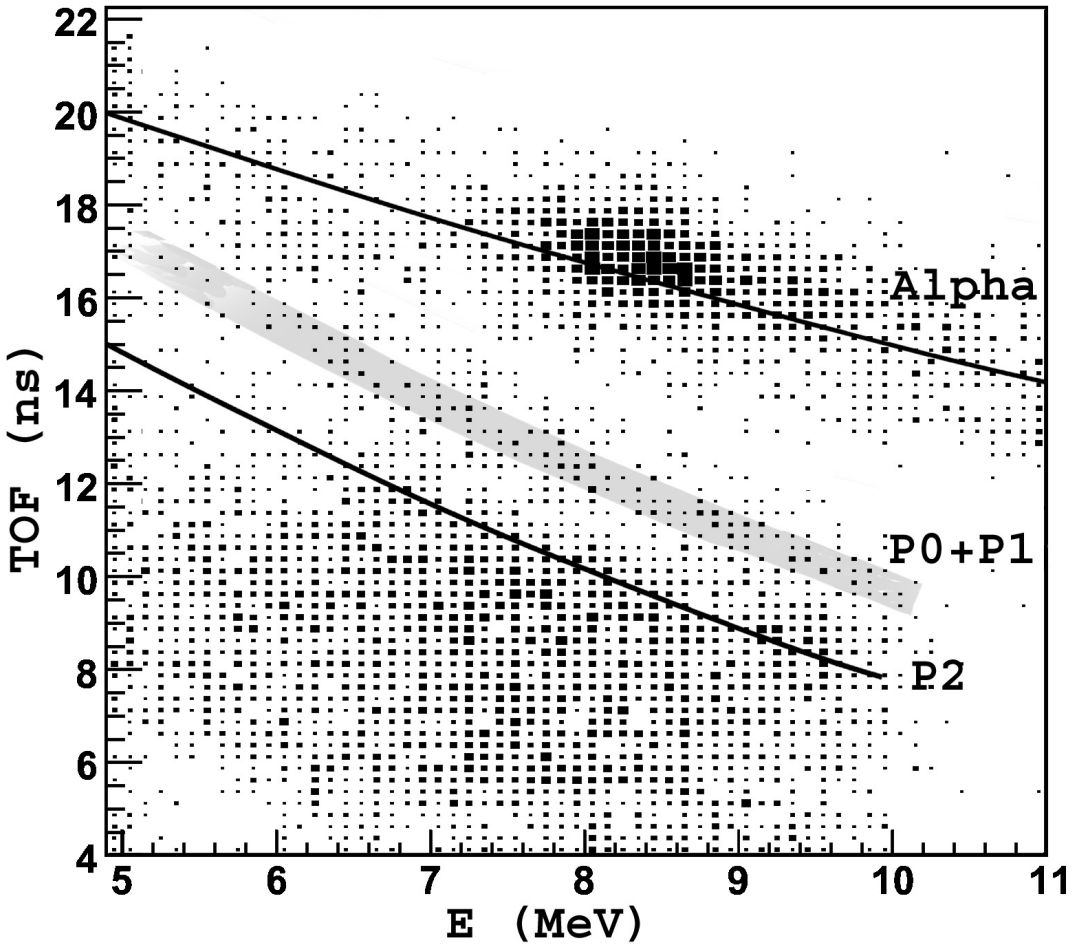

Fig. 47. the TOF-E spectrum of the $^{14}\mathrm{O} + {}^{4}\mathrm{He}$ interaction.

Figure 48 shows the proton spectrum in the c.m. system corresponding to the population of the ground and first excited states in $^{17}\mathrm{F}$ in the $^{14}\mathrm{O}(\alpha, p)$ reaction. The low energy cut off is due to the loss of the proton-alpha identification at low energies. Unfortunately, our results are restricted to rather high energies of the interaction

because of the high pressure of the helium gas which was used to stop ^{14}O at a short distance before the QSD. This limitation can be improved in future measurements by decreasing the pressure of the helium gas target. One can see in Fig. 48 that the cross section related with the population of the two lowest particle stable states in ^{17}F rapidly decreases when the interaction energy approaches the astrophysically important region. At lower excitation energies the total proton yield at small angles is dominated by proton decays from particle unstable states in ^{17}F due to preferable kinematics.

Figure 49 is the "excitation function" if only the conventional TTIK method was used as was presented in Ref. [31] and subsequent publications. It shows the projection on the energy axis of all proton events, including events corresponding to the population of the ground and possible excited state of ^{17}F.

As can be seen in Figs. 48 and 49, the number of protons corresponding to excitation of the particle stable states in ^{17}F is less than 10% of the total proton events at zero degrees in this experimental condition. Therefore, it is questionable if the total proton spectra which were presented in Ref. [31] could be used to extract information useful for astrophysics.

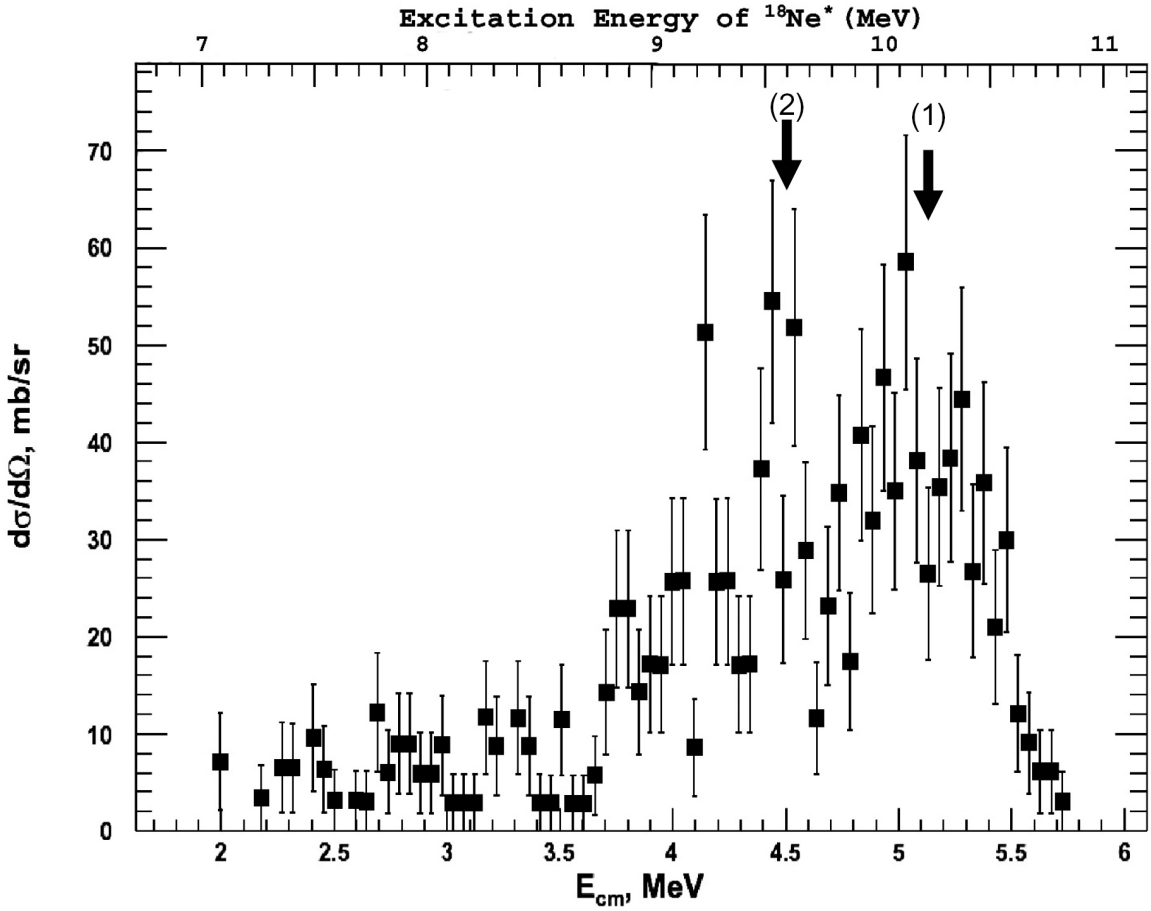

Fig. 48. Excitation function for the $^{14}\mathrm{O}(\alpha, p)^{17}\mathrm{F}$ reaction, where ^{17}F is in g.s. or the first excited state 0.5 MeV. The peak (1) is from the decay $^{18}\mathrm{Ne}^*(10.2\,\mathrm{MeV}) \rightarrow p + {}^{17}\mathrm{F}(g.s.)$; the peak (2) may be from the decay $^{18}\mathrm{Ne}^*(10.2\,\mathrm{MeV}) \rightarrow p + {}^{17}\mathrm{F}^*(0.5\,\mathrm{MeV})$.

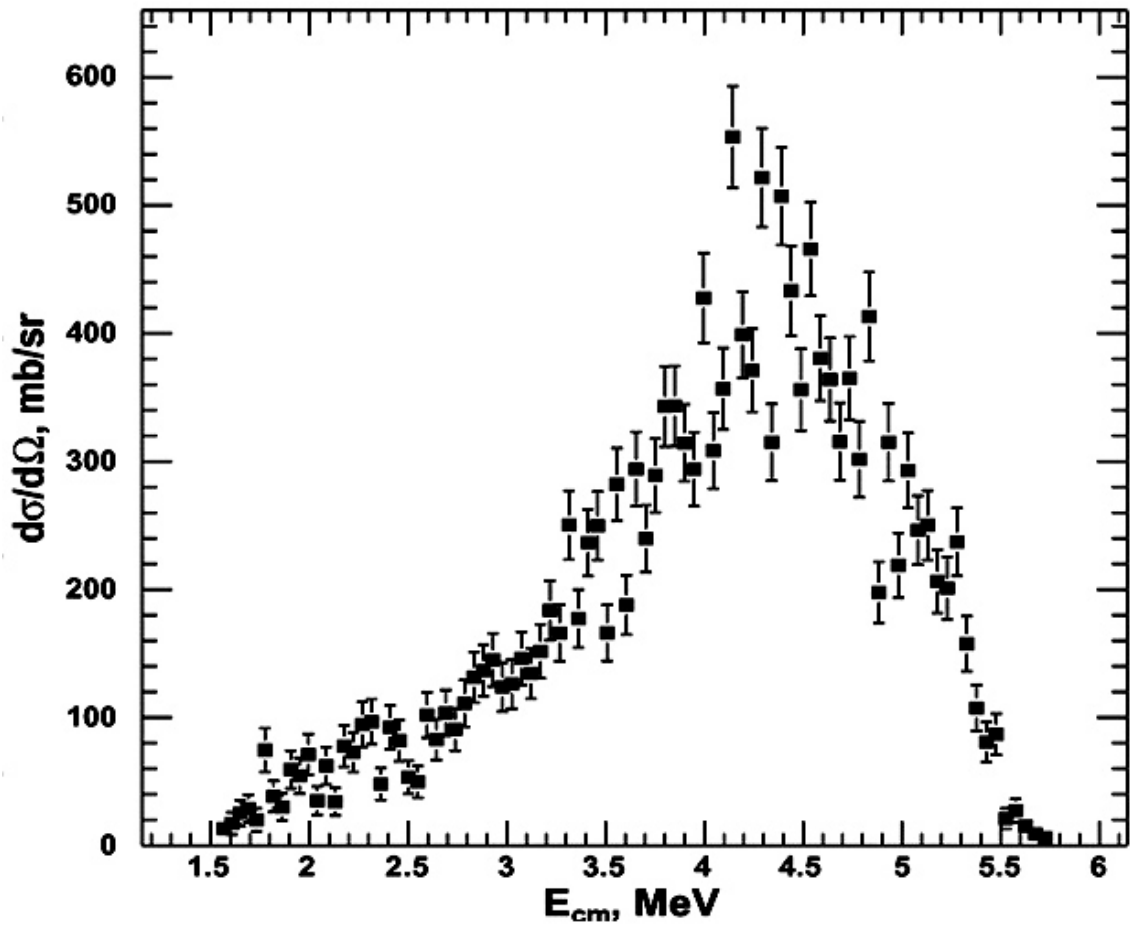

Fig. 49. "Excitation function" for the $^{14}\mathrm{O}(\alpha, p)^{17}\mathrm{F}$ reaction if only the conventional TTIK method was used as is in Ref. [31]. There is a huge background mixture that gets counted by this procedure.

CHAPTER VII

SUMMARY

Using facilities at the Texas A&M University Cyclotron Institute, we obtained a radioactive ion beam of ^{14}O. The key factor in developing the beam was the use of resonances in the ^{14}N(p, n) reaction. As a result we obtained ^{14}O beams in the energy range 2-7 MeV/u with an intensity of over 10^5 pps, and with less than 1% contamination in the beam. These parameters were obtained with a relatively low intensity primary ^{14}N beam (less than 0.6 $e\mu A$). They combine to make the ^{14}O beam at TAMU one of the best available.

The nature of the physics goals in this project required a better suppression of the contamination of ^{7}Be, which has the same q/A ratio as the ^{14}O RIB. A ^{7}Be/^{14}O intensity ratio of about 10^{-4} was achieved by an amplitude analysis of light signals from ions passing through thin scintillating foils. The amplitude resolution of the system developed for this experiment was about 30%. The light signals also provided an event by event count of ^{14}O incident on the helium gas target and start signals for the Time-Of-Flight (TOF) measurements.

We made the first measurements of α particles, protons and two proton events in the $^{14}\mathrm{O} + \alpha$ resonance interaction using the TTIK method with helium gas as a target. TOF combined with energy information was used to separate protons and α particles, the main products from the $^{14}\mathrm{O} + \alpha$ interactions. This approach was found to be very effective and provided the possibility to study products with low energy.

The two proton study showed that this process, less than 7 MeV in the c.m., is mainly due to resonance excitation of levels in ^{18}Ne (several of them appeared to be previously unreported). The decay of the ^{18}Ne levels mainly proceeds by successive two proton decay through intermediate particle unstable states in ^{17}F. This finding

casts doubt on the interpretation of proton spectra from earlier measurements in Ref. [31] in terms of astrophysically important results. We found that proton decay of the 8.45 MeV level in ^{18}Ne differs from the decay of all other states. We interpreted this decay as being due to a correlated proton pair decay. We used formalism of the three body Faddeev equation, and a simple model of the final state interaction to describe the properties of this decay. We found that the main features of the distribution of relative energy between the two protons are primarily defined by the p-p interaction. The influence of the third body is mainly to create a barrier for the decay.

We modified the TTIK method by adding the determination of the location of the reaction in the target. Using the modified TTIK method we were able to measure a spectrum of protons corresponding to the population of ^{17}F particle stable states in the $^{14}\mathrm{O}(\alpha, p)$ reaction. The continuation of this spectrum to lower energies is an important astrophysical issue.

The excitation functions for elastic $\alpha + {}^{14}$O scattering were measured at several initial energies of ^{14}O by the TTIK method. We also made measurements of the excitation functions for the elastic $\alpha + {}^{14}$C scattering (together with a FSU group). The two excitation functions, $^{14}\mathrm{C}(\alpha, \alpha)$ and $^{14}\mathrm{O}(\alpha, \alpha)$, appeared surprisingly different. We found several very strong resonances and determined tentative assignments for their quantum characteristics. From these data, α-cluster structures were found in the $^{18}\mathrm{Ne}^*$ and $^{18}\mathrm{O}^*$.

APPENDIX A

THE DIFFERENTIAL CROSS SECTION OF A THREE BODY REACTION WITH THE TTIK APPROACH

As in (α, α), and (α, p) reactions using the TTIK approach, careful consideration must be used to extract a differential cross section for $(\alpha, 2p)$. We will extend the formulae for 2-body reactions to 3-body reactions in this section.

Consider a reaction $a + A \rightarrow b_1 + b_2 + B$ (Fig. 50). In the lab system, the number of reaction products with energy in the range $(E_L, E_L + \mathrm{d}E_L)$ going into the solid angle $\mathrm{d}\Omega$ can be written as

$$\mathrm{d}N^{(L)} = IN_t\sigma^{(L)}\mathrm{d}\Omega_1^{(L)}\mathrm{d}\Omega_2^{(L)}\mathrm{d}E_1^{(L)}\mathrm{d}E_2^{(L)}, \tag{A.1}$$

where I is the number of projectile particles, N_t is the number of target nuclei, and $\sigma^{(L)}$ is the double differential cross section. $\mathrm{d}E_1^{(L)}$ ($\mathrm{d}E_1^{(L)}$) is energy of particle b_1 (b_2) in lab system, and $\mathrm{d}\Omega_1^{(L)}$ ($\mathrm{d}\Omega_1^{(L)}$) is solid angle of particle b_1 (b_2) in lab system.

Similarly, in the center of mass system,

$$\mathrm{d}N^{(C)} = IN_t\sigma^{(C)}\mathrm{d}\Omega_1^{(C)}\mathrm{d}\Omega_2^{(C)}\mathrm{d}E_1^{(C)}\mathrm{d}E_2^{(C)}. \tag{A.2}$$

where the symbols used here are self-explanatory.

Since $\mathrm{d}N_C = \mathrm{d}N_L \equiv \mathrm{d}N$,

$$\sigma^{(L)}\mathrm{d}\Omega_1^{(L)}\mathrm{d}\Omega_2^{(L)}\mathrm{d}E_1^{(L)}\mathrm{d}E_2^{(L)} = \sigma^{(C)}\mathrm{d}\Omega_1^{(C)}\mathrm{d}\Omega_2^{(C)}\mathrm{d}E_1^{(C)}\mathrm{d}E_2^{(C)}. \tag{A.3}$$

Then we have:

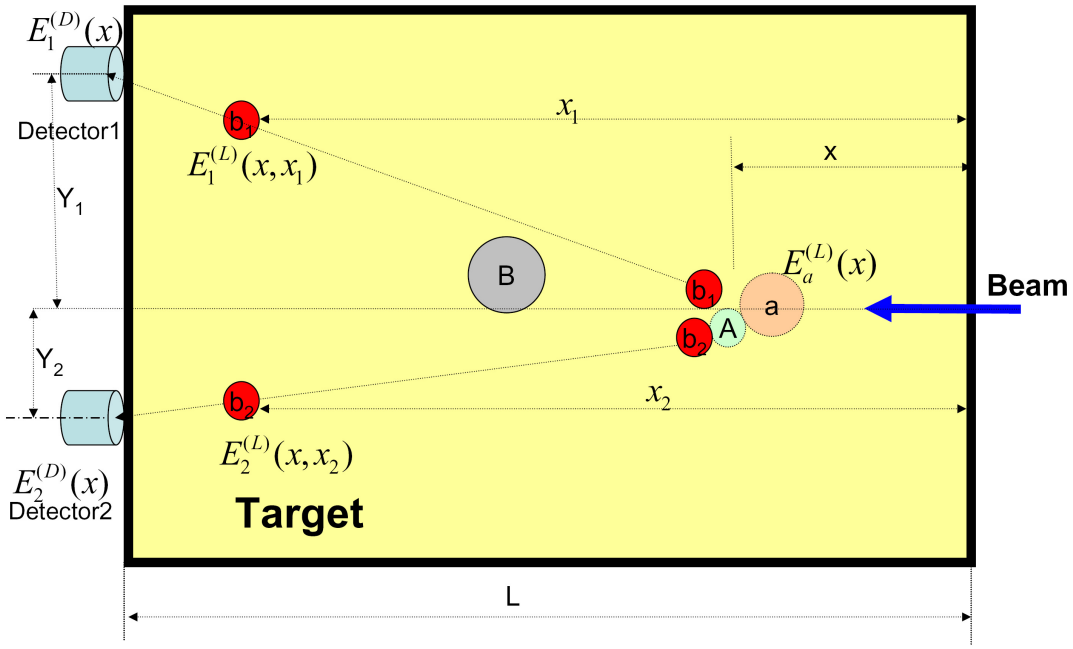

Fig. 50. A layout to detect reaction products in $a + A \rightarrow b + B$.

$$\begin{aligned}\sigma^{(C)} &= \sigma^{(L)} \frac{\mathrm{d}\Omega_1^{(L)}}{\mathrm{d}\Omega_1^{(C)}} \frac{\mathrm{d}\Omega_2^{(L)}}{\mathrm{d}\Omega_2^{(C)}} \frac{\mathrm{d}E_1^{(L)}}{\mathrm{d}E_1^{(C)}} \frac{\mathrm{d}E_2^{(L)}}{\mathrm{d}E_2^{(C)}} \\ &= \frac{\mathrm{d}N}{IN_t \mathrm{d}\Omega_1^{(L)} \mathrm{d}E_1^{(L)} \mathrm{d}\Omega_2^{(L)} \mathrm{d}E_2^{(L)}} \frac{\mathrm{d}\Omega_1^{(L)}}{\mathrm{d}\Omega_1^{(C)}} \frac{\mathrm{d}\Omega_2^{(L)}}{\mathrm{d}\Omega_2^{(C)}} \frac{\mathrm{d}E_1^{(L)}}{\mathrm{d}E_1^{(C)}} \frac{\mathrm{d}E_2^{(L)}}{\mathrm{d}E_2^{(C)}}. \end{aligned} \tag{A.4}$$

Since

$$\frac{\mathrm{d}\Omega^{(L)}}{\mathrm{d}\Omega^{(C)}} = \frac{\sqrt{1-\gamma^2 \sin^2\theta^{(L)}}}{\left(\gamma\cos\theta^{(L)} + \sqrt{1-\gamma^2\sin^2\theta^{(L)}}\right)^2}, \tag{A.5}$$

where $\gamma = v_{cm}/v_b^{(C)}$, v_{cm} is the speed of center of mass, and $v_b^{(C)}$ the speed of outgoing particle in c.m. system, therefore, we have

$$\sigma^{(C)} = \frac{\sqrt{1-\gamma_1^2 \sin^2\theta_1^{(L)}}}{\left(\gamma_1\cos\theta_1^{(L)} + \sqrt{1-\gamma_1^2\sin^2\theta_1^{(L)}}\right)^2} \frac{\sqrt{1-\gamma_2^2 \sin^2\theta_2^{(L)}}}{\left(\gamma_2\cos\theta_2^{(L)} + \sqrt{1-\gamma_2^2\sin^2\theta_2^{(L)}}\right)^2}$$

$$\times \frac{\mathrm{d}N}{IN_t \mathrm{d}\Omega_1^{(L)} \mathrm{d}E_1^{(L)} \mathrm{d}\Omega_2^{(L)} \mathrm{d}E_2^{(L)}} \frac{\mathrm{d}E_1^{(L)}}{\mathrm{d}E_1^{(C)}} \frac{\mathrm{d}E_2^{(L)}}{\mathrm{d}E_2^{(C)}}. \tag{A.6}$$

For a thick target, the number of target nuclei N_t equates to

$$N_t = \rho \mathrm{d}x, \tag{A.7}$$

where ρ is the density of the target, $\mathrm{d}x$ is the thickness of the target and the energy of projectile is in the range $(E_L, E_L + \mathrm{d}E_L)$. Then

$$\begin{aligned} \sigma^{(C)} &= \frac{\sqrt{1-\gamma_1^2 \sin^2\theta_1^{(L)}}}{\left(\gamma_1 \cos\theta_1^{(L)} + \sqrt{1-\gamma_1^2\sin^2\theta_1^{(L)}}\right)^2} \frac{\sqrt{1-\gamma_2^2 \sin^2\theta_2^{(L)}}}{\left(\gamma_2 \cos\theta_2^{(L)} + \sqrt{1-\gamma_2^2\sin^2\theta_2^{(L)}}\right)^2} \\ &\times \frac{\mathrm{d}N}{I\rho \mathrm{d}x \mathrm{d}\Omega_1^{(L)} \mathrm{d}E_1^{(L)} \mathrm{d}\Omega_2^{(L)} \mathrm{d}E_2^{(L)}} \frac{\mathrm{d}E_1^{(L)}}{\mathrm{d}E_1^{(C)}} \frac{\mathrm{d}E_2^{(L)}}{\mathrm{d}E_2^{(C)}}. \end{aligned} \tag{A.8}$$

In fact,

$$E_a^{(L)}(x) = E_a^{(L)}(0) - \int_0^x \frac{\mathrm{d}E_a^{(L)}(x)}{\mathrm{d}x} \mathrm{d}x, \tag{A.9}$$

$$E_a^{(C)}(x) = \frac{m_A}{m_a + m_A} E_a^{(L)}(x). \tag{A.10}$$

The detected energy of the particle is

$$\begin{aligned} E_1^{(D)}(x) &\equiv E_1^{(L)}(L, x) \\ &= E_1^{(L)}(x, x) - \int_0^{\sqrt{(L-x)^2+Y_1^2}} \frac{\mathrm{d}E_1^{(L)}(x_1, x)}{\mathrm{d}x_1} \mathrm{d}x_1. \end{aligned} \tag{A.11}$$

By numerical calculation, one can obtain $\left(\frac{\Delta E_1^{(D)}}{\Delta E_1^{(C)}}\right)_{E_2^{(D)}}$. Therefore, the cross section of the three body reaction in the TTIK approach can be written as

$$\sigma^{(C)} \approx \frac{\sqrt{1-\gamma_1^2 \sin^2\theta_1^{(L)}}}{\left(\gamma_1 \cos\theta_1^{(L)} + \sqrt{1-\gamma_1^2\sin^2\theta_1^{(L)}}\right)^2} \frac{\sqrt{1-\gamma_2^2 \sin^2\theta_2^{(L)}}}{\left(\gamma_2 \cos\theta_2^{(L)} + \sqrt{1-\gamma_2^2\sin^2\theta_2^{(L)}}\right)^2}$$

$$\times \frac{\mathrm{d}N\Delta x}{I\rho \mathrm{d}\Omega_1^{(L)}\mathrm{d}\Omega_2^{(L)}(\Delta E_1^{(D)})^2(\Delta E_2^{(D)})^2}$$
$$\times \left(\frac{\Delta E_1^{(D)}}{\Delta E_1^{(C)}}\right)_{E_2^{(D)}} \left(\frac{\Delta E_2^{(D)}}{\Delta E_2^{(C)}}\right)_{E_1^{(D)}} \left(\frac{\Delta E_1^{(D)}}{\Delta x}\right)_{E_2^{(D)}} \left(\frac{\Delta E_2^{(D)}}{\Delta x}\right)_{E_1^{(D)}}. \quad \text{(A.12)}$$

For zero degrees in lab system, the equation may be simplified to

$$\begin{aligned} \sigma_c &= \frac{\mathrm{d}N}{IN_t}\left[\frac{4\pi}{\mathrm{d}\Omega_L}\frac{\left(\gamma\cos\theta_L + \sqrt{1-\gamma^2\sin^2\theta_L}\right)^2}{\sqrt{1-\gamma^2\sin^2\theta_L}}\right]_{\theta_L=0}^2 \\ &\approx \frac{(4\pi)^2(1+\gamma)^4\mathrm{d}N}{IN_t(\mathrm{d}\Omega_L)^2}. \end{aligned} \quad \text{(A.13)}$$

APPENDIX B

THE FLORIDA STATE UNIVERSITY EXPERIMENT

As described in Chapter (I), data from the $^{14}C(\alpha,\alpha)$ reaction is extremely useful to make reliable spin-parity assignments in the $^{14}O + \alpha$ reaction, since it yields much higher counting statistics due to the availability of a ^{14}C beam as an accelerated beam. This data was obtained at Florida State University (FSU)[1].

A schematic of the experimental layout used at FSU is shown in Fig. 51. A 35 MeV ^{14}C beam was produced using ^{14}C in the ion source for the Tandem-Linac facility at FSU. The beam was directed through the first scattering chamber at high vacuum. In the vacuum was a Au foil of thickness $30\,\mu g/cm^2$ which was backed by $30\,\mu g/cm^2$ of natural carbon. Two silicon detectors were placed at a laboratory angle of 20° on each side of the beam axis to observe scattered beam particles. This enabled us to monitor and then control the position and intensity of the beam in the first scattering chamber.

The second scattering chamber was filled with 70 kPa of helium gas and served as a thick target. A 2.41 μm Havar foil separated the two chambers. Six silicon detectors, with collimators of 8 mm diameter, were mounted over the angular range from 0° to 35°. The detectors in both chambers were calibrated by using a ^{228}Th α source.

For testing and calibration purposes, a ^{12}C beam was used. Since the $^{12}C(\alpha,\alpha)^{12}C$ reaction has been extensively studied and the compound nucleus spectrum for ^{16}O is very well known, the setup and the data treatment procedure could be checked. In

[1]Thanks to Dr. Grigory V. Rogachev and the research group at FSU for their support with the experiment which was carried out there.

fact, the R-matrix technique and the geometry of the setup could be calibrated in this way.

To test the conditions, a ΔE-E telescope was used at 0° in the first runs. The results showed that an overwhelming majority of the events in the detector corresponded to α-particles. Therefore, the ΔE detector was be removed.

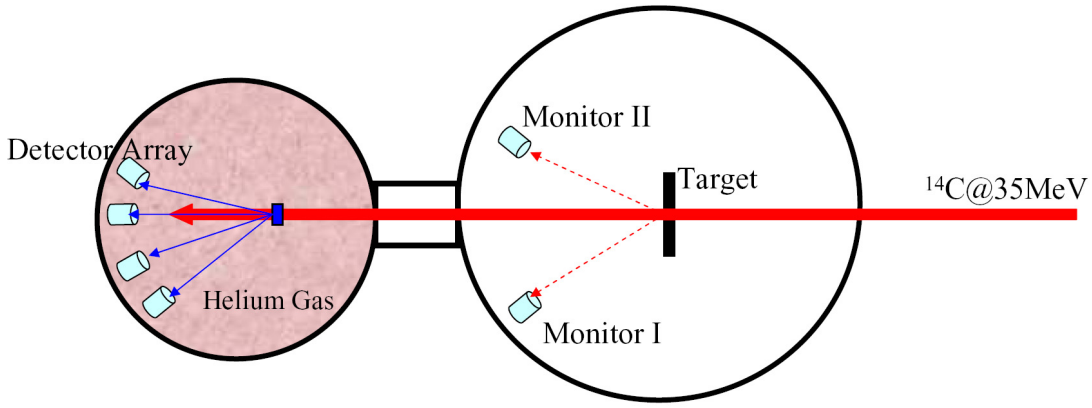

Fig. 51. A schematic of the experimental layout at Florida State University.

The electronics for the experiment are illustrated in Fig. 52. The signal from a detector was passed through a pre-amplifier into a spectroscopic amplifier. The signals then were sent to ADCs. Another output from the pre-amplifier was sent to a CFD and was used as a gate for the ADCs. The software, MSU SpecTcl [63] was used for readout of the data.

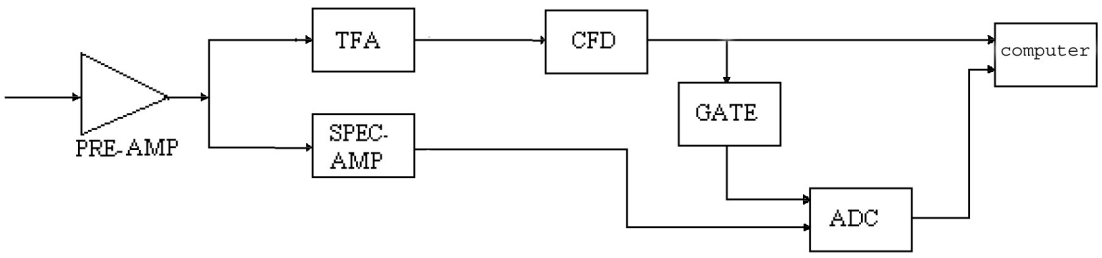

Fig. 52. The data acquisition system used in the experiment at Florida State University.

REFERENCES

[1] H. Feshbash, *Theoretical nuclear physics: Nuclear structure* (John Wiley & Sons, Inc., New York, 1992).

[2] K. P. Artemov, M. S. Golovkov, V. Z. Goldberg, V. I. Dukhanov, I. Mazurov, V. V. Pankratov, V. Paramonov, V. Rudakov, I. Serikov, V. Solovev, and V. Timofeev, Sov. J. Nucl. Phys. **52**, 480 (1990).

[3] V. Z. Goldberg, G. G. Chubarian, G. Tabacaru, L. Trache, R. E. Tribble, A. Aprahamian, G. V. Rogachev, B. B. Skorodumov, and X. D. Tang, Physical Review C (Nuclear Physics) **69**, 031302 (2004).

[4] P. A. Butler and W. Nazarewicz, Rev. Mod. Phys. **68**, 349 (1996).

[5] V. V.Z.Goldberg, V.P.Rudakov, Sov.J.Nucl.Phys. **19**, 253 (1974).

[6] A. H. Wuosmaa, R. R. Betts, M. Freer, and B. R. Fulton, Annu. Rev. Nucl. Part. Sci. **45**, 89 (1995).

[7] V. Z. Goldberg, G. V. Rogachev, and W. H. Trzaska, Phys. Rev. C **69**, 024602 (2004).

[8] M. Dufour and P. Descouvemont, Nucl. Phys. A **738**, 447 (2004).

[9] W. V. Oertzen, Z. Phys. A **357**, 355 (1997).

[10] V. Z. . Goldberg, W. H. Trzaska, and G. V. Rogachev, in *Proceedings of the Symposium on Nuclear Clusters* (Debrecen, Hungary, 2003), pp. 89–96.

[11] A. Aprahamian, K. Langanke, and M. Wiescher, Prog. Part. Nucl. Phys. **54**, 535 (2005).

[12] V. I. Goldansky, Nucl. Phys. **19**, 482 (1960).

[13] A. I. Baz, V. I. Goldanskii, V. Z. Goldberg, and J. B. Zeldovich, *Light and Intermediate Nuclei Close to the Drip Line* (Nauka, Moscow, 1972).

[14] D. F. Geesaman, R. L. McGrath, P. M. S. Lesser, P. P. Urone, and B. VerWest, Phys. Rev. C **15**, 1835 (1977).

[15] L. V. Grigorenko, R. C. Johnson, I. G. Mukha, I. J. Thompson, and M. V. Zhukov, Phys. Rev. Lett. **85**, 22 (2000).

[16] L. V. Grigorenko, R. C. Johnson, I. G. Mukha, I. J. Thompson, and M. V. Zhukov, Phys. Rev. C **64**, 054002 (2001).

[17] R. A. Kryger, A. Azhari, M. Hellström, J. H. Kelley, T. Kubo, R. Pfaff, E. Ramakrishnan, B. M. Sherrill, M. Thoennessen, S. Yokoyama, R. J. Charity, J. Dempsey, A. Kirov, N. Robertson, D. G. Sarantites, L. G. Sobotka, and J. A. Winger, Phys. Rev. Lett. **74**, 860 (1995).

[18] I. Mukha, E. Roeckl, L. Batist, A. Blazhev, J. Doring, H. Grawe, L. Grigorenko, M. Huyse, Z. Janas, R. Kirchner, M. L. Commara, C. Mazzocchi, S. L. Tabor, and P. V. Duppen, Nature **439**, 298 (2006).

[19] M. D. Cable, J. Honkanen, R. F. Parry, S. H. Zhou, Z. Y. Zhou, and J. Cerny, Phys. Rev. Lett. **50**, 404 (1983).

[20] J. Honkanen, M. D. Cable, R. F. Panrry, S. H. Zhou, Z. Y. Zhou, and J. Cerny, Phys. Lett. B **133**, 146 (1983).

[21] M. Pfutzner, E. Badura, C. Bingham, B. Blank, M. Chartier, H. Geissel, J. Giovinazzo, L. Grigorenko, R. Grzywacz, M. Hellstrom, Z. Janas, J. Kurcewicz,

A. Lalleman, C. Mazzocchi, I. Mukha, G. Munzenberg, C. Plettner, E. Roeckl, K. Rykaczewski, K. Schmidt, R. Simon, M. Stanoiu, and J.-C. Thomas, Eur. Phys. J. A. **14**, 279 (2002).

[22] B. Blank, A. Bey, G. Canchel, C. Dossat, A. Fleury, J. Giovinazzo, I. Matea, N. Adimi, F. D. Oliveira, I. Stefan, G. Georgiev, S. Grevy, J. C. Thomas, C. Borcea, D. Cortina, M. Caamano, M. Stanoiu, F. Aksouh, B. A. Brown, F. C. Barker, and W. A. Richter, Phys. Rev. Lett. **94**, 232501 (2005).

[23] A. Galindo-Uribarri, J. G. Campo, and J. R. Beene, Nucl. Phys. A **682**, 363c (2001).

[24] L. V. Grigorenko, R. C. Johnson, I. J. Thompson, and M. V. Zhukov, Phys. Rev. C **65**, 044612 (2002).

[25] M. Pfiitzner, Eur. Phys. J. A. **25**, 165 (2005).

[26] B. Harss, J. P. Greene, D. Henderson, R. V. F. Janssens, C. L. Jiang, J. Nolen, R. C. Pardo, K. E. Rehm, and J. P. Schiffer, Phys. Rev. Lett. **82**, 3964 (1999).

[27] B. Harss, C. L. Jiang, K. E. Rehm, J. P. Schiffer, J. Caggiano, P. Collon, J. P. Greene, Henderson, and P. Parker, Phys. Rev. C **65**, 035803 (2002).

[28] J. C. Blackmon, D. W. Bardayan, W. Bradfield-Smith, A. E. Champagne, A. A. Chen, T. Davinson, K. I. Hahn, R. L. Kozub, Z. Ma, P. D. Parker, G.Rajbaidya, R.C.Runkle, C.M.Rowland, A.C.Shotter, M.S.Smith, K.B.Swartz, D.W.Visser, and P.J.Woods, Nucl. Phys. A **688**, 142c (2002).

[29] K. I. Hahn, A. Garcia, E. G. Adelberger, P. V. Magnus, A. D. Bacher, N. Bateman, and G. P. Berg, Phys. Rev. C **54**, 1999 (1996).

[30] Y. Parpottas, S. M. Grimes, S. Al-Quraishi, C. R. Brune, T. N. Massey, J. E. O'Donnell, J. E. Oldendick, A.Salas, and R.T.Wheeler, Phys. Rev. C **72**, 025802 (2005).

[31] M. Notani, S. Kubono, T. Teranishi, Y. Yanagisawa, S. Michimasa, K. Ue, J. He, H. Iwasaki, H. Baba, M. Tamaki, T. Minemura, S. Shimoura, N. Hokoiwa, Y. Wakabayashi, T. Sasaki, T. Fukuchi, A. Odahara, Y. Gono, Z. Fulop, E. Lee, K. Hahn, J. Moon, C. Yun, J. Lee, C. Lee, and S. Kato, Nucl. Phys. A **746**, 113c (2004).

[32] R. E. Tribble, R. H. Burch, and C. A. Gagliardi, Nucl. Instr. and Meth. A **285**, 441 (1989).

[33] Z. Kovacs, B.Scholten, and F. Tarkanyi, Radiochim. Acta **91**, 185 (2003).

[34] M. L. Muga, D. J. Burnsed, W. E. Steeger, and H. E. Taylor, Nucl. Instr. and Meth. **83**, 135 (1970).

[35] M. L. Muga, Nucl. Instr. and Meth. **95**, 349 (1971).

[36] M. L. Muga and G. Griffith, Nucl. Instr. and Meth. **109**, 289 (1973).

[37] Y. Zhao, W. Zhan, and Z. Guo, Nucl. Instr. and Meth. A **355**, 464 (1995).

[38] R. Brun, F. Rademakers, P. Canal, I. Antcheva, and D. Buskulic, ROOT: Users Guide 5.12, 2006, at http://root.cern.ch [viewed on Mar. 1, 2007].

[39] PAW, http://paw.web.cern.ch/paw/ [viewed on Mar. 1, 2007].

[40] J. F. Ziegler, J. P. Biersack, and U. Littmark, *The Stopping and Range of Ions in Solids* (Pergamon Press, New York, 2003), the code SRIM can be downloaded from http://www.srim.org/.

[41] K. Perajarvi, C. Fu, G. V. Rogachev, G. Chubarian, V. Z. Goldberg, F. Q. Guo, D. Lee, D. M. Moltz, J. Powell, B. B. Skorodumov, G. Tabacaru, X. D. Tang, R. E. Tribble, B. A. Brown, A. Volya, and J. Cerny, Physical Review C **74**, (2006).

[42] V. Z. Goldberg, G. G. Chubarian, G. Tabacaru, L. Trache, R. E. Tribble, A. Aprahamian, G. V. Rogachev, B. B. Skorodumov, and X. D. Tang, Phys. Rev. C **69**, 031302 (2004).

[43] M. Freer, E. Casarejos, L. Achouri, C. Angulo, N. I. Ashwood, N. Curtis, P. Demaret, C. Harlin, B. Laurent, M. Milin, N. A. Orr, D. Price, R. Raabe, N. Soic, and V. A. Ziman, Physical Review Letters **96**, 042501 (2006).

[44] P. Boutachkov, G. V. Rogachev, V. Z. Goldberg, A. Aprahamian, F. D. Becchetti, J. P. Bychowski, Y. Chen, G. Chubarian, P. A. DeYoung, J. J. Kolata, L. O. Lamm, G. F. Peaslee, M. Quinn, B. B. Skorodumov, and A. Wöhr, Phys. Rev. Lett. **95**, 132502 (2005).

[45] K. Markenroth, L. Axelsson, and S. Baxter, Phys. Rev. C **62**, 034308 (2000).

[46] E. P. Wigner and L. Eisenbud, Phys. Rev. **72**, 29 (1947).

[47] A. M. Lane and R. G. Thomas, Rev. Mod. Phys. **30**, 257 (1958).

[48] P. Descouvemont, in *Theoretical Models for Nuclear Astrophysics* (Nova Science, New York, 2003), Chap. 4, pp. 33–54.

[49] H. Feshbash, *Theoretical nuclear physics: Nuclear reactions* (John Wiley & Sons, Inc., New York, 1992).

[50] G. L. Morgan, D. R. Tilley, G. E. Mitchell, R. A. Hilko, and N. R. Roberson, Nucl. Phys. A **148**, 480 (1970).

[51] H. E. Gove and A. E. Litherland, Phys. Rev. **113**, 1078 (1959).

[52] V. Z. Goldberg, K. Kallman, T. Lonnroth, P. Manngard, and B. Skorodumov, Phys. Atom. Nucl. **68**, 1079 (2005).

[53] L. Buchmann, J. D'Auria, M. Dombsky, U. Giesen, K. P. Jackson, P. McNeely, J. Powell, and A. Volya, Phys. Rev. C **75**, 012804 (2007).

[54] M. Gai, S. L. Rugari, R. H. France, B. J. Lund, Z. Zhao, D. A. Bromley, B. A. Lincoln, W. W. Smith, M. J. Zarcone, and Q. C. Kessel, Phys. Rev. Lett. **62**, 874 (1989).

[55] R. Dalitz, Phil. Mag. **44**, 1068 (1953).

[56] A. V. Nero, E. G. Adelberger, and F. S. Dietrich, Phys. Rev. C **24**, 1864 (1981).

[57] M. A. Preston and R. K. Bhaduri, *Structure of the Nucleus* (Addison Wesley Publishing Company, Reading, Massachusetts, 1975).

[58] B. V. Danilin, M. V. Zhukov, A. Korsheninnikov, L. Chulkov, and V. Efros, Sov. J. Nucl. Phys. **46**, 225 (1987).

[59] E. I. Dolinskii and A. M. Mukhamedzhanov, Sov. J. of Nucl. Phys. **3**, 180 (1966).

[60] H. V. Heringen, Nucl. Phys. A **253**, 355 (1975).

[61] Y.Yanagisawa and et al., RIKEN Accel. Prog. Rep. **34**, 183 (2001).

[62] J. C. Overley and W. Whaling, Phys. Rev. **128**, 315 (1962).

[63] SpecTcl, http://docs.nscl.msu.edu/daq/spectcl/ [viewed on Mar. 1, 2007].

VITA

Changbo Fu was born in Naixiang, Henan province, P. R. China in 1974. He graduated from Chengjiao High school, Henan province, and enrolled in Lanzhou University, Lanzhou, China in 1991. He obtained his B.S. degree in physics from Lanzhou University and then joined the China Institute of Atomic Energy (CIAE), Beijing, China in 1995. He received his M.S. degree from CIAE in 2001. In the same year, he was accepted by the Physics Department at Texas A&M University as a Ph.D. student and received his Ph.D degree in May 2007. He can be reached at Fuzhuang, Guanzhang, Naixiang, Henan Province 474360, P.R. China.